297
7-9-70

DWR-12456

BAW-3809-6
August 1969
TID-4500
UC-25

Babcock & Wilcox

MASTER

EXAMINATION OF STAINLESS-STEEL-CLAD ThO_2-UO_2 FUEL RODS AND ZIRCALOY-2 CAN AFTER OPERATION FOR 442 EFPD IN THE INDIAN POINT REACTOR

RESEARCH & DEVELOPMENT DIVISION

NUCLEAR DEVELOPMENT CENTER

Lynchburg, Virginia

DISCLAIMER

Printed in the United States of America
Available from
Clearinghouse for Federal Scientific and Technical Information
National Bureau of Standards, U.S. Department of Commerce
Springfield, Virginia 22151
Price: Printed Copy $3.00; Microfiche $0.65

BAW-3809-6
August 1969
TID-4500
UC-25

EXAMINATION OF STAINLESS-STEEL-CLAD ThO_2-UO_2 FUEL RODS AND ZIRCALOY-2 CAN AFTER OPERATION FOR 442 EFPD IN THE INDIAN POINT REACTOR

FINAL REPORT

Volume 1 of 3 Volumes

by

C. J. Baroch
E. N. Harbinson
A. V. Munim

AEC Contract No. AT(30-1)-3809
B&W Contract No. 859-3103

Prepared for
THE UNITED STATES ATOMIC ENERGY COMMISSION
by
BABCOCK & WILCOX
Nuclear Development Center
P.O. Box 1260
Lynchburg, Virginia 24505

Babcock & Wilcox

CONTENTS

List of Tables

Tables (Cont'd)

List of Figures

Figures (Cont'd)

Figures (Cont'd)

Figures (Cont'd)

1. SUMMARY

Detailed hot cell examinations were performed on 13 ThO_2-UO_2 fuel rods and one Zircaloy-2 can that had been operated in Consolidated Edison's Indian Point Reactor for 442 effective full power days (EFPD). During this operating period, the fuel had achieved peak burnups as high as 33,000 MWd/T, and the borated type 304 stainless steel cladding and the Zircaloy-2 can received peak fast neutron fluences (E > 1 MeV) of about 3×10^{21} nvt.

The examinations showed that all 13 fuel rods and the Zircaloy-2 can had performed very satisfactorily. Nothing observed during the examination indicated that these core components could not operate to a considerably higher exposure.

The reactor exposure caused no major microstructural changes in the fuel. The lack of microstructural changes indicated that the centerline fuel temperature was probably less than 1600 C. The amount of fission gases released—1 to 2%—is consistent with results from fuel temperatures in the 1600 C range.

The ThO_2-UO_2 fuel operated to exposures of 33,000 MWd/T without introducing localized or general strains in the cladding. No ridging at the pellet interfaces was observed, even in the rod of highest exposure. Entire pellets could be easily removed from all rods regardless of the enrichment of the fuel or the burnup achieved. These fuel rods were fabricated with a diametral gap of 0.002 to 0.004 inch. The lack of pellet distortion and cladding strains and the fact that entire pellets could be removed from the cladding indicated that irradiation-induced fuel swelling was minimal. Urania fuels operated under similar conditions would show some increase in volume and possibly some ridging at pellet interfaces.

Porosity was observed on the inside surface of the borated type 304 stainless steel cladding. This porosity took a variety of shapes,

from fine, hairline cracks to spherical voids. The exact cause of the porosity was not determined, but it had no apparent ill effects on the performance of the fuel rod.

Irradiation affected the tensile properties of the stainless steel cladding rather significantly. The ductility, as determined by uniform and total elongations, was quite low (generally less than 1% except at 70 F where it was about 5%) at all test temperatures and for the range of calculated fluences investigated (5×10^{20} to 3×10^{21} nvt). Annealing the cladding for 1 hour at 1000 C had little effect on the ductility of the cladding at all test temperatures, but annealing did reduce the yield and ultimate strengths to essentially the unirradiated values. From these results, it appears that helium in sufficient quantities can reduce the ductility of austenitic stainless steels at all test temperatures.

The in-reactor performance of the Zircaloy-2 can was identical to that predicted from out-of-pile tests. Although the oxide film was too thin to measure, the weight gain was estimated to be less than about 20 mg/dm^2 and the hydrogen content less than 40 ppm. The mechanical properties of the irradiated Zircaloy were similar to what one would predict from the available data. The uniform elongations of all specimens, regardless of the test temperature, were less than 1%.

2. INTRODUCTION

The objectives of this program were to determine the isotopic content of several heavy elements and fission products in irradiated thoria-urania fuels and to perform metallurgical examinations on the fuels, the stainless steel cladding, and the Zircaloy-2 fuel can. The specimens were taken from core A of the Consolidated Edison Indian Point Reactor.

Thirteen fuel rods from six elements were selected for analysis. The rods were gamma scanned and punctured for fission gas release. The results of the gamma scans were used in selecting samples for isotopic analyses and metallurgical examination.

The results of metallographic examinations of the thoria-urania fuel, stainless steel cladding, and Zircaloy fuel can are described in this report. The isotopic abundances of certain transactinium and fission product elements were determined; the results of these experiments are reported in BAW-3809-7.

The following reports have been issued under this program:

BAW-3809-1	Progress Report No. 1 - March - August 1967
BAW-3809-2	Progress Report No. 2 - September - November 1967
BAW-3809-3	Progress Report No. 3 - December 1967 - February 1968
BAW-3809-4	Progress Report No. 4 - March - May 1968
BAW-3809-5	Progress Report No. 5 - June - August 1968
BAW-3809-6	Examination of Stainless-Steel-Clad ThO_2-UO_2 Fuel Rods and Zircaloy-2 Can After Operation for 442 EFPD in The Indian Point Reactor
BAW-3809-7	Post-Irradiation Examination of Thoria-Urania Fuel Rods—Isotopic Analysis of the Fuel

3. CONCLUSIONS

The following conclusions were made after evaluation of the post-irradiation examinations of 13 ThO_2-UO_2 fuel rods and one Zircaloy-2 can from the Consolidated Edison Indian Point Reactor:

3.1. General

The ThO_2-UO_2 fuel, the type 304 stainless steel modified with 250 ppm of boron, and the Zircaloy-2 can were in excellent condition after the 442-EFPD operation in the reactor. Nothing observed in the postirradiation examination indicated that these materials could not operate for a considerably longer period.

3.2. ThO_2-UO_2 Fuel

The amount of fission gas released from the ThO_2-UO_2 fuel was less than 2.0% regardless of enrichment or burnup. A like amount of fission gases would be released from UO_2 operated under similar conditions.

Distortion and swelling of the fuel during operation were minimal, since entire fuel pellets could be removed from the rods regardless of their enrichment or burnup. Furthermore, no ridging was observed at the pellet interfaces. It appears that ThO_2-UO_2 fuels are more resistant to thermal cracking, hour-glassing, and irradiation swelling than are UO_2 fuels operated under similar conditions.

Some fuel of the wrong enrichment had been placed in some of the fuel rods accidentally. In addition, metallic inclusions, which apparently were introduced during fabrication, were observed in most of the fuel. These two anomalies had no noticeable effect on the performance of the fuel rods.

3.3. Borated Stainless Steel Cladding

Cracking and porosity were observed on the inside surface of the cladding from almost all of the fuel rods. This porosity assumed a

variety of shapes, ranging from fine, hairline cracks to spherical voids. Archive samples of the unirradiated cladding did not contain the porosity; however, there is some doubt concerning the origin of these samples. Therefore, it cannot be determined conclusively whether this porosity was present in the as-fabricated cladding or was produced by irradiation. The depth of penetration, less than 0.002 inch, was small enough so that it would not be cause for rejection of the as-fabricated tubing. Regardless of the source of this porosity, it did not affect the performance of the fuel rods.

At test temperatures below 900 F, the strength of the cladding was increased by irradiation. At test temperatures above 900 F, irradiation had little effect on cladding strength. At all test temperatures, however, the ductility of the cladding was quite low, and often it was less than 0.5%. Post-irradiation annealing for one hour at 1832 F returned the strength to the unirradiated condition but had little effect on the ductility. The presence of boron in the steel results in a slightly different effect during irradiation than that observed with standard type 304 stainless steel. Irradiation of the borated stainless steel at 600 F apparently introduces enough helium into the steel so that the ductility at test temperatures of 900 F and below is reduced significantly, even after a post-irradiation annealing operation.

3.4. Zircaloy-2 Can

The corrosion resistance of the Zircaloy-2 can was excellent. The oxide film was too thin to measure, and the hydrogen content was less than 40 ppm. These results are quite typical of Zircaloy-2 exposed to 525 F water for up to 20,000 hours.

Irradiation had increased the strength and reduced the ductility of the Zircaloy-2. The properties of the Zircaloy-2 after irradiation to a fluence of 2.5×10^{21} nvt were consistent with those reported by some of the data in the literature.

4. FUEL ROD EXAMINATION

4.1. Visual

4.1.1. Purpose

The fuel rods were visually examined to determine their general appearance and to locate any areas of unusual appearance. The visual examination provided data for use in defining subsequent examinations. Areas of specific interest included corrosion patterns, integrity of the braze joints, and the possibility of cladding penetrations.

4.1.2. Scope

All 13 of the fuel rods were visually examined in detail.

4.1.3. Procedure

Each rod was individually examined with the hot cell periscope at a magnification of about 10 power. Areas of unusual appearance were photographed.

4.1.4. Results

The visual examination indicated that all 13 fuel rods were in excellent condition. The rods were coated with a dark gray oxide film, and there were no signs of deterioration of the cladding or the ferrules. The examination did not reveal that the cladding on nine of the rods had been penetrated when the rods were removed from the elements. The overall appearance of two fuel rods is shown in Figures 4-1 and 4-2, and the appearance of one of the rods in the area of a penetration is shown in Figure 4-3.

4.2. Profilometer Measurements

4.2.1. Purpose

The profilometer measurements were taken to determine the extent of any localized or overall changes in the diameter of the fuel

rods. These measurements are used to evaluate the extent of ridging at the pellet interfaces and the swelling of the fuel rod under irradiation.

4.2.2. Scope

Ten 7-inch segments were obtained from five different fuel rods. The locations of these sections are shown schematically in Figure 5-1 and listed in Table 4-1. The ten segments represent burnups from about 3 GWd/T to 30 GWd/T.

Table 4-1. Location of Profilometer Specimens

Rod No.	Estimated rod burnup, MWd/T	Specimen location		
		High	Average	Low
61A	30	1	1	1
105A	22	1	1	1
105C	15	1	0	0
$105D_1$	20	1	0	0
106A	8	1	0	1

4.2.3. Procedure

The sections of the fuel rods which were obtained for the profilometer measurements were about 7 to 8 inches long. The 9-inch spacing between the ferrules precluded the possibility of obtaining sections any longer than 8-inches. While the sections of the fuel rods were held in a stationary position they were scanned by a pair of probes bearing on diametrically opposite sides of the rod sections. The travel of the probe, which was perpendicular to the axis of the fuel rod section, was converted to an electrical signal by linear variable differential transformers. The output signal was continuously recorded on a strip chart.

After the first diametral scan, the fuel rod section was rotated 45 degrees and the scanning was repeated. This procedure was repeated until diametral measurements were obtained at 0-180, 45-225, 90-270, and 135-315 degrees.

Bow measurements were obtained using only one probe and traveling the rod in the manner used for diametral measurements.

Thus bow measurements were obtained at 0, 45, 90, 135, 180, 225, 270, and 315 degrees. Spiral bow and spiral diameter measurements were obtained by rotating the section of the fuel rod as the probe or probes traveled in a direction parallel to the axis of the fuel rod section.

4.2.4. Results

The results of the diameter measurements at 0 and 90 degrees for all ten sections are shown in Figures 4-4 through 4-9. Typical bow, spiral bow, and spiral diameter measurements are shown in Figures 4-10, 4-11, and 4-12, respectively. These scans indicate that the diameter of the fuel rod is extremely uniform and is well within the as-fabricated dimensional tolerance of 0.304 ± 0.001 inch. Furthermore, there is no evidence of ridging or cladding distortion at the pellet interfaces. The measurements of both the diameter and the spiral indicate that there was little or no ovality in the tubing.

Significant rod bowing was observed, as shown in Figure 4-10. However, it is impossible to determine whether this bowing was present before irradiation, occurred during irradiation, was introduced during removal of the fuel rods from the fuel bundles, or was introduced during the sectioning of the fuel rods.

4.3. Gamma Scanning

4.3.1. Purpose

The gamma scanning was performed to determine an approximate axial distribution of fission product activity and fast fluence and to determine whether there was any unusual behavior of the fuel rods. Because the fission product activity is proportional to fission power production, the gamma scan can be used to locate the peak burnup region and to determine the peak-to-average burnup ratio, the relative burnup, and the integrated fluences at various axial positions on the fuel rod.

4.3.2. Scope

All 13 fuel rods were given a gross gamma scan to determine the shape of the burnup profile. Several locations on all 13 rods were examined with the multichannel analyzer to determine the source of the gamma activity.

4.3.3. Procedure

Gamma scans were obtained by moving a vertically suspended fuel rod past a slit 0.50 inch wide and 0.025 inch high. The gamma rays were collimated by the slit over a distance of 42 inches. The collimated beam was directed at a sodium iodide crystal in a scintillation probe monitored by a count-rate meter. Readout was provided or a chart was recorded in which 1 inch of chart travel was equivalent to 1.862 inches on the fuel rod.

4.3.4. Results

A typical gamma scan is shown in Figure 4-13. The gamma activity in the center third of rod 105F was very low because of the low fissioning rate in the pure ThO_2. The gamma scan of rod 105F is shown in Figure 4-14.

During the gamma scanning it was observed that pellets of a higher enrichment were accidently inserted into three fuel rods; a typical example of this is shown in the gamma scan of rod 105F (Figure 4-14). The areas that contained fuel of the improper enrichment are described briefly below. The presence of the fuel with enrichments greater than specified did not appear to produce any adverse effects during operation of the fuel rods.

		Wrong pellet	
Rod No.	Type of fuel, ^{235}U enrichment, %	Type of fuel, ^{235}U enrichment, %	Location, in. from top
106B	B - 4.2	C - 5.5	40
105F	F - Pure ThO_2	A - 3.0	50
106A	A - 3.0	B - 4.2	47

During the gamma scanning, it was observed that the fuel pellets were free to move within the fuel tube. An example of this is shown in the two gamma scans (Figures 4-15 and 4-16) of rod 105A, which was scanned before and after inverting the rod. The location of the internal voids shifted during the inversion as shown in Table 4-2. The movement of fuel within the rods was not limited solely to rod 105A

but occurred in practically all other rods (as indicated in section 5.2, Sectioning). The fact that the fuel was able to move within the rods indicated that fuel swelling and distortion during irradiation was minimal, even in the high-burnup rods.

The analyses of the gross gamma scans indicated that the peak-to-average activity, which is also believed to be indicative of the burnup profile, was between 1.28 and 1.35 for all rods except 105F. The presence of the pure ThO_2 central section in this rod created a significantly different activity profile, as shown in Figure 4-14. The P/A ratio measured by the gamma activity is in close agreement with the number predicted by the nuclear physics calculations, 1.35.

Gamma spectra were recorded at various points along the rods. Many of the radioactive pieces had decayed below detection limits in the three years since reactor shutdown. The primary activities were from cesium-134 and -137 and cerium-144-praseodymium-144 produced from the fuel and cobalt-60 produced from the cladding. There was no significant variation in the ratio of cesium-137 to cerium-144-praseodymium-144 along the rods.

Table 4-2. Locations of Gaps in Fuel Column in Rod 105A

Location of voids,[1] in. from bottom	Type of void	
	Scanned in upright position	Scanned in inverted position
5-1/4 - 5-1/2	None	Gap
6-1/2	Dip in scan	None
9-3/8 - 9-1/2	Gap	Gap
10-1/4	Dip in scan	None
11-7/8	None	Dip in scan
12-1/8	Dip in scan	Dip in scan
12-5/8 - 12-3/4	Dip in scan	Gap
18-1/2 - 8-3/4	Gap	Dip in scan
19-7/8	Dip in scan	None
20-1/8 - 20-3/8	None	Gap
20-3/8	Dip in scan	None
27-3/4 - 28	Gap	Gap
36-1/4 - 36-1/2	Gap	Gap
45-3/4 - 46	None	Gap
46 - 46-1/4	Gap	None

Figure 4-1. General Appearance of Surface of Fuel Rod 62A

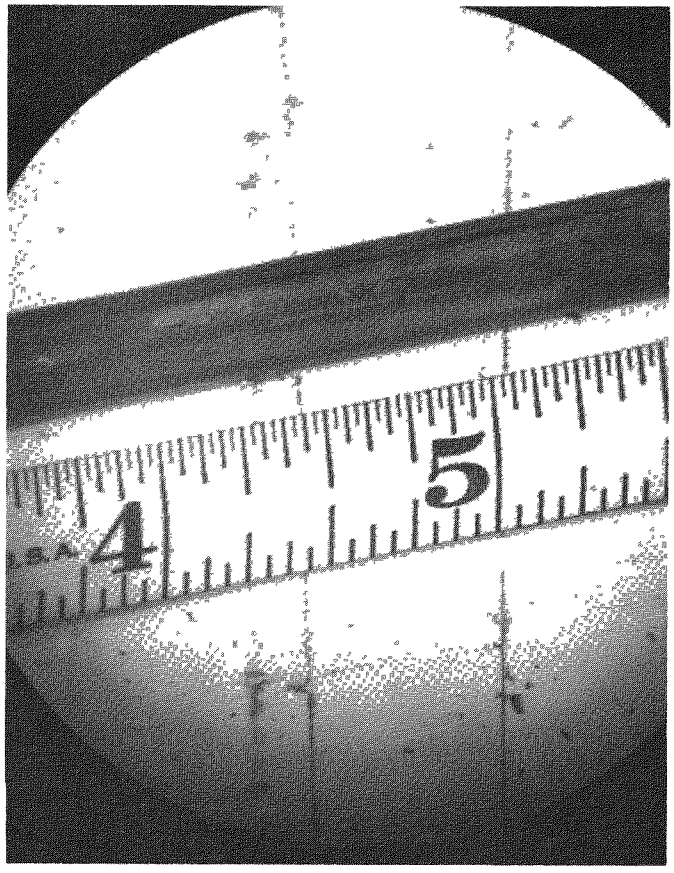

Figure 4-2. General Appearance of Surface of Fuel Rod 195B

Figure 4-3. Typical Appearance of Cladding Penetration That Occurred in Rod 62A During Its Removal From the Fuel Bundle

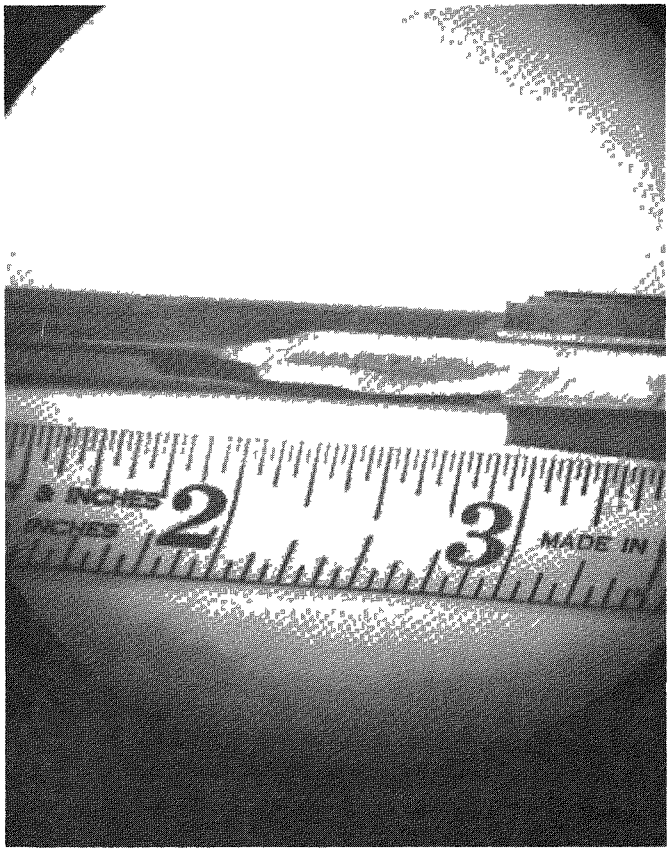

Figure 4-4. Profilometer Scans of Two Sections From Fuel Rod 61A

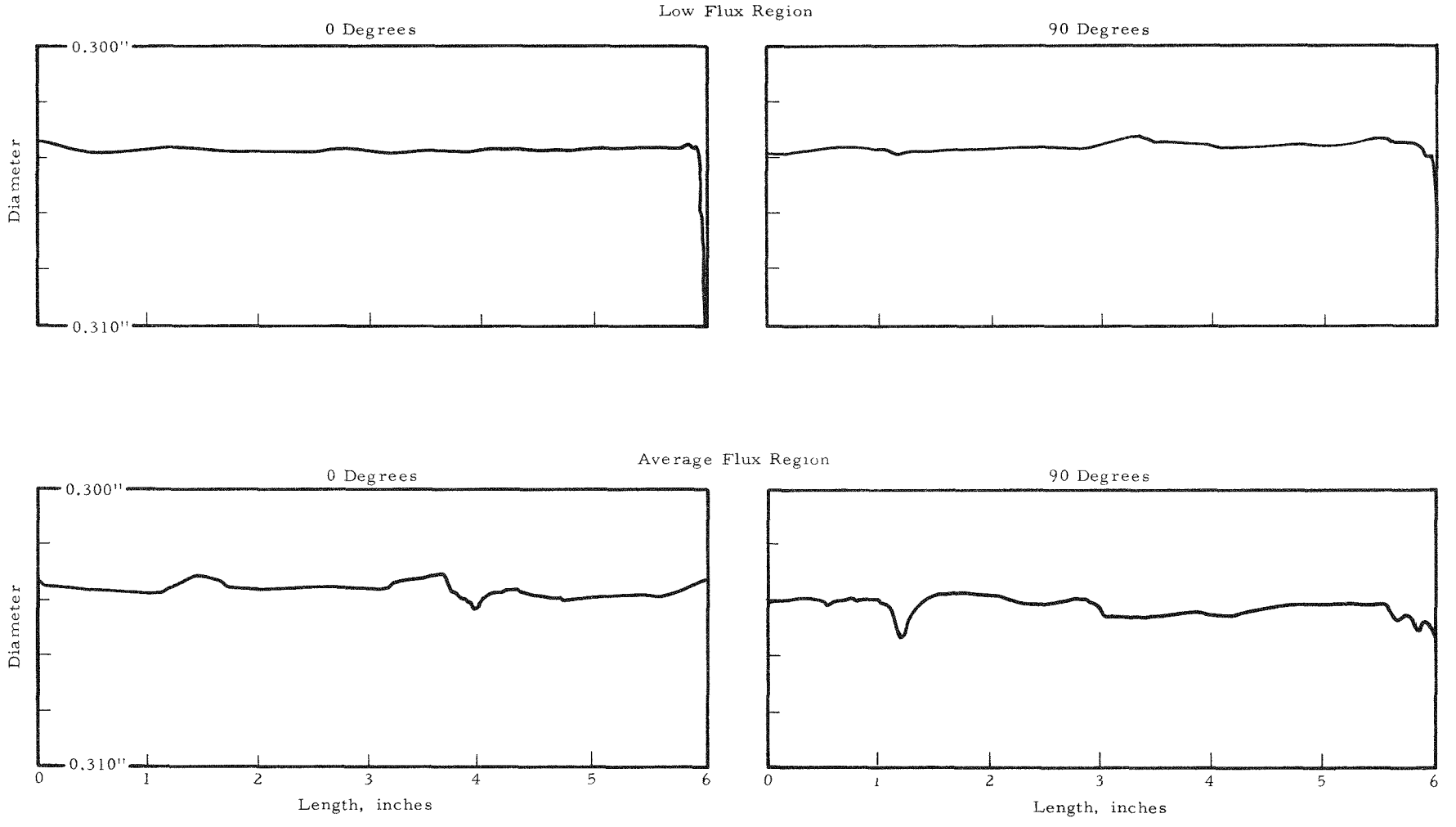

Figure 4-5. Profilometer Scan From Peak Flux Location of Fuel Rod 61A

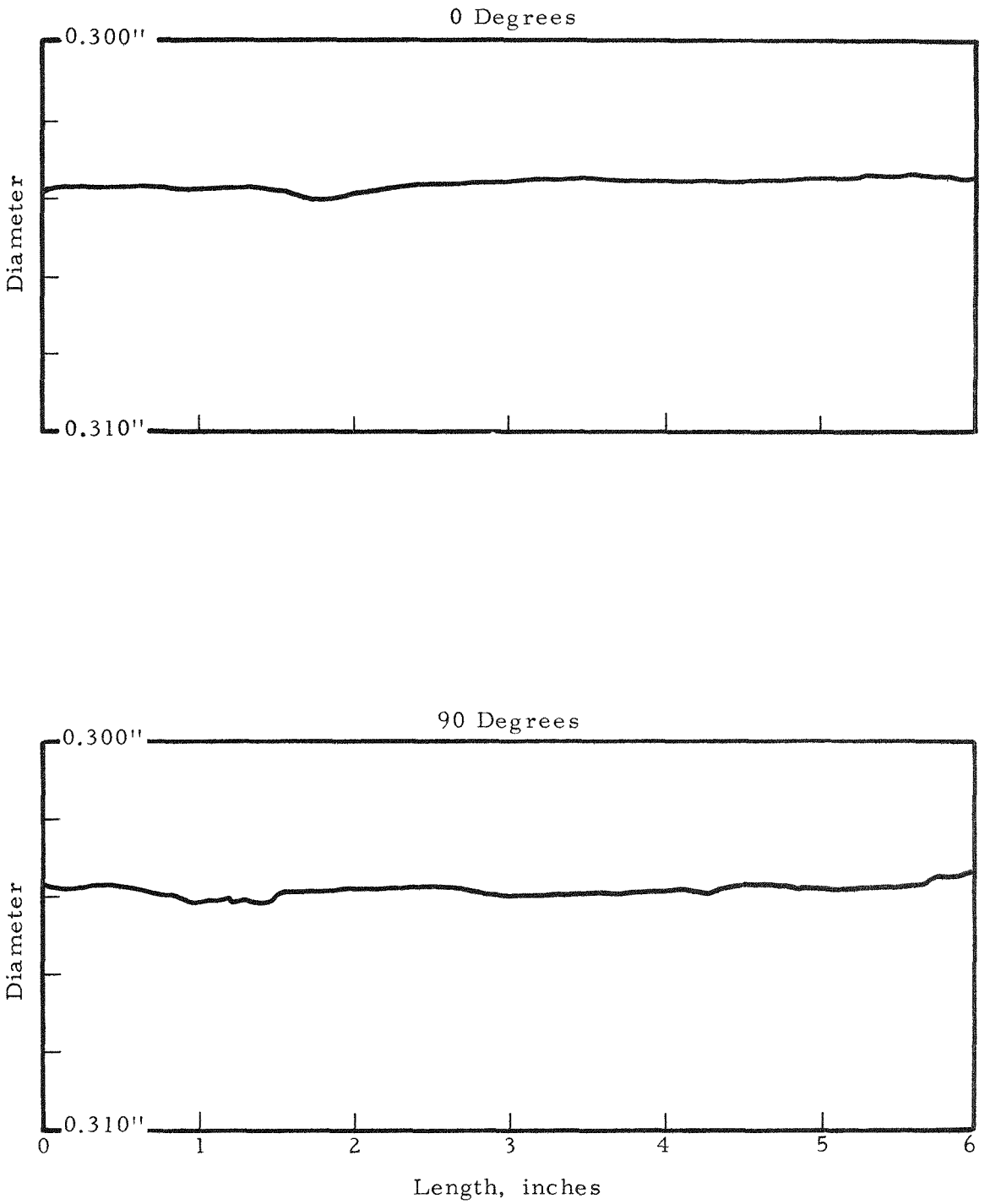

Figure 4-6. Profilometer Scans of Two Sections From Fuel Rod 105A

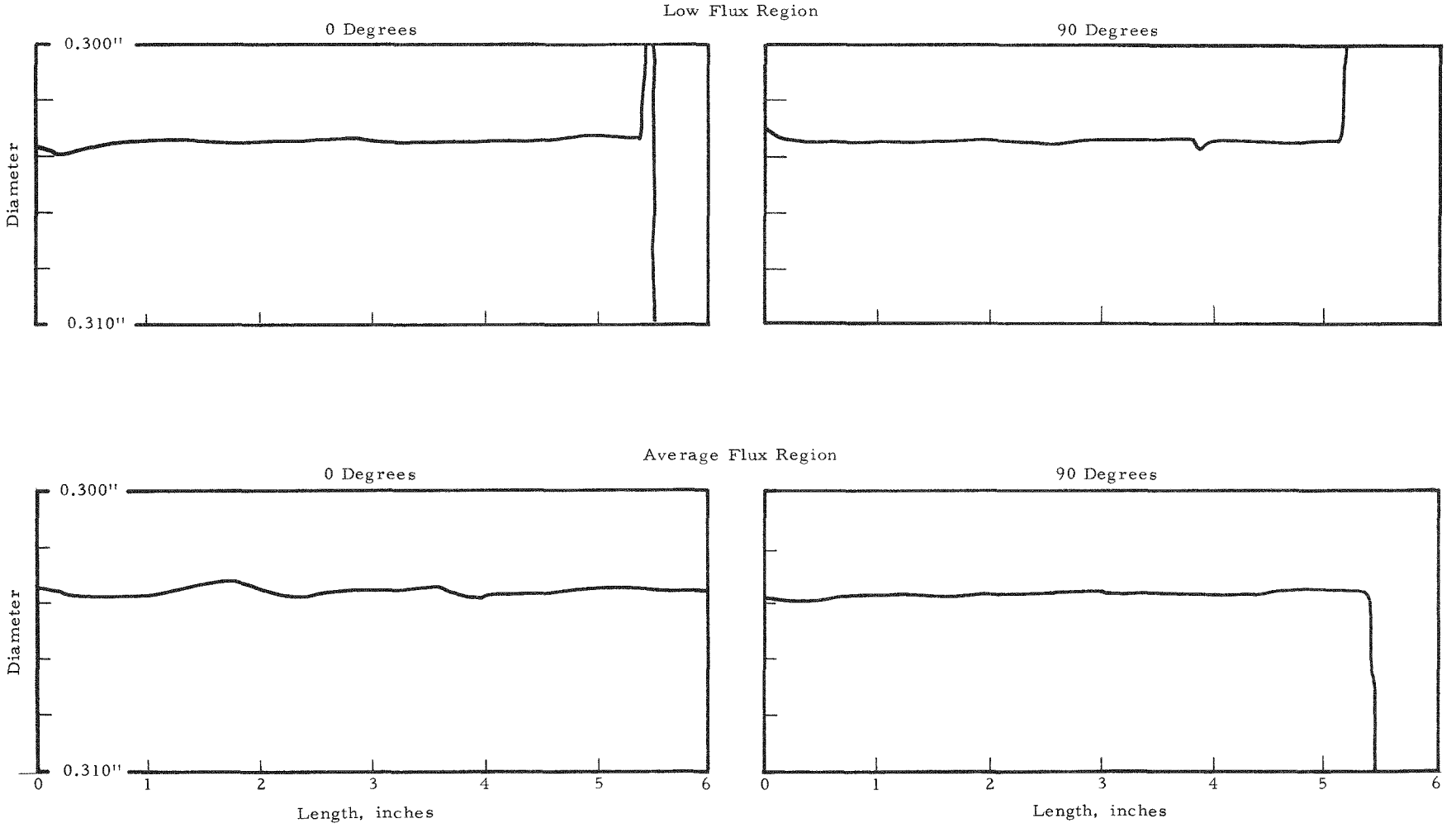

Figure 4-7. Profilometer Scans From Peak Flux Region of Fuel Rod 105A

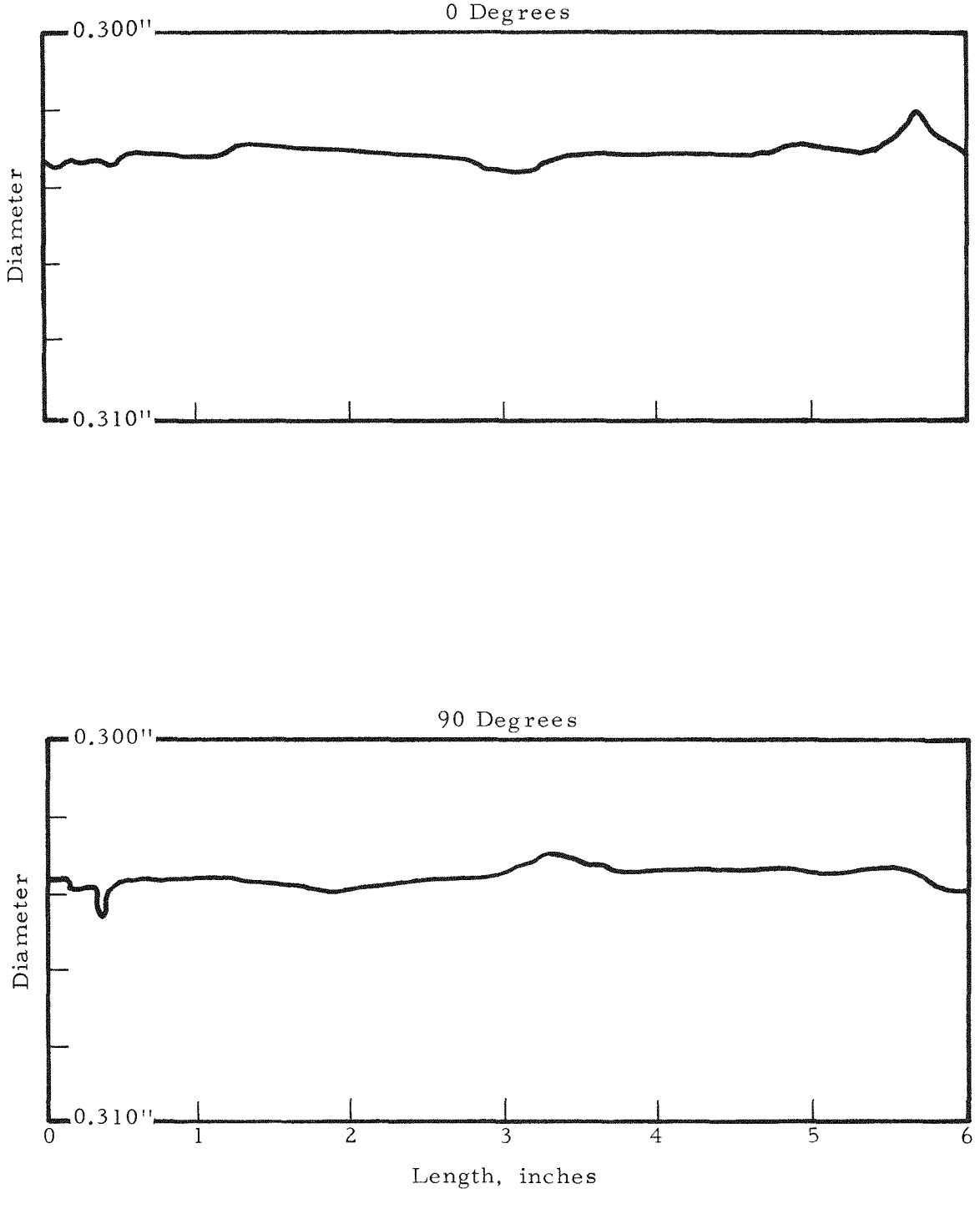

Figure 4-8. Profilometer Scans of Sections From Peak Flux Locations in Fuel Rods 105C and 105D

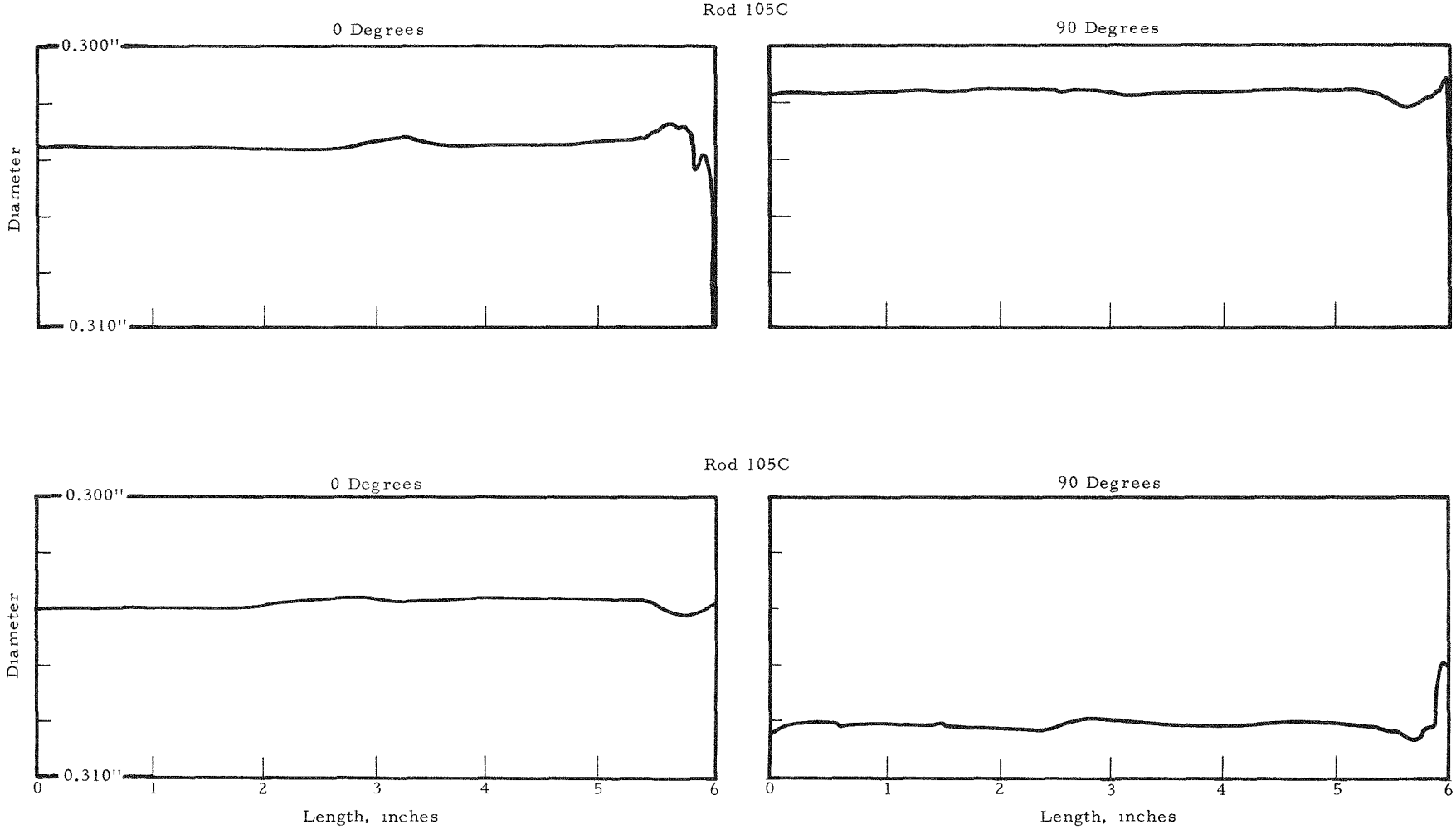

Figure 4-9. Profilometer Scans of Two Sections From Fuel Rod 106A

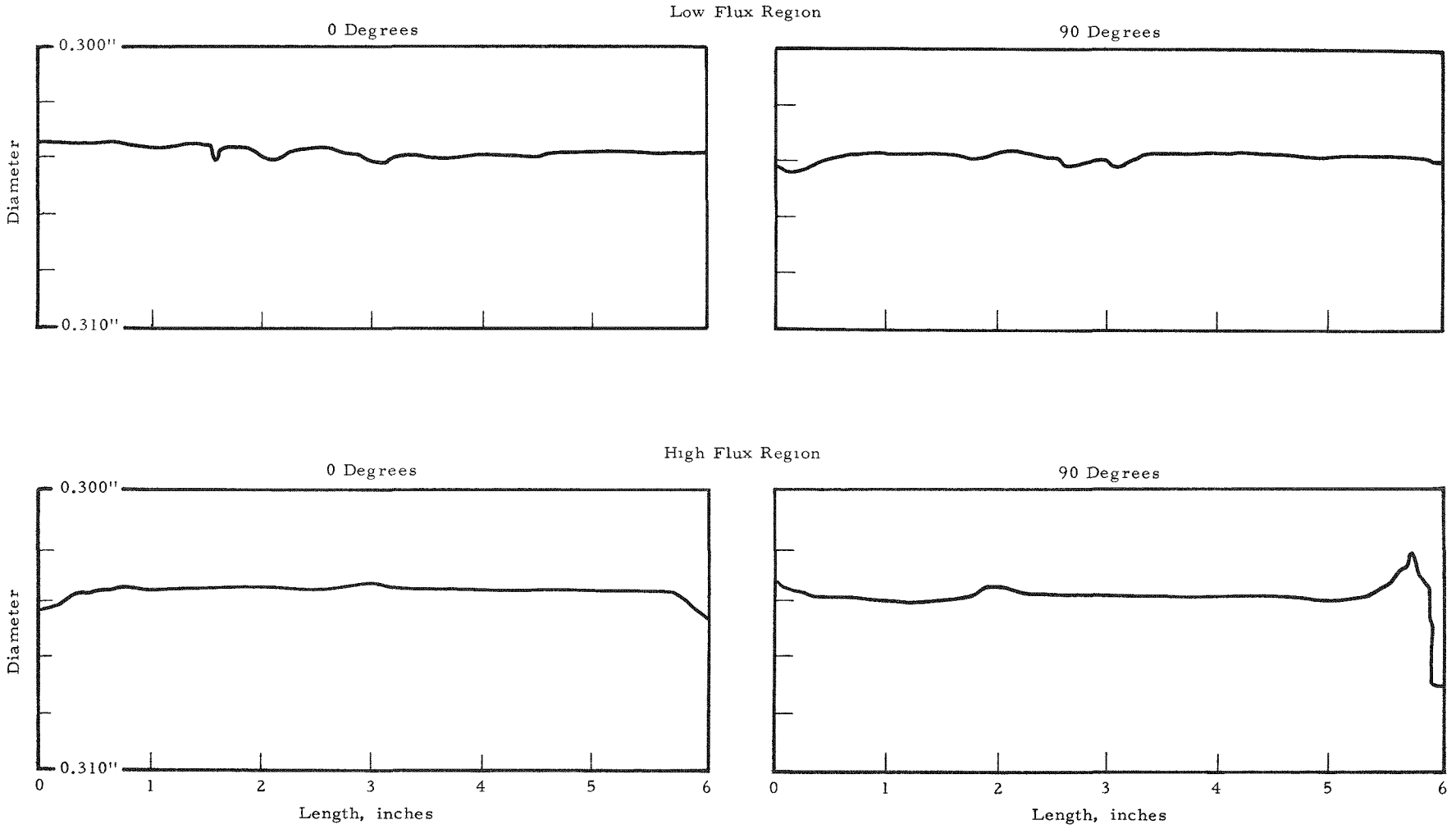

Figure 4-10. Typical Bow Traces From Section 6 of Fuel Rod 105C

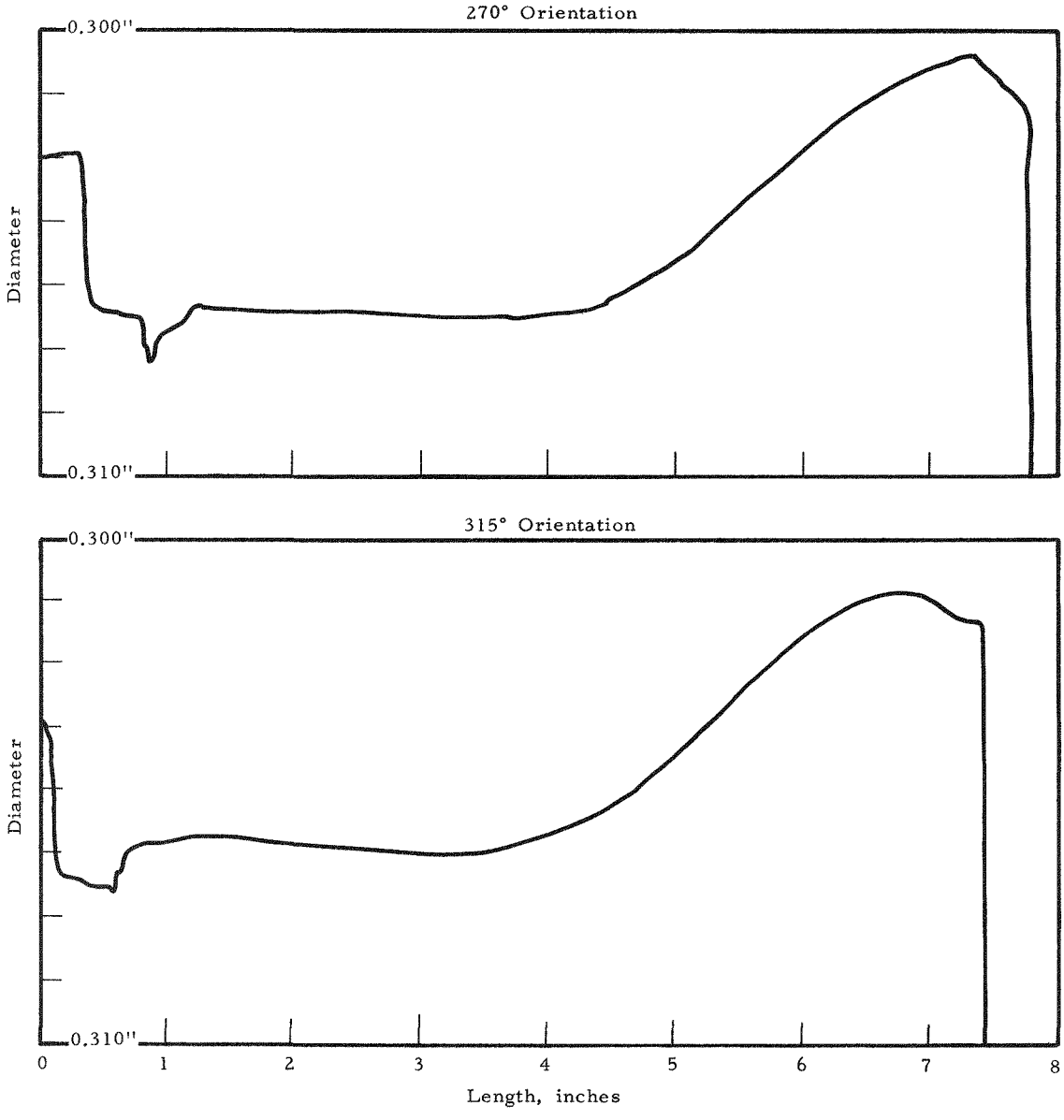

Figure 4-11. Typical Bow Spiral Traces: Section 6, Fuel Rod 61A and Section 14, Fuel Rod 105C

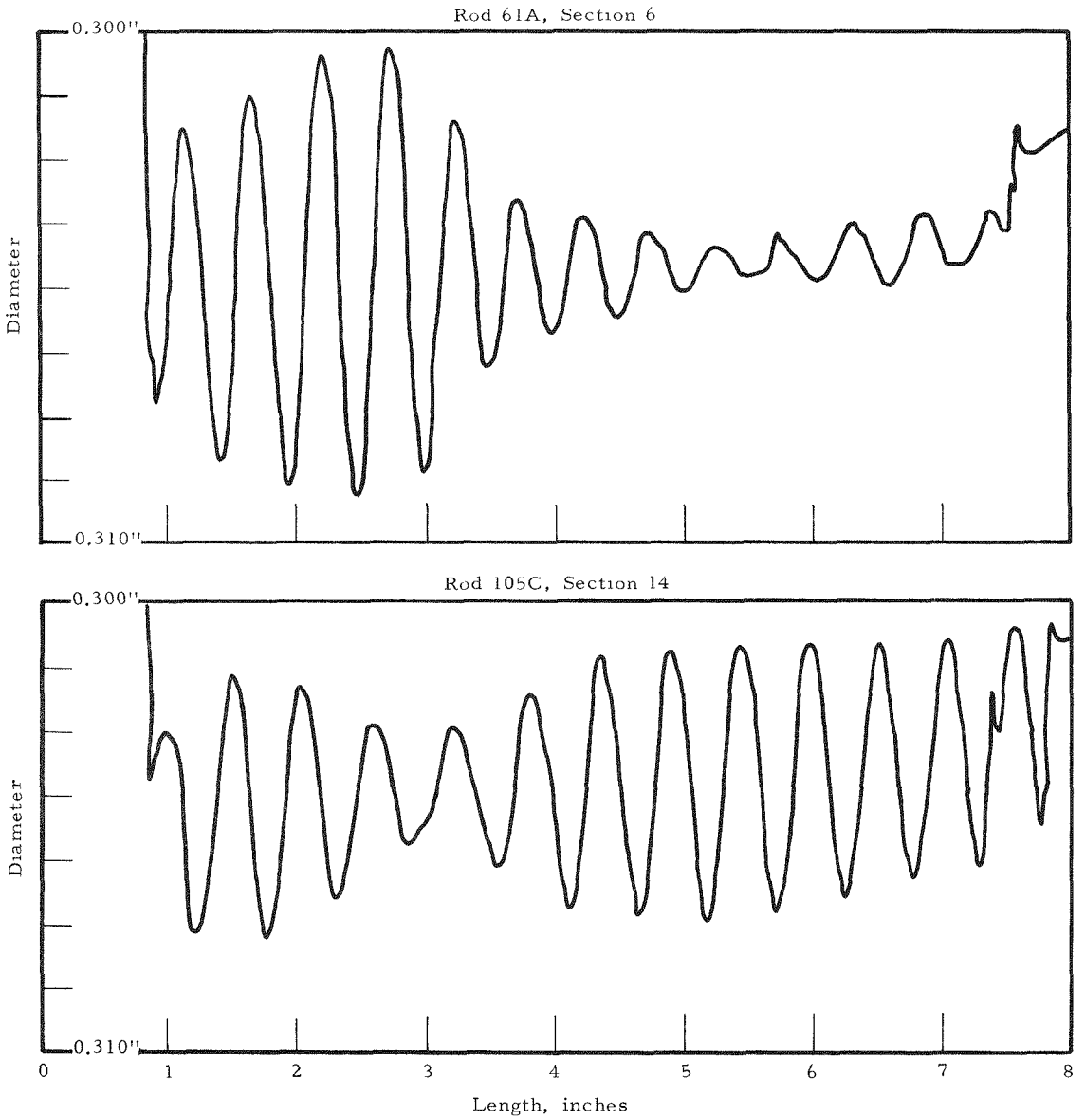

Figure 4-12. Typical Spiral Diameter Traces: Section 6, Fuel Rod 61A and Section 14, Fuel Rod 105C

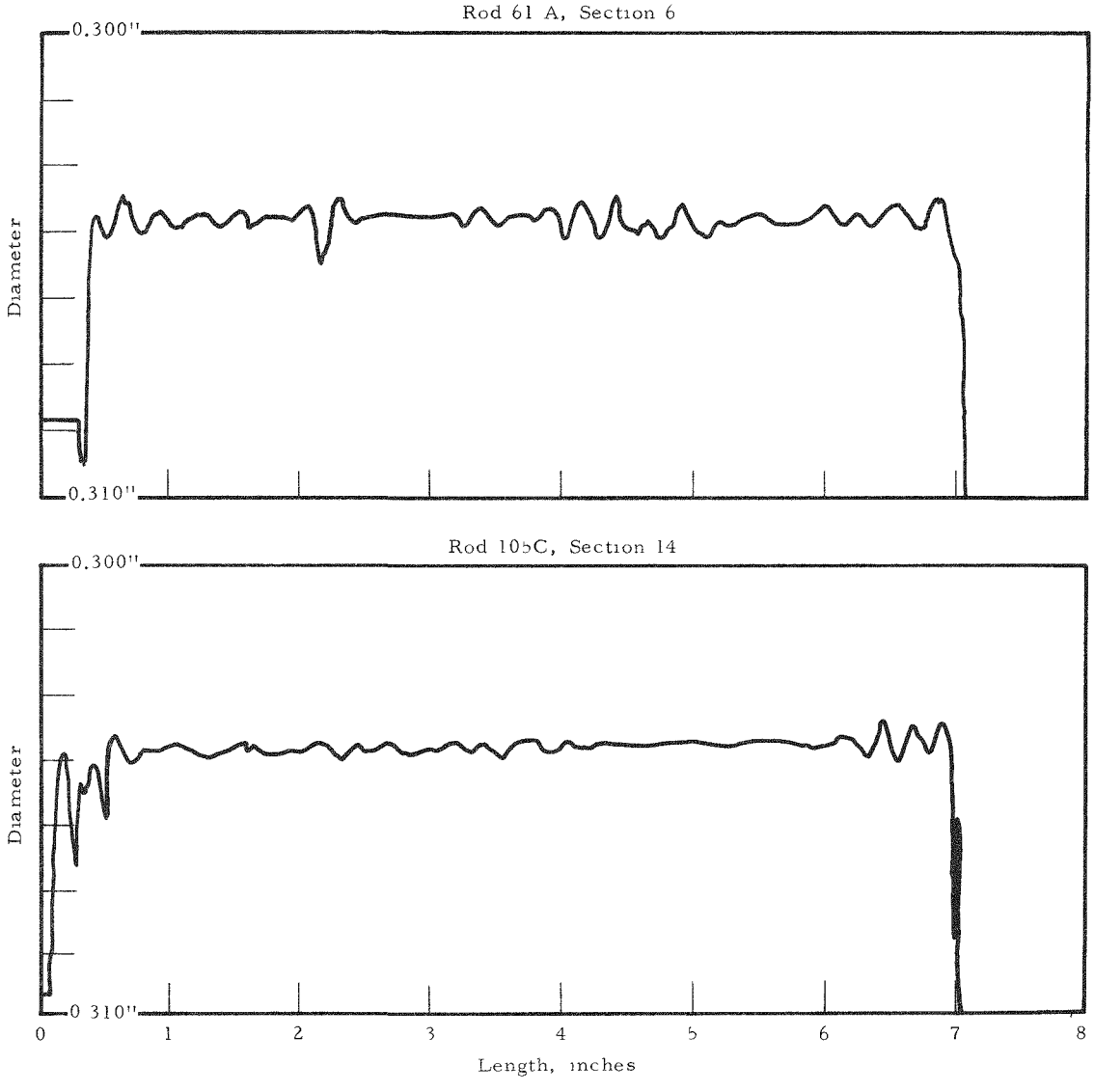

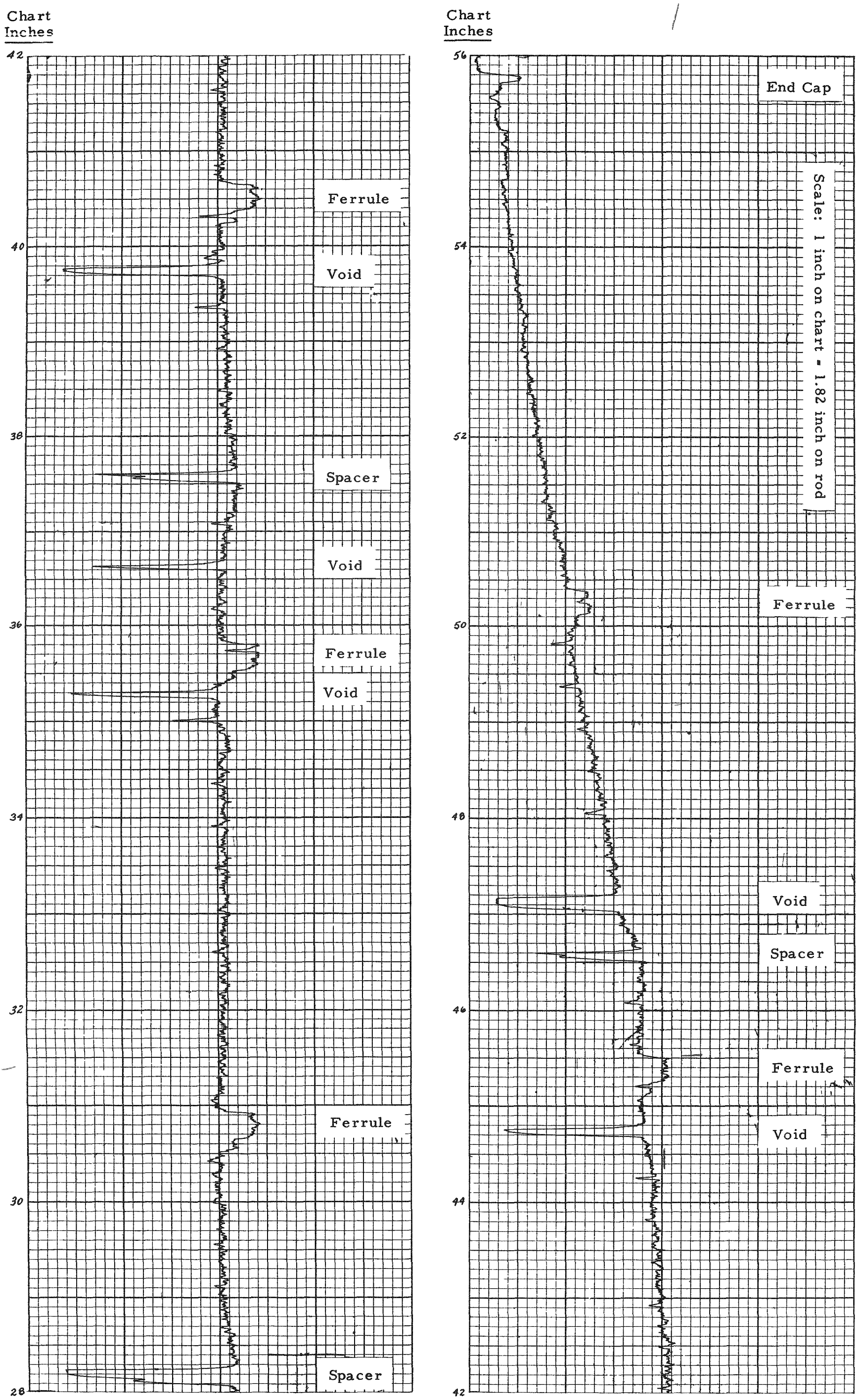

Figure 4-13. Gross Gamma Profile of Fuel Rod 62A

Figure 4-13. (Cont'd)

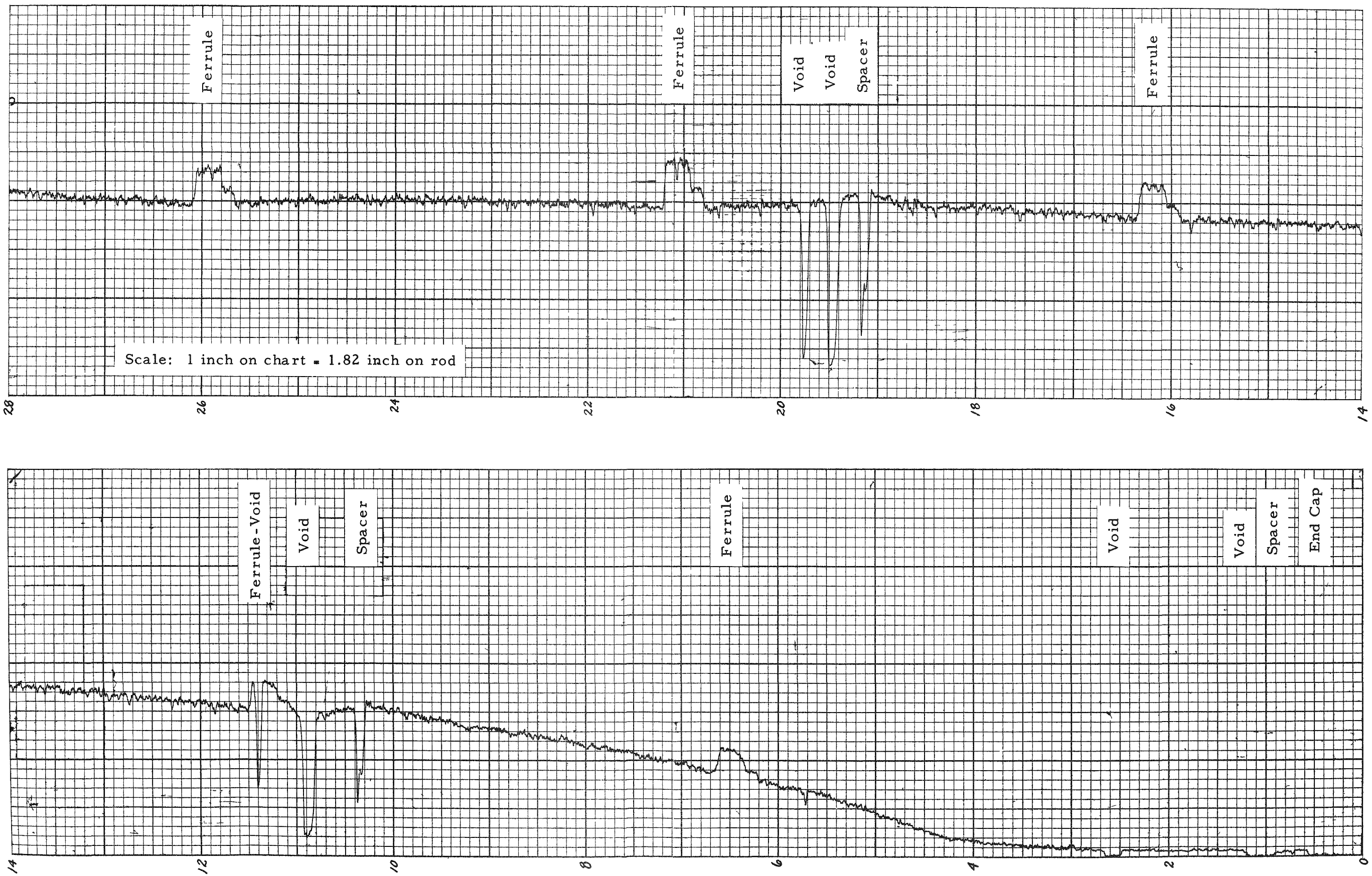

Figure 4-14. Gross Gamma Profile of Fuel Rod 105F

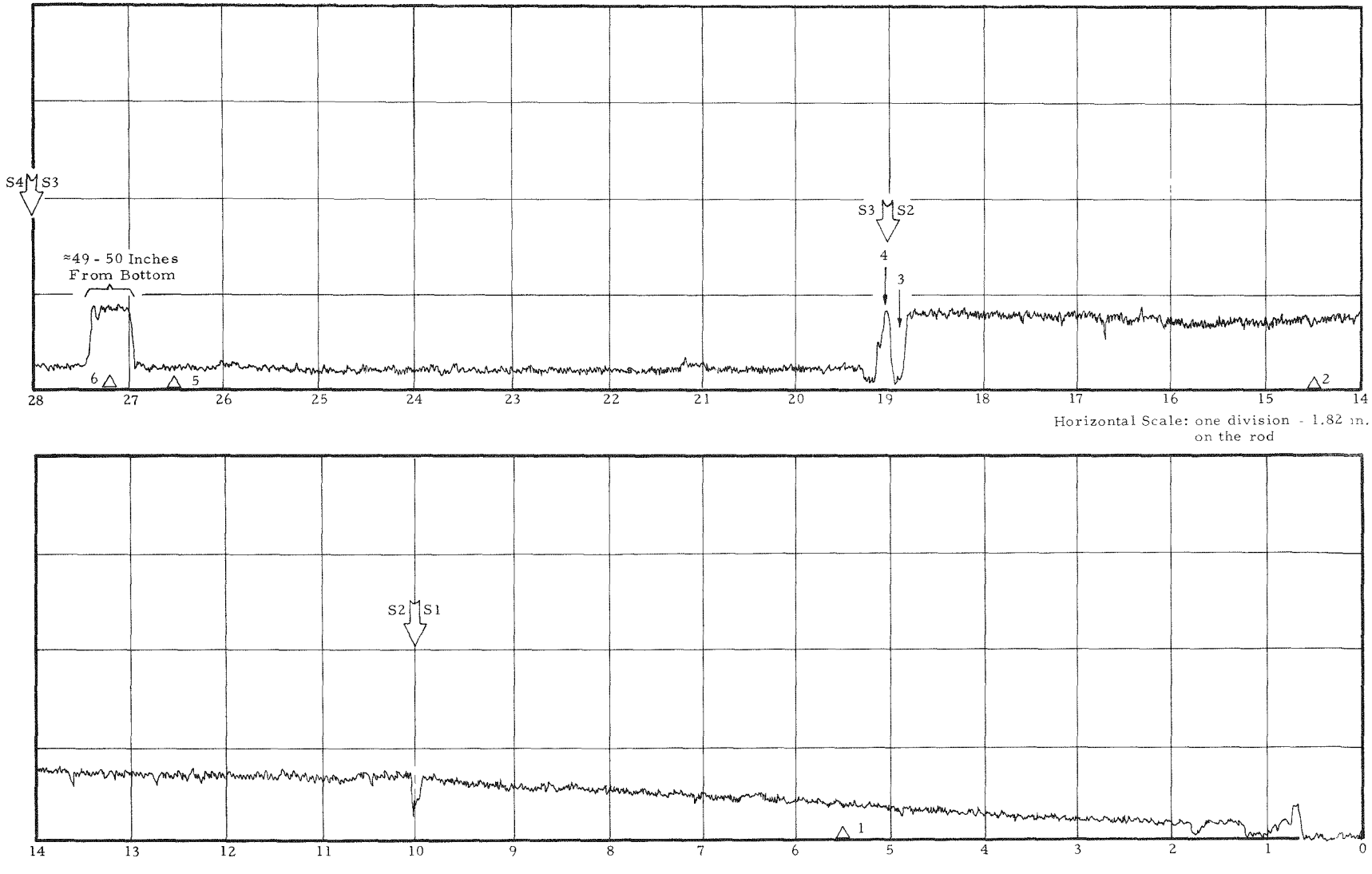

Figure 4-14. (Cont'd)

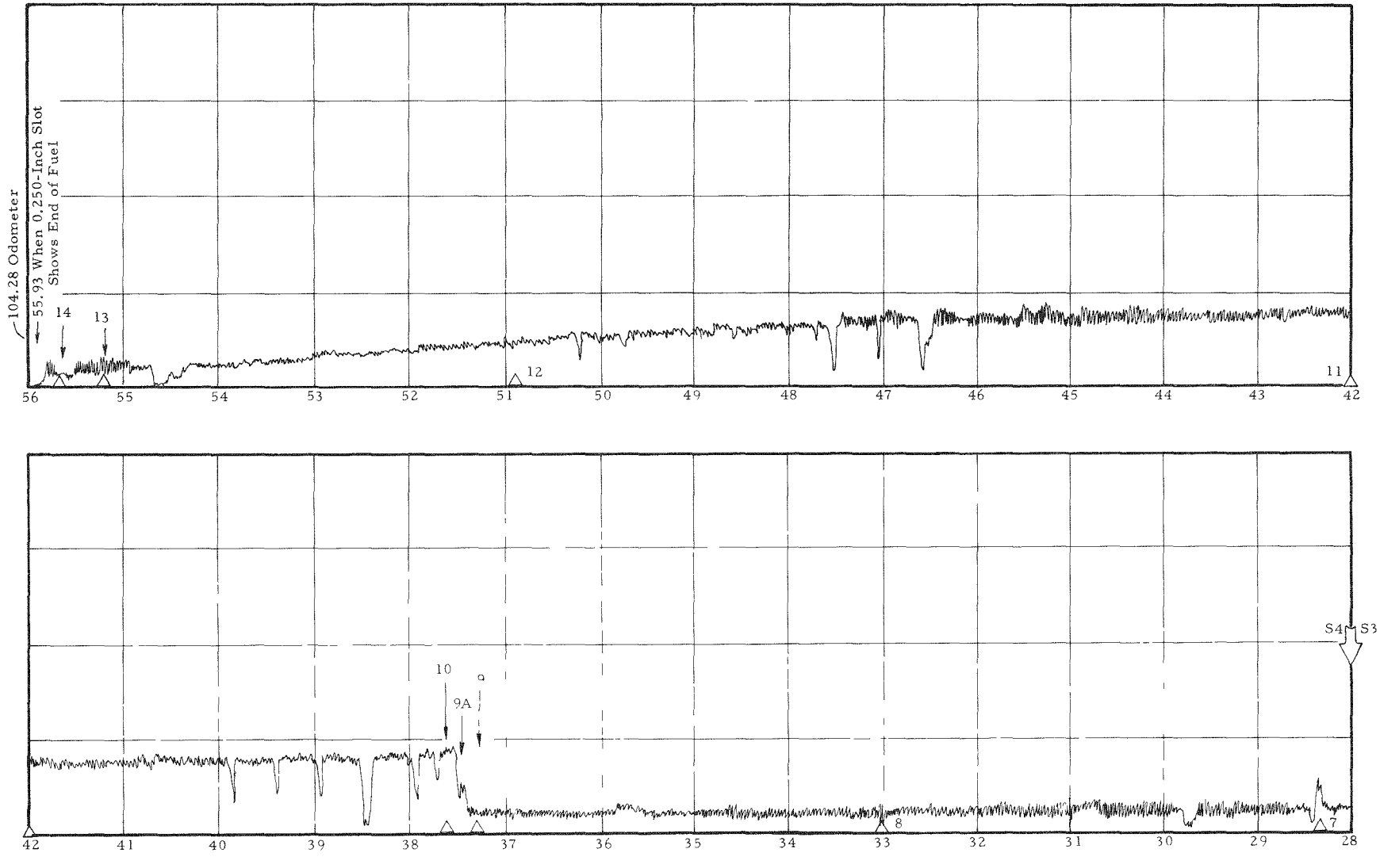

Figure 4-15. Gross Gamma Profile of Fuel Rod 105A, Scanned Bottom to Top

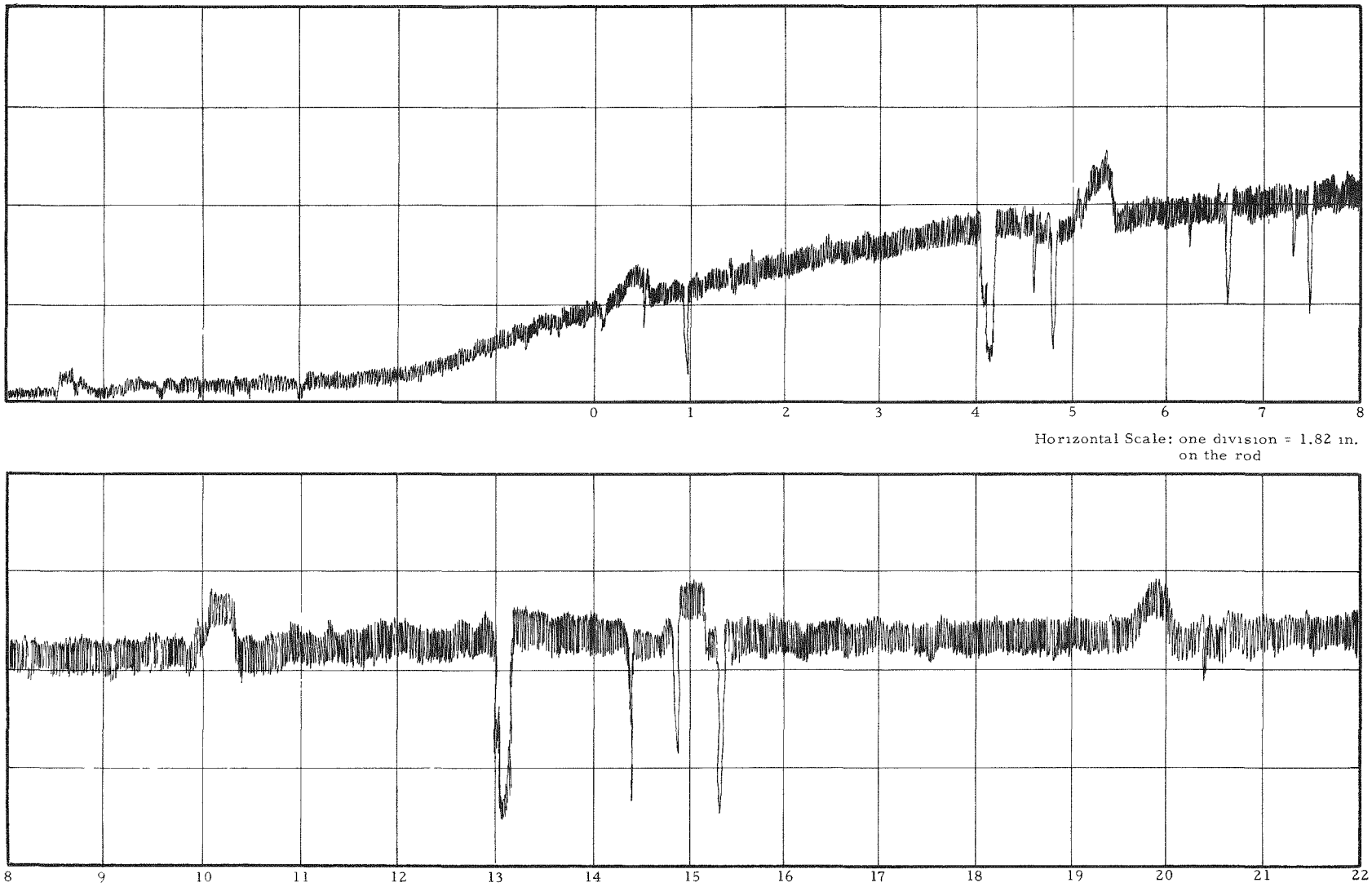

Figure 4-15. (Cont'd)

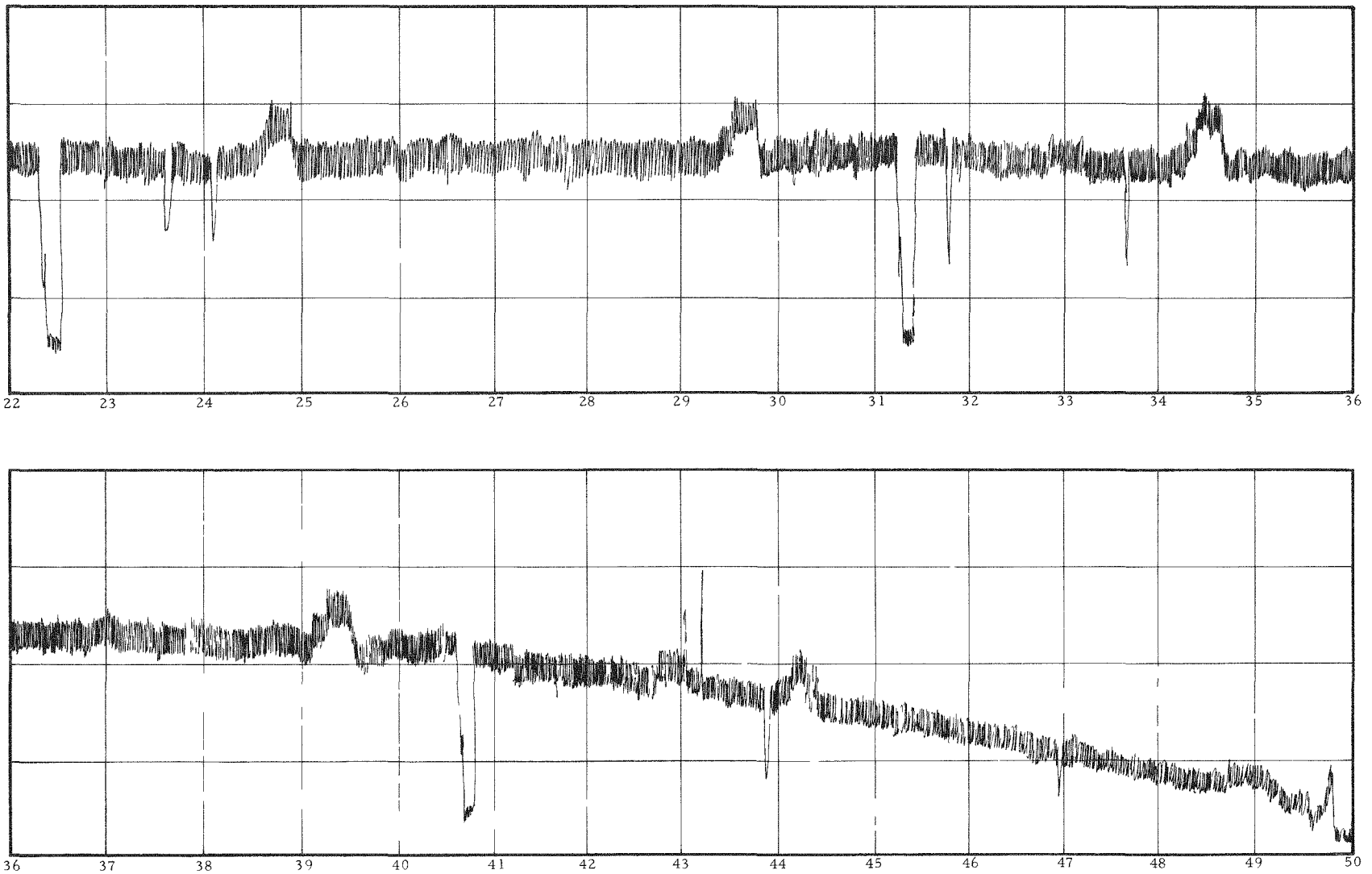

Figure 4-16. Gross Gamma Profile of Fuel Rod 105A, Scanned Top to Bottom

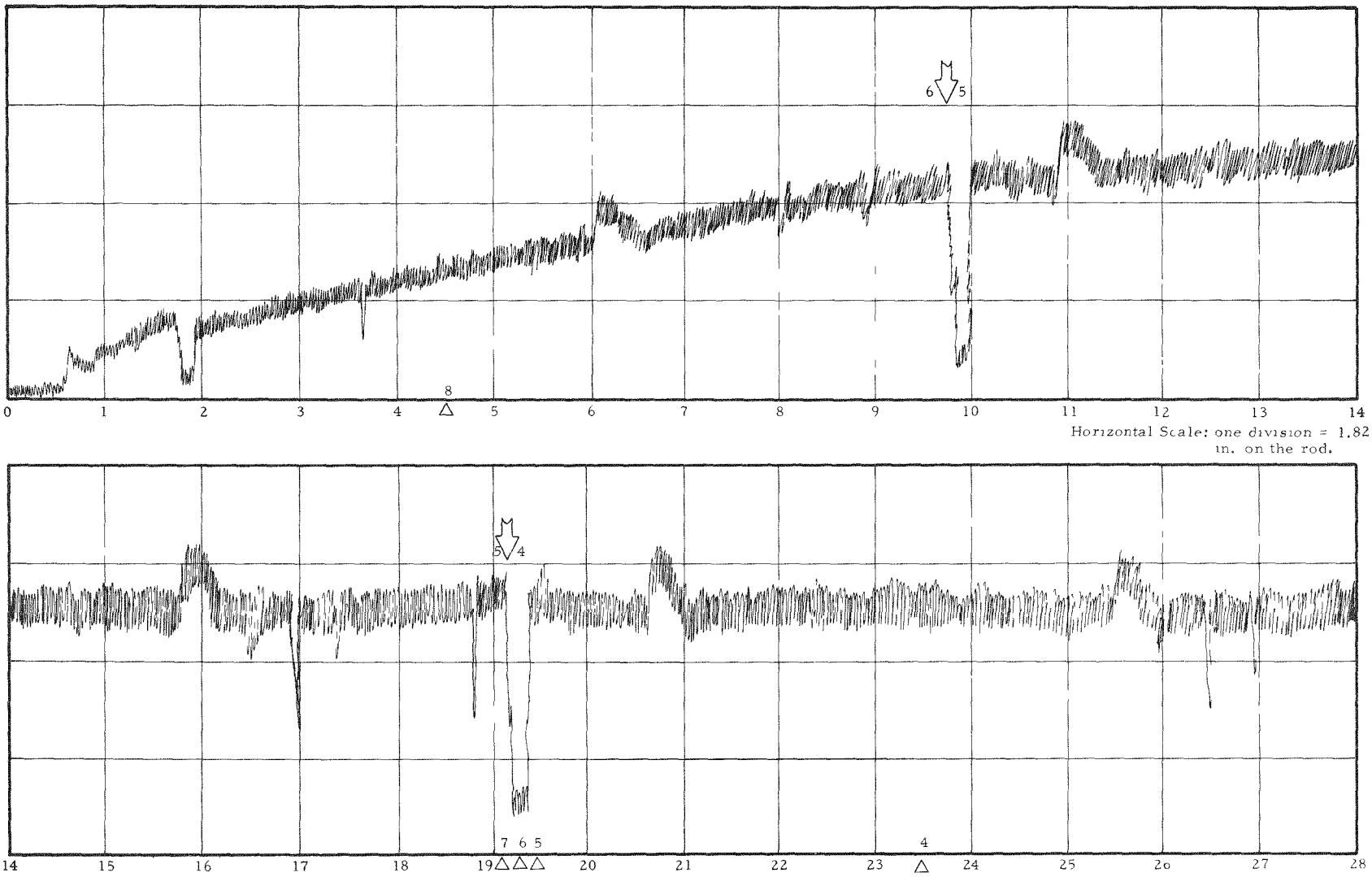

Figure 4-16. (Cont'd)

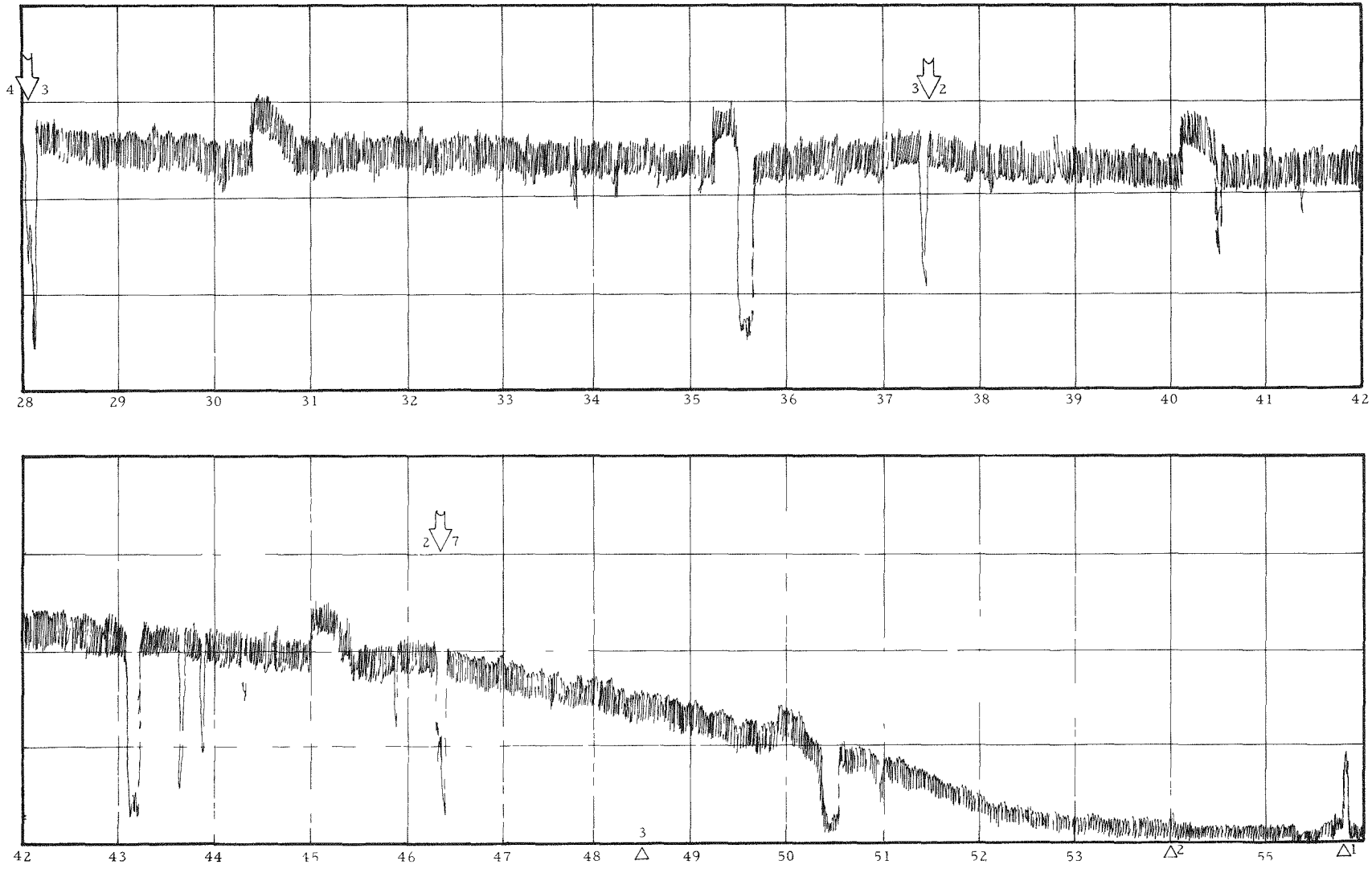

5. ThO_2-UO_2 FUEL EXAMINATION

5.1. Fission Gas Release

5.1.1. Purpose

The pressure created by the fission gases released from the fuel is a major consideration in the design of the fuel rods. Conservatively high fission gas release percentages were generally used because of the lack of applicable data. Because of this lack it was considered advantageous to obtain these data on the amount of gases released from ThO_2-UO_2 for the fuel rods examined.

5.1.2. Scope

Initially, it was planned to collect and analyze the gases within all of the fuel rods. As mentioned in section 4.1.4, nine of the 13 rods were punctured during removal from the fuel bundles. Thus the fission gas analyses were limited to four fuel rods: 105D, $105D_1$, 105E and 105F.

5.1.3. Procedure

The gas collecting system consists of an in-cell puncture device connected to an out-of-cell vacuum collection system. One end of the rod was sealed in a set of puncture blocks lined with neoprene gaskets and the system was evacuated to a pressure of less than 1.0 micron. The vacuum system was shut off and the leak rate determined. If the maximum leak rate was less than 0.5 micron/minute, the rod was punctured with a sharp pin. The gases within the fuel rod (V_x) were allowed to diffuse into the evacuated system, which had a known volume (V_1). When the system achieved equilibrium, the gas pressure (P_1) within the system was measured. The gases within the fuel rod (V_x) and the known volume (V_1) were allowed to diffuse into another system of known volume (V_2). When the system achieved equilibrium, the gas pressure (P_2) within the system was measured. By solving the following

two equations, the pressure (P_x) and volume (V_x) in the fuel rod can be calculated:

$$V_x P_x = P_1(V_1 + V_x). \quad (1)$$

$$V_x P_x = P_2(V_1 + V_2 + V_x). \quad (2)$$

$$V_x P_x = P_1(V_1 + V_x) = P_2(V_1 + V_2 + V_x).$$

Since P_1, P_2, V_1, and V_2 are known, $P_x V_x$ can be calculated.

A known quantity of the collected gas was removed for analyses by gamma counting and mass spectrometry.

5.1.4. Results

The results of the fission gas analyses on the four rods are reported in Tables 5-1 through 5-3. Because of the small void volume within the rods, compared with the total volume of the system, the measured void volumes varied considerably with only minor errors in the pressure reading. Therefore, these results were discarded. The amount of helium in the collected gases is somewhat greater than that initially loaded into the rods. This excess helium could have been generated from tertiary fissions within the fuel or released from the cladding. About 27 cc of helium are generated in the cladding of each rod by the n,α reactions with the boron-10. Because there are two possible sources of this helium, it is impossible to determine the manner of its release.

The Xe:Kr ratio varied among the four specimens from a low of 5.1 to a high of 7.2. The average ratio of the four would be about 6.2, which is not inconsistent with that observed in other thermal reactors; values from 6.5 to 7.4 were reported for the VBWR, [1] and values from 6.3 to 8.5 were reported for the Yankee fuel rods. [2]

Table 5-1. Results of Fission Gas Puncture

Rod No.	Gas content, cc (STP)	Calculated rod pressure, mm Hg[(a)]
105D	7.75	1987
$105D_1$	9.45	2357
105E	9.24	2336
105F	5.46	1385

[(a)] Based on calculated void volume of 3.02 cc.

Table 5-2. Composition of Gases According to Mass Spectrometer

Rod No.	Volume, %			Xe:Kr ratio
	Helium	Xenon	Krypton	
105D	51	41	8	5.1
$105D_1$	40	52	8	6.5
105E	64	31	5	6.2
105F	80	18	25	7.2

Table 5-3. Percent Fission Gas Release

Rod No.	Average rod burnup, MWd/MTM	Fission gas vol, cc		Amount released, %
		Produced	Released	
105D	11,000	236	3.8	1.6
$105D_1$	11,000	236	5.7	2.4
105E	15,500	334	3.3	1.0
105F	5,000	110	1.1	1.0

5.2. Fuel Rod Sectioning

5.2.1. Purpose

The 13 fuel rods were sectioned to obtain specimens of the cladding for the tensile tests, specimens for the metallographic examination of the fuel and cladding, sections of the rods for the profilometer measurements, samples of the fuel for burnup and isotopic analyses, and samples of the cladding for examination at Ohio State University and Battelle Memorial Institute.

5.2.2. Scope

The locations and types of specimens obtained from all 13 fuel rods are shown schematically in Figure 5-1.

5.2.3. Procedure

Because of the close spacing of the ferrules (about 9 inches apart), it was not possible to obtain sections of the fuel rods more than 8 inches in length. The segments of the fuel rods between the ferrules were cut with a motorized tubing cutter. Individual specimens were then obtained from these short segments, using either a fine abrasive cutoff wheel or the motorized tubing cutter.

5.2.4. Results

The sectioning of the rods proceeded without any difficulty. In some instances, however, entire fuel pellets came out of the rod segments. Figure 5-2 shows two views of a fuel pellet removed from rod 105C; this pellet achieved an estimated burnup of 15 GWd/T. Irradiation altered neither the shape of the pellet nor the enrichment identification mark ("C").

A side view of a series of three pellets removed from another portion of rod 105C is shown in Figure 5-3. The ability to remove apparently undamaged pellets was not limited to the "C" fuel, since it was possible to remove entire pellets from all fuel rods examined regardless of their enrichment or burnup. The fact that fuel pellets could be removed from the cladding further substantiates the results of the gamma scanning, which indicated minimal distortion of the pellets during irradiation from cracking or swelling.

5.3. Metallography

5.3.1. Purpose

The fuel and cladding were examined to determine whether there were any thermally, chemically, or radiation-induced changes in the microstructure. The cladding is discussed further in section 6. From the resulting microstructures and operational data, deductions can be made regarding the overall thermal performance of the fuel. In addition, it might be possible to correlate the amount of fission gas release with the post-irradiation microstructure.

5.3.2. Scope

Samples of fuel from the fuel rods were metallographically examined in detail. The sites from which the samples were obtained and the purpose of the examinations are listed in Table 5-4.

Table 5-4. Locations From Which Samples Were Taken

Rod No.	Location of specimen, in. from bottom	Purpose
20A	35	Examine spacer
61A	15	Examine fuel
	48	Examine fuel
105A	13	Examine fuel
	35	Examine fuel
	47	Examine ferrule
	48	Examine fuel
105B	15	Examine fuel
	48	Examine fuel
105C	15	Examine fuel
	48	Examine fuel
105D	15	Examine fuel
	48	Examine fuel
105E	15	Examine fuel
	48	Examine fuel
105F	30	Examine fuel
	52	Examine fuel
	53	Examine fuel and determine enrichment of misplaced pellet
106A	15	Examine fuel
	45	Examine ferrule
	48	Examine fuel
	51	Examine spacer
106B	15	Examine fuel
	42	Examine fuel

5.3.3. Procedure

The metallographic specimens were vacuum-impregnated with epoxy, mounted in cold setting compound, and finely polished. The fuel was then examined in the as-polished condition to determine the general appearance and to locate any areas of unusual appearance. A 250× photomosiac of the as-polished fuel from centerline to cladding surface was prepared. Photomicrographs of areas of unusual appearance were also obtained.

Because standard etchants failed to bring out the grain structure, some effort was devoted to developing a suitable etchant for this fuel. Satisfactory results were obtained using the following solution:

90cc H_2O, 10cc H_2SO_4, and 5 drops
HF at 150 F for 1 to 10 minutes

Unfortunately, the funds for the program had been exhausted by the time a satisfactory etchant had been developed, and only two specimens were examined in the etched condition.

5.3.4. Results

The metallographic examination indicated that there were some metallic appearing inclusions in all types of fuel. Typical examples of various sizes and shapes of inclusions are shown in Figure 5-4. It is believed that these inclusions were introduced during fabrication, since relatively large agglomerates were found in the pure ThO_2. The low burnup achieved by the ThO_2 (2 GWd/T) essentially eliminates fission product accumulation as the source of inclusions. Furthermore, most of the available data indicate that fission product agglomeration begins to occur at temperatures similar to that required for void migration.[3] The fact that neither columnar grain growth nor significant migration occurred in any of the fuel rods not only indicates that the centerline temperatures were considerably below 1800 C, but also precludes the possibility of the migration of solid fission products. Funding limitations prevented positive identification of the inclusions and of the low probability that they were caused by irradiation.

Figures 5-5 through 5-10 are photomosiacs of typical irradiated fuels in the as-polished condition. A significant amount of pullout of the fuel occurred during polishing. There were no major changes in the fuel microstructure regardless of the burnup or the heat rate. Figure 5-8 is a photomosiac of the etched fuel (type A) taken 15 inches from the bottom of fuel rod 61A. One other etched sample (rod 105A, 35 inches from bottom) was examined, but meaningful results could not be obtained because of the severity of pullout that occurred during polishing and etching.

Near the center of the fuel pellet shown in Figure 5-6 some of the porosity migrated toward the grain boundaries; however, even at the center of the fuel rod, some porosity still exists within the grains. There is an agglomerate of unusual-appearing material present at this sample; it is believed to be the remnants of a piece of previously sintered fuel. During fabrication, the fired density was controlled by mixing the active powder with powder obtained from crushing sintered pellets. During subsequent sintering of this fuel mixture, the characteristics of the previously sintered material apparently were not erased.

The sizes of the grains within the specimen shown in Figure 5-6 were determined at several different locations. These measurements indicated that there was no significant change in grain size during irradiation. Since there were no changes in the grain size, it is almost impossible to determine the peak centerline temperature achieved during irradiation.

Figure 5-1. Sectioning Diagram for Thirteen ThO_2-UO_2 Fuel Rods

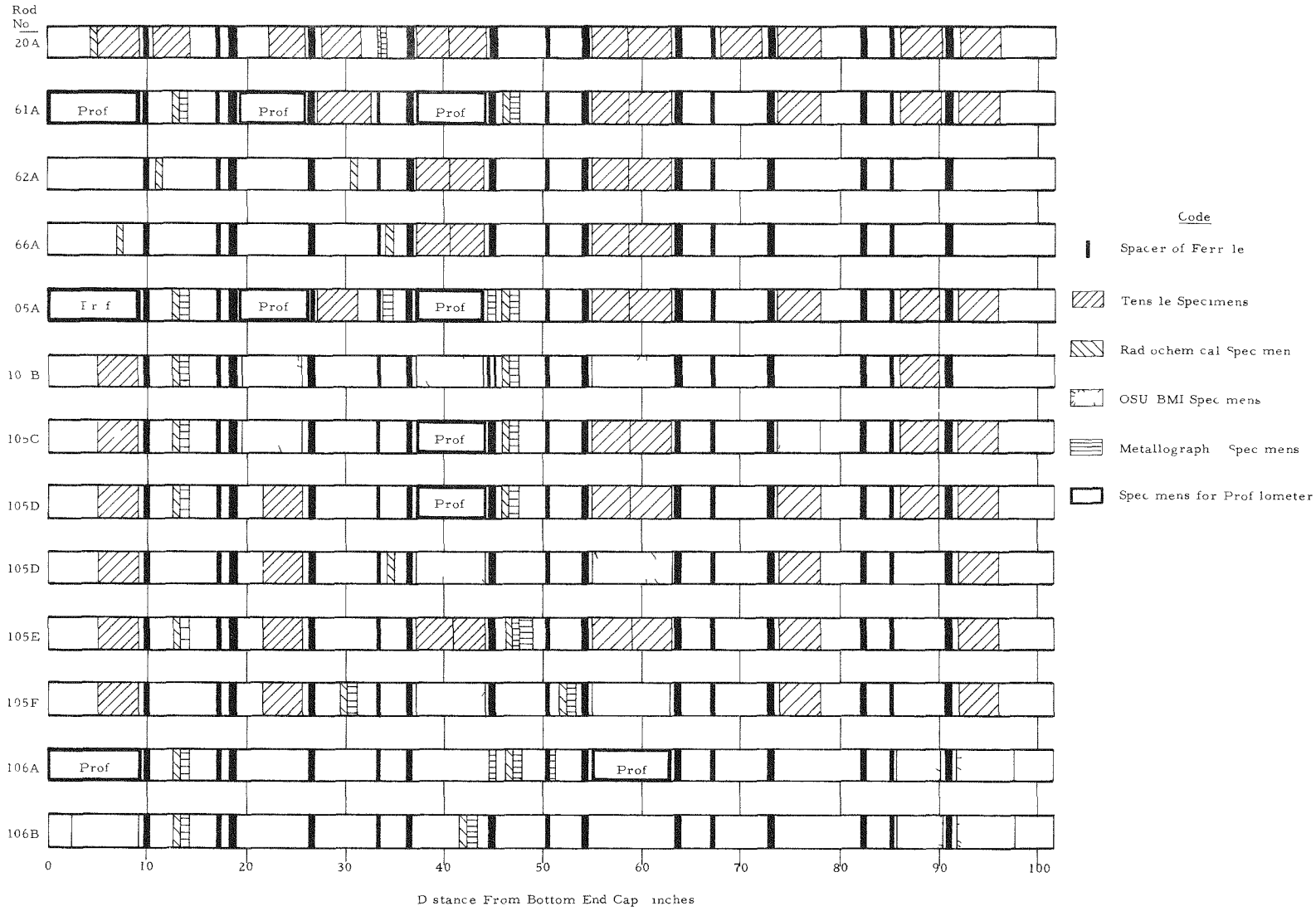

Figure 5-2. End and Side Views of Irradiated Thoria-Urania Pellet

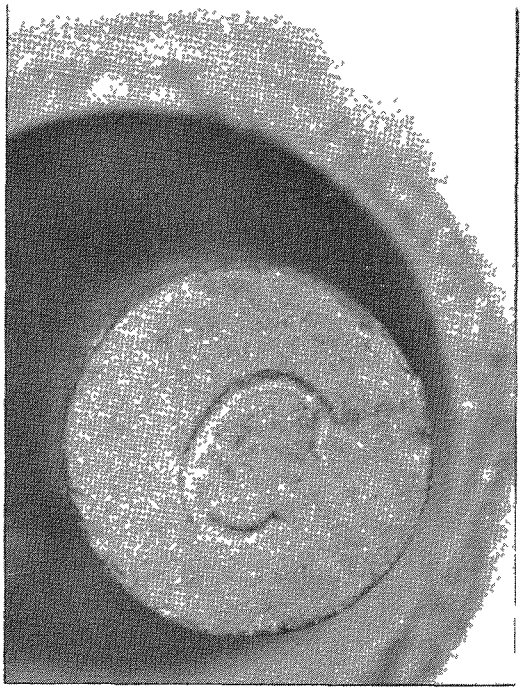

End View

(Tubular piece is a support, not the cladding.)

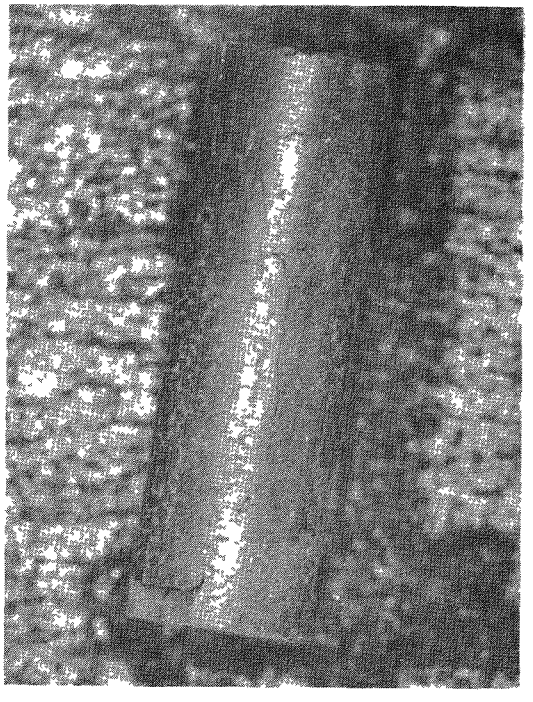

Side View

(Pellet Diameter: ≈0.260 inch;
Pellet Length: ≈0.750 inch)

Figure 5-3. Side View of Three Irradiated Thoria-Urania Pellets

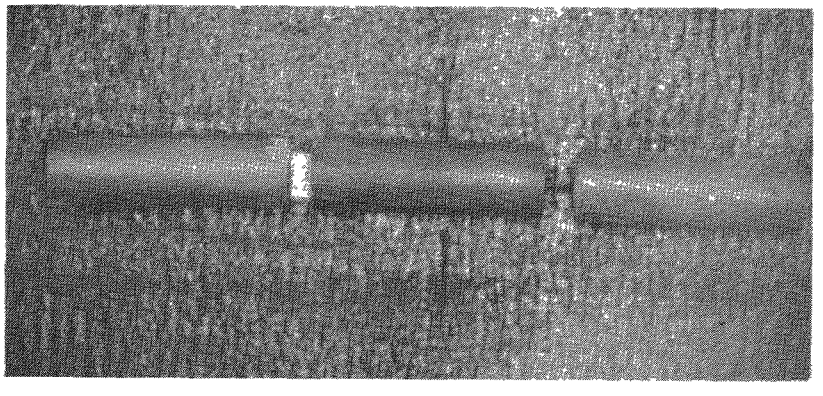

(Pellet Diameter: ≈0.260 inch;
Pellet Length: ≈0.750 inch)

Figure 5-4. Metallic Inclusions in Thoria-Urania Fuel (As-Polished, 250X)

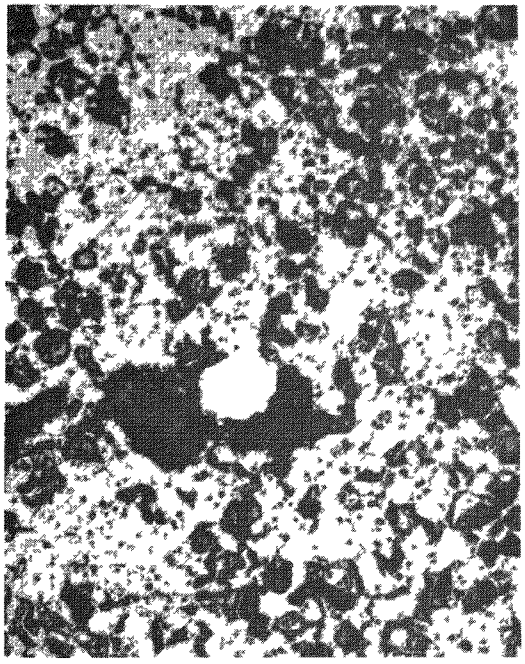

Rod 105A

(ThO_2 - 3% UO_2, Peak Rod Burnup 22 GWd/T)

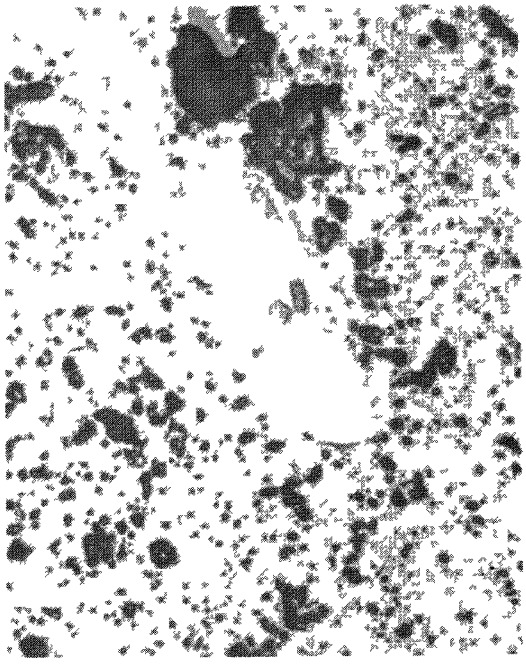

Rod 105C

(ThO_2 - 5.5% UO_2, Peak Rod Burnup 15 GWd/T)

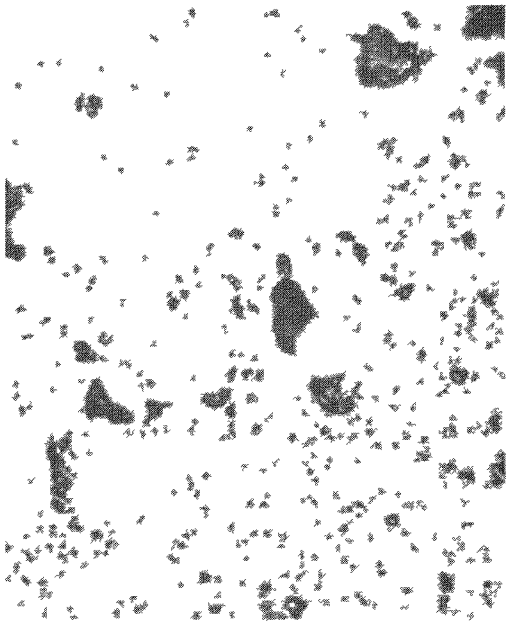

Rod 105F

(Pure ThO_2, Peak Rod Burnup 2 GWd/T)

Figure 5-5. Photomosaic of Fuel From Peak Flux Location of Fuel Rod 61A

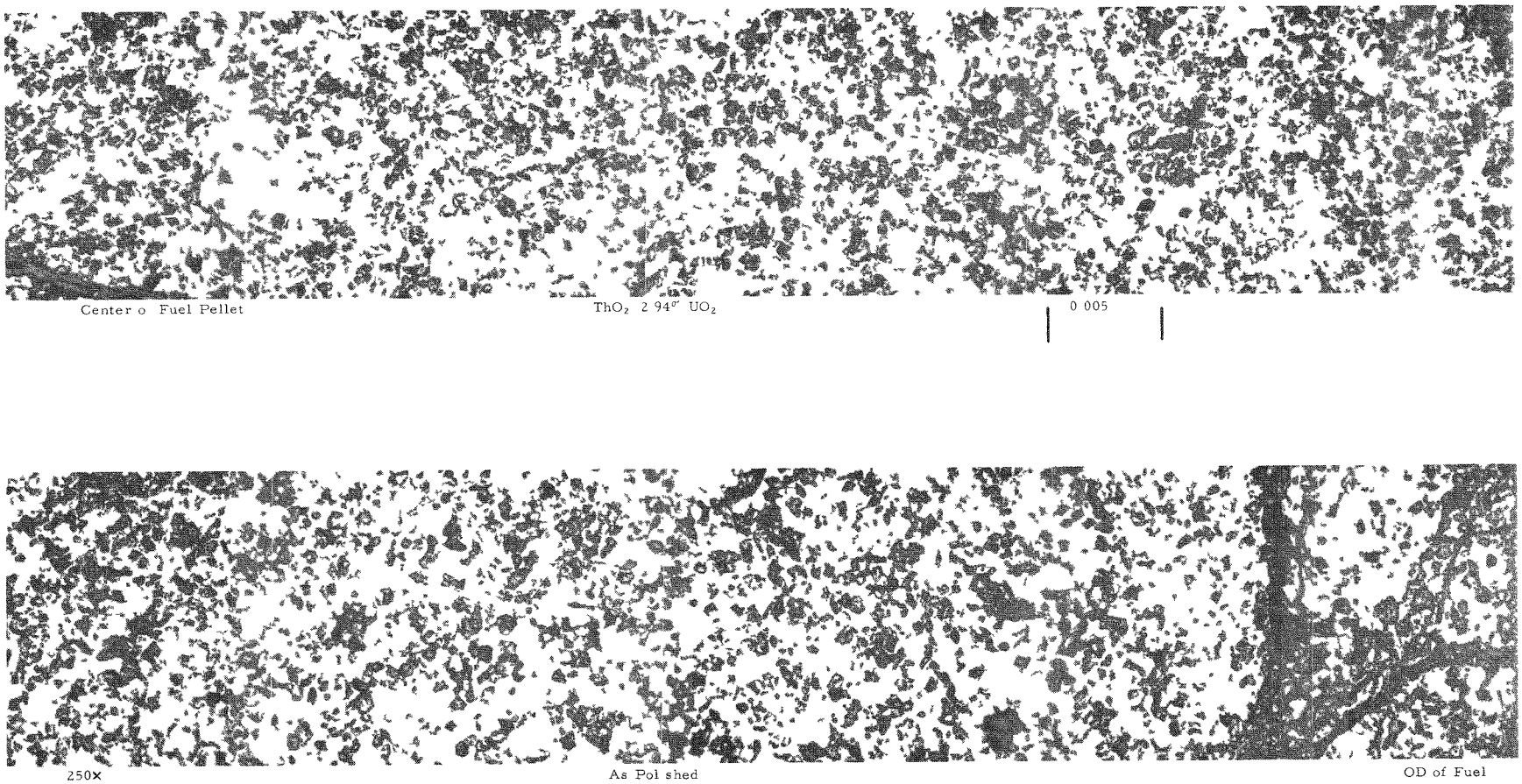

Figure 5-6. Photomosaic of Fuel From Average Flux Location of Fuel Rod 61A

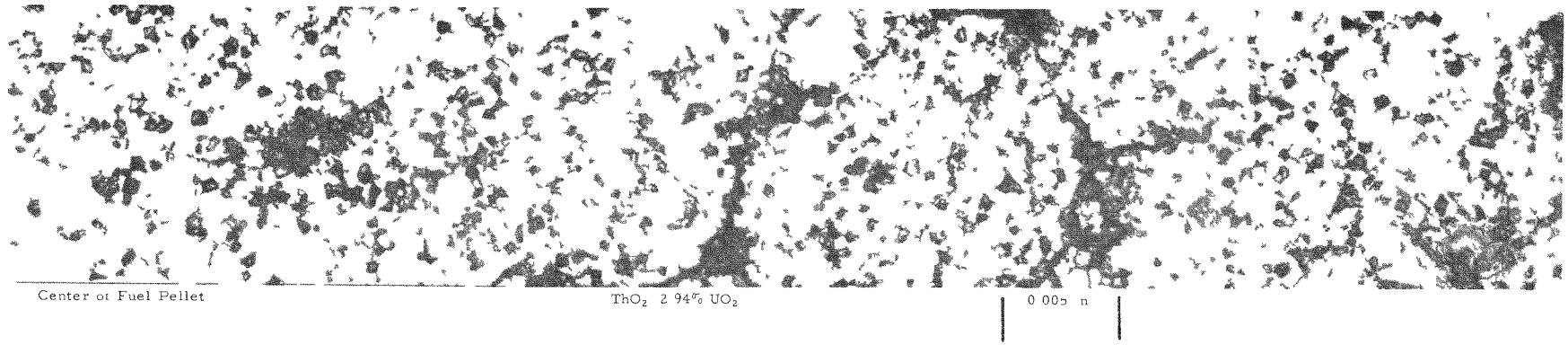

Figure 5-7. Photomosaic of Fuel From Peak Flux Location of Fuel Rod 105A

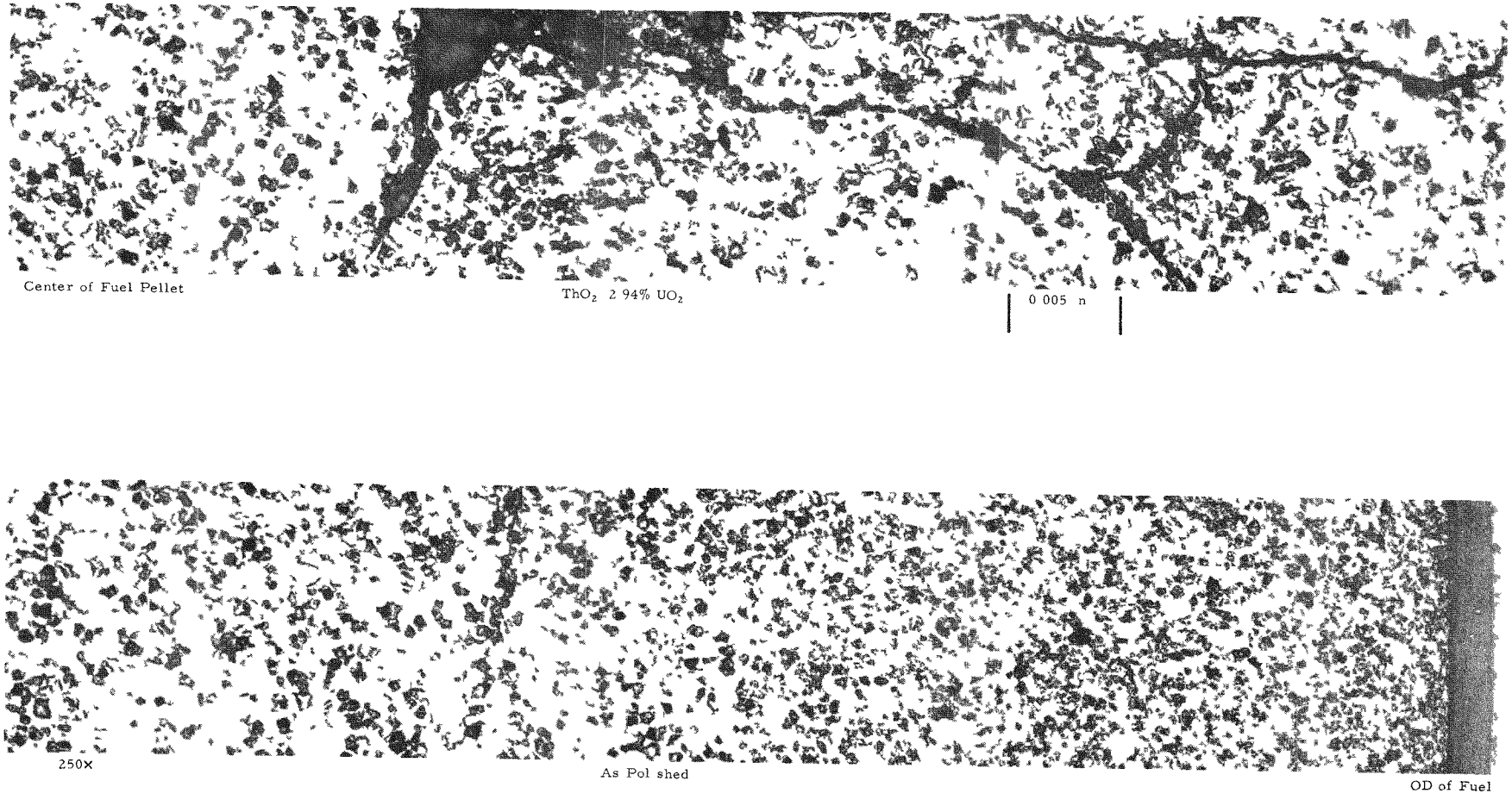

Figure 5-8. Photomosaic of Fuel From Peak Flux Location of Fuel Rod 105C

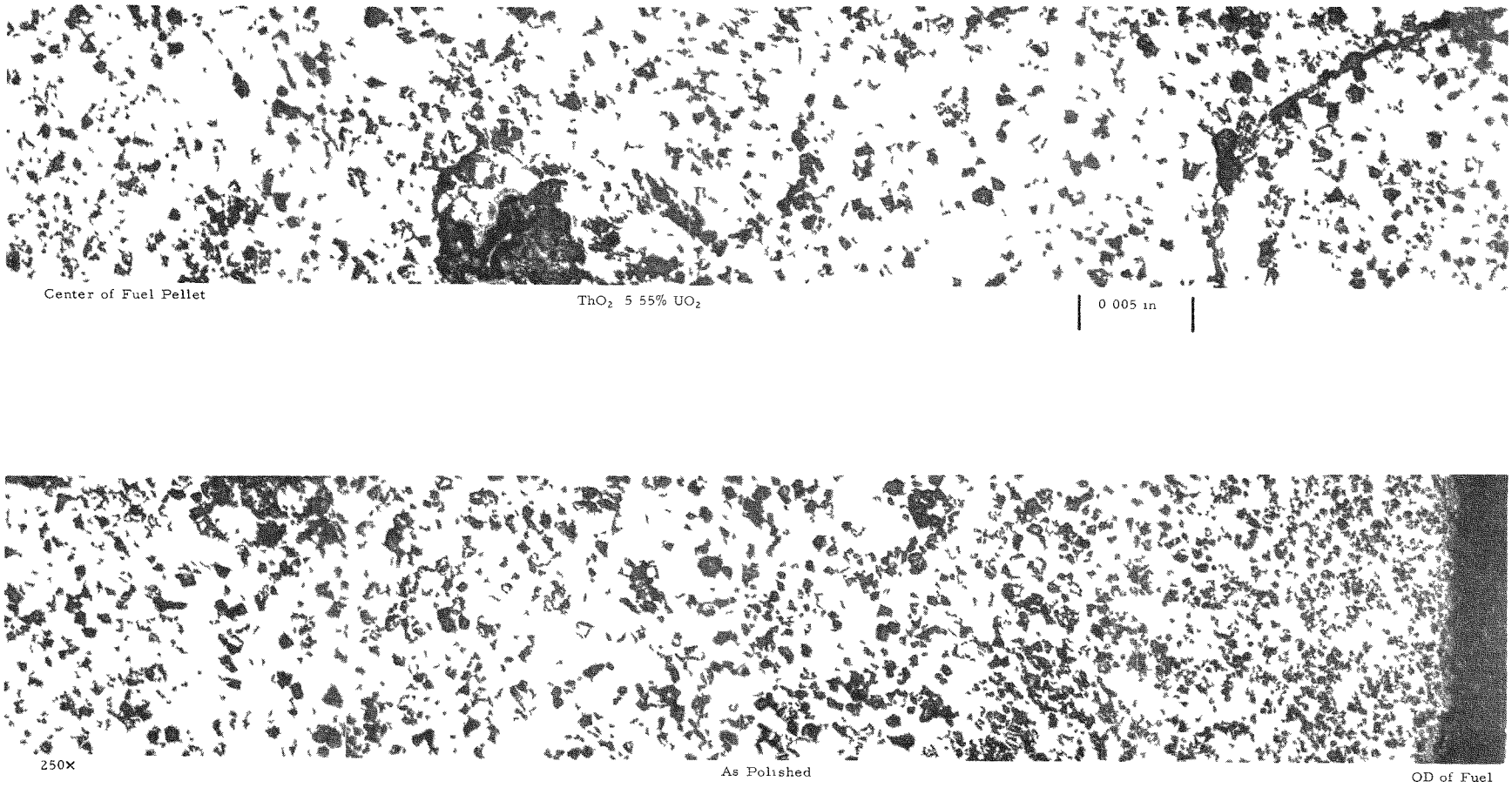

Figure 5-9. Photomosaic of Fuel From Low Flux Region of Fuel Rod 106A

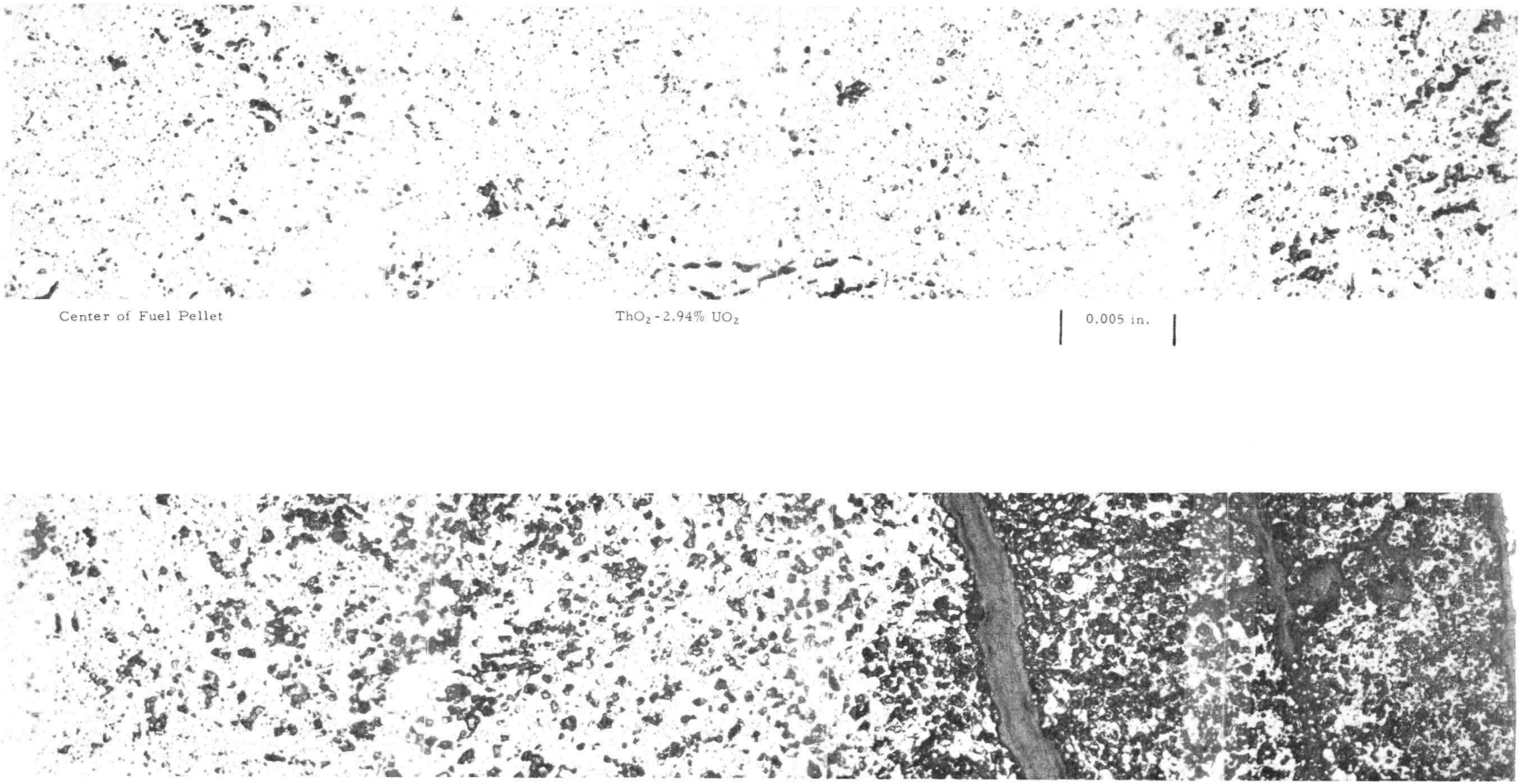

Figure 5-10. Photomosaic of Fuel From Peak Flux Location of Fuel Rod 105F

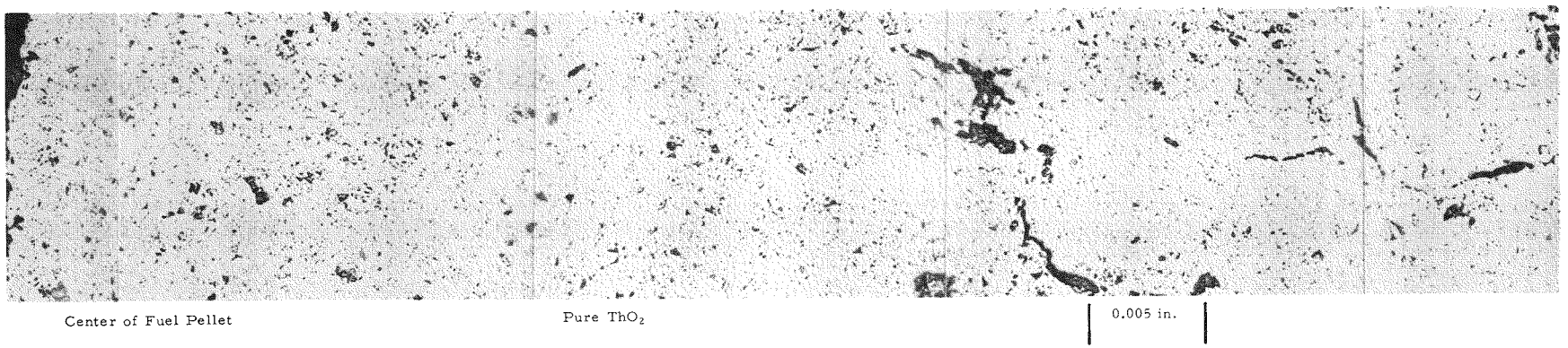

6. CLADDING EXAMINATION

6.1. Metallography

6.1.1. Purpose

The cladding was examined metallographically for the reasons described for the examination of the fuel in section 5.3.1.

6.1.2. Scope

Both the fuel and the cladding were examined in all of the metallographic specimens, and the scope of the metallographic examination of the cladding is the same as that described for the fuel in section 5.3.2.

6.1.3. Procedure

The cladding and fuel were examined in the as-polished condition at the same time. After the fuel had been examined in the etched condition, the specimens were repolished to remove any stains on the cladding caused by the etching of the fuel. After repolishing, the cladding was electrolytically etched using a 10% oxalic acid solution. During the etching, the voltage varied from 8 to 15, amperage varied from 1.5 to 2.5, and the etching time varied from 6 to 15 seconds, depending on the particular sample. Throughout the examinations photomicrographs and photomacrographs of typical and unusual-appearing areas were obtained.

6.1.4. Results

6.1.4.1. Cladding

The metallographic examination confirmed the conclusion of the visual examination that the outside surface of the cladding was unaffected by the exposure in the reactor. The dark gray oxide film observed in the visual examination could not be detected during the metallographic examination.

The examination did indicate that there was a large quantity of precipitates in the grain boundaries of the cladding, as shown in Figure 6-1. The large number of grain boundary precipitates was not unexpected, since the cladding contained about 250 ppm of boron, which generally precipitates at the grain boundaries. Furthermore, during the brazing operation, the cladding was at 800 to 1300 F for a considerable length of time. In this temperature range, the carbon and boron have a strong tendency to precipitate at the grain boundaries as carbides and borides.

During the examination, considerable porosity was found on the inside surface of the cladding from most of the fuel rods. This porosity assumed a variety of shapes, including small radial cracks, irregular voids, and spheres. The zone of porosity was generally limited to about 0.001 inch in thickness, but occasionally penetrated as deep as 0.002 inch. Typical examples of the types of voids observed in several samples are shown in Figures 6-2 and 6-3.

There was no evidence of interaction between the fuel and cladding that might have caused the voids. Furthermore, the type of fuel did not appear to have any effect on the formation of the voids. Voids were not observed in the cladding adjacent to the pure ThO_2 (rod 105F), as shown in Figure 6-4. The fast and thermal fluence for rod 105F are similar to those received by other rods in fuel bundle 105. Voids were observed in fuel rod 106A but not in rod 61A, as shown in Figure 6-5.

Examination of archive specimens of cladding that was similar to that used in the fuel rods did not reveal any voids (Figure 6-6). Unfortunately, there were no archive specimens available that were identical to the cladding in the bundles. The material that was examined came from a dummy bundle of unknown origin which was used to develop brazing techniques; thus, precise knowledge of the cladding in the unirradiated condition is not available. Most of the defects found in the irradiated cladding would not have been cause for rejection of the cladding during ultrasonic inspection, since they were less than 0.002 inch in depth, which is the specified limit.

At this time there is no logical explanation for the void formation. Because good archive specimens are not available,

one is not certain whether the voids were present in the unirradiated cladding or whether they occurred during irradiation.

6.1.4.2. Ferrules

Two ferrules were selected for detailed metallographic examination. They came from locations on rod 106A that had achieved burnups of about 6 and 22 GWd/T. By examining these two ferrules with wide variation in total fast and thermal fluences, it should be possible to determine whether the total fluence received by the ferrule had any significant effect on the performance of the braze joint.

A photomacrograph of the cross section of a fuel rod 106A as the ferrule is shown in the left-hand portion of Figure 6-7. Two areas within one of the braze joints are also shown. Figure 6-8 is a photomosiac of an entire braze joint. These two figures are representative of the information obtained from fuel rods 106A and 105A.

In most of the braze joints there is some cracking and porosity in the vicinity of the meniscus. This cracking and porosity is observed in the as-fabricated braze joints and is caused by shrinkage of the molten braze alloy during solidification. Figure 6-9 is a photomicrograph of an unirradiated braze joint showing even more severe cracking.

The examination of these two ferrules indicated that the braze joints were not affected by operation in the reactor. There was no evidence of excessive corrosion or deterioration of the joints during operation. Furthermore, there were no visible differences in the appearance of the braze joints in rods 106A and 105A, in which the total fluences received varied by a factor of at least 3.

6.1.4.3. Spacer

Internal spacers were inserted into the fuel rods to segment the fuel column and the fission gas plenum. By segmenting the fuel column, the problem of ratcheting and fuel slumping could be minimized. These spacers (type 304 stainless steel) were about 0.125 inch long and were spaced at intervals of about 16 inches along the length of the fuel rod. The spacers were held in position by rolling the cladding into a circumferential groove machined into the spacer and by brazing the spacer to the cladding.

One spacer from the peak heat flux location of fuel rod 20A was examined to determine the condition of both spacer and cladding after operation in the reactor. Photomicrographs of the spacer and of selected areas of the cladding in the vicinity of the spacer are shown in Figure 6-10, and a photomosiac of half of the spacer is shown in Figure 6-11. The outside surface of the cladding at the spacer location was in excellent condition, as shown in Figure 6-11. There was no evidence of cracking, excessive corrosion, or crud buildup in the depression created by rolling the cladding into the spacer.

Porosity was found on the inside surface of the cladding and voids at a short distance from the spacer. This porosity was similar to that described in section 6.1.4.1. Other cladding areas near the spacer were coated with braze alloy. It was hoped that the examination of the cladding beneath the braze might help to determine whether the voids and porosity were created by irradiation or were present in the unirradiated cladding. Because of the great solubility of the cladding in the braze, it was impossible to determine whether the heavy penetration of the braze metal into the grain boundaries was caused by a chemical reaction or occurred because of porosity in the as-received cladding. Thus, the examination of the spacer did not aid in determining the cause of the porosity in the cladding.

The examination of the spacer did indicate that their presence did not adversly affect the operation of the fuel rod. The effectiveness of the spacer for minimizing ratcheting and slumping was not determined, because there was little mechanical interaction between the fuel and cladding and because fuel melting did not occur.

6.2. Tensile Properties

6.2.1. Purpose

The tensile testing of the borated stainless steel cladding was performed to investigate the effects of irradiation on its strength and ductility. Within the past few years it has been theorized that the loss of ductility in irradiated austenitic stainless steel at temperatures above 500 C was caused by the accumulation of helium at the grain boundaries.[4] This helium is produced by the n,α reaction between boron-10 and various elements in stainless steel—particularly iron, nickel, and

nitrogen. The high boron content (about 250 ppm) in the cladding from these rods should help to determine whether the loss in high temperature ductility can, indeed, be related to the helium or is caused by some other fast neutron reaction. Therefore, specimens of the cladding were tested at a number of temperatures to determine their ductility.

6.2.2. Scope

The scope of the tensile testing program is shown in Table 6-1. The data obtained from the tests conducted at 70 and 600 F provide information on the properties of the cladding that are of interest to thermal reactor designers. The other data were obtained to determine the effects of the high helium content on the elevated-temperature properties of the steel. Some of the irradiated specimens were annealed at 1832 F for one hour to eliminate essentially all displacement-type defects and thus evaluate more precisely the contribution of the helium to the loss in ductility. The unirradiated specimens, both as-received and annealed, provide a base line for the interpretation of the data.

6.2.3. Procedure

Four-inch sections of the fuel rods were obtained by cutting the rods with a motorized tubing cutter. Semi-cylindrical sections of the cladding were obtained by slitting the sections of the fuel rod in the axial direction. These slitting operations were performed with a fine abrasive cutoff wheel. The semi-cylindrical sections of cladding were deburred and the gage length machined using a Tensile Kut machine with a special jig adapted for this size tubing. Figure 6-12 shows a finished tensile specimen.

The tensile specimens that were annealed were soaked for one hour at 1832 F and then water quenched. Oxidation of the specimens during annealing and quenching was minimized by packing the specimens in Sen-Pak envelopes which are especially designed to prevent oxidation.

Suitable grips and extensometers had to be developed for these subsized and semi-cylindrical specimens. Figures 6-13 and 6-14 are photographs of the grips containing a specimen and of the extensometer. All specimens were tested at a strain rate of 0.02 per minute, the extensometer being attached to the specimen throughout the test. Typical load deflection curves for unirradiated and irradiated specimens

are shown in Figures 6-15 and 6-16. Typical photographs of the fractured specimens are shown in Figures 6-17 and 6-18.

6.2.4. Results

6.2.4.1. Unirradiated Cladding

The results of the tensile tests conducted on unirradiated specimens that were annealed are shown graphically in Figures 6-19 through 6-22. After annealing, the yield and tensile strengths (Figures 6-19 and 6-20) of as-received, 3000- and 6000-hour thermally aged specimens decrease as the temperature increases from 70 to 750 F. Little difference is observed in the yield strength of the specimens tested in the range from 750 to 1000 F. The yield strength, regardless of the previous thermal history of the material, increased with increasing temperature from 1000 to 1300 F. The peak in the yield strength-versus-temperature curves is more pronounced for the 6000-hour thermally aged material than for the 3000-hour thermally aged or the as-received material. The normal softening trend, as indicated by the decrease in strength with increasing temperature, is regained above 1300 F, and at 1450 F (the maximum test temperature used in this program) the yield strength is approximately the same as that at 900 F. The ultimate tensile strength-versus-temperature curves for these materials do not show a peak. There is little difference in the tensile strength of material tested at temperatures from 750 to 1200 F.

The total elongation of the as-received, 3000- and 6000-hour thermally aged material (Figures 6-21 and 6-22) rapidly decreases as the test temperature increases from 70 to 600 F. At 600 F, the total elongation begins to increase with increasing temperature until a peak in the total elongation occurs at 850 F. The total elongation then decreases as the temperature increases from 850 to 1450 F.

Figures 6-23 through 6-26 represent the strength and ductility of as-received, 3000- and 6000-hour thermally aged materials that were not annealed. Since data for this material were obtained only at 70, 600, and 1200 F, insufficient data are available to draw curves like those in Figures 6-19 through 6-22.

The yield and tensile strengths of these materials decrease as the test temperature increases from 70 to 1200 F (the

maximum temperature used in testing this material). The total elongation decreases as the temperature increases from 70 to 600 F. From 600 to 1200 F, the total elongation increases with increasing temperature. It is interesting to note that the tensile strengths and total elongations of the as-received and thermally aged materials are identical at 1200 F.

From these results, it can be concluded that annealing (1 hour at 1832 F) of the unirradiated specimens before testing has essentially no effect on the strength or the ductility of the as-received or thermally aged cladding.

Table 6-1. Tensile Testing of Stainless Steel Cladding

	Test temperature, F											
	70		600		750	900		1050	1200		1300	1450
Fluence	BA	AA	BA	AA	BA	AA	BA	AA	BA	AA	AA	AA
Peak	2	2	2	2	2	2	2	2	2	2	2	0
Minimum	2	2	2	2	0	0	0	0	2	2	0	0
As-received	2	2	2	2	0	0	0	0	2	2	0	0
Aged 3000 h	2	2	2	2	2	2	0	2	2	2	2	2
Aged 6000 h	2	2	2	2	0	0	0	0	2	2	2	0

BA - before annealing
AA after annealing

6.2.4.2. Irradiated Cladding

The results of the tensile tests on the irradiated cladding before and after annealing are shown in Table 6-2. The fluence received by the specimens ranged from about 5×10^{20} to about 2.5×10^{21} (E > 1 MeV). The data shown in Table 6-2 are plotted in Figures 6-27 through 6-42. All the data points on these figures represent the average of the two specimens tested at any one condition.

The tensile properties of the as-irradiated cladding are shown in Figures 6-27 through 6-30. The data shown in Table 6-2 and Figures 6-27 and 6-28 indicate that the yield and ultimate strengths are about equal and that variations in fluence have little or no

effect on the yield and ultimate strengths. The uniform and total elongations are about equal for any given specimen. One would expect, when the yield and ultimate strengths are equal, that the uniform elongation would be essentially zero and all elongation would be nonuniform; however, this was not always the case, as indicated by the data in Table 6-2. The uniform and total elongations for the specimens from the low-fluence regions of the rods were slightly greater than those for the specimens from the high-fluence regions.

The tensile properties of the irradiated cladding after annealing are shown in Figures 6-31 through 6-34. As in the case of the irradiated specimens that were not annealed, the tensile and ultimate strength did not vary with fluence, although there was considerable difference in the yield and ultimate strengths at test temperatures below 1000 F. The uniform elongation in most instances was almost equal to the total elongation, regardless of the test temperature.

The data for the as-irradiated cladding before and after annealing are compared in Figures 6-35 through 6-38. Annealing reduces the tensile and ultimate strength of the material significantly at test temperatures below 800 F. At test temperatures above 800 F, the strength of the as-irradiated cladding is generally lower than that of the irradiated cladding after annealing. Apparently, the annealing operation produces some secondary hardening that does not occur in the as-irradiated cladding. It is also possible that many of the defects introduced by irradiation began to move rapidly during testing at temperatures above 800 F. The movement of defects causes the specimens to rupture at a lower load than that required to rupture specimens in which there is little defect movement.

Annealing for one hour at 1832 F restored some of the ductility to the specimens at test temperatures below 1000 F; the restoration of ductility was far from complete, however. At test temperatures above 1000 F, there was essentially no difference between the elongation of the as-irradiated cladding and that of the irradiated cladding that had been annealed.

The data for the unirradiated and irradiated cladding after annealing are compared in Figures 6-39 through 6-42. There are some minor differences in strength of the unirradiated and

irradiated materials, particularly in the shape of the curves above 800 F. It appears that irradiation may have shifted the initiation of the secondary hardening process to a slightly lower temperature or may have altered the process. Because the unirradiated cladding may not be truly representative of the material irradiated (discussed in section 5.2), it is impossible to determine whether these differences are caused by irradiation or by differences in materials.

The data also indicate that the annealing operation has eliminated essentially all of the strengthening produced by displacement-type defects introduced during irradiation. Even though the strengths are returned to the unirradiated condition, the elongations of the irradiated cladding after annealing are still considerably below those for the unirradiated cladding. This would suggest that some factor other than point defects is the cause of the low elongations.

A series of tests to determine the effect of irradiation at 545 F on the tensile properties of AISI type 304 stainless steel were conducted by Bement.[5] The results of these tests with relation to the elevated-temperature properties of the material are summarized in Figures 6-43 and 6-44. The general trend shown in these figures is similar to those shown in Figures 6-27 and 6-29, except for the following:

1. Significant differences in both strength and elongation were observed with the standard type 304 stainless steel when the fluence varied from 1.5×10^{20} to 6×10^{21}, whereas only minor effects of fluence were observed for the borated material when the fluence varied from about 5×10^{20} to 2.5×10^{21}.

2. The unirradiated type 304 stainless steel did not exhibit secondary hardening, whereas the borated material did exhibit some secondary hardening.

At test temperatures below 900 F, the tensile strength of the irradiated type 304 stainless steel was considerably higher than the strength of the irradiated borated stainless steel. The borated cladding was somewhat more susceptible to irradiation embrittlement than was the standard type 304 material. The uniform elongation of the borated cladding for fluences as low as 6×10^{20} nv was no greater

than that of the standard type 304 stainless steel that received a fluence of 6×10^{21} nv. Thus, it appears that the addition of boron to the type 304 stainless steel reduces both the strength and ductility of the irradiated material.

At all test temperatures, the yield strength of type 304 stainless steel irradiated at temperatures above 750 F is only slightly greater than that of the unirradiated material.[6] Furthermore, type 304 steel irradiated at temperatures above 750 F exhibits considerable ductility at test temperatures below 900 F. At test temperatures above 900 F, the ductility decreases rapidly and is essentially zero % at test temperatures between 1100 and 1300 F. By irradiating at temperatures above 750 F it is reported that the displacement defects are annealed out as rapidly as they are introduced.

It is evident that, with standard type 304 stainless steel, the irradiation temperature is a fairly significant factor in determining the effect of irradiation on the mechanical properties. Irradiation of the borated type 304 stainless steel at about 600 F appears to produce a slightly different effect than with the standard type. Irradiation of the borated type 304 stainless steel has the following effects:

1. It reduces the ductility at temperatures above 900 F; this effect is attributed to helium.

2. It introduces some displacement-type defects and some other product which affects the properties below 900 F. Annealing the borated stainless steel returns its strength to the unirradiated condition but does not affect the ductility significantly. If displacement defects were the only factor affecting the properties at test temperatures below 900 F, then the annealing operation should restore the strength and ductility. It is possible that helium in sufficient quantities not only affects the elevated-temperature ductility, but also affects the ductility both before and after annealing at test temperatures below 900 F.

Because of the high boron-10 content of the cladding, about 280 atom ppm of helium are introduced by irradiation. It appears likely that helium may be the factor affecting the properties of the stainless steel at all test temperatures. No data are available to substantiate this conclusion at test temperatures below 900 F. Work at ORNL indicated that the ductility of austenitic stainless steel at 1300 F

is reduced with increasing helium.[7] Unfortunately, similar data were not obtained for lower test temperatures.

Table 6-2. Results of Tensile Testing of Irradiated Stainless Steel Cladding

Spec.[a]	Rod No.	Fast fluence (E > 1 MeV), nvt × 10^{21}	Test temp, F	Strength, psi		Elongation, %	
				Yield	Ultimate tensile	Uniform	Total
PA1	62A	1.72	70	50,800	82,600	6.15	6.40
PA3	62A	1.75	600	30,000	55,900	6.15	6.20
PA5	105A	1.72	900	26,700	61,800	11.10	11.50
PA6	20A	2.32	900	34,900	67,400	7.40	7.50
PA7	$105D_1$	1.78	1050	33,900	51,400	3.30	3.30
PA9	20A	2.43	1200	23,900	27,000	0.40	0.46
PA10	62A	1.72	1200	23,300	26,400	0.73	1.15
PA11	$105D_1$	1.78	1300	11,900	14,500	0.97	3.97
PB1	20A	2.49	70	--	122,400	1.70	3.80
PB2	105E	1.65	70	124,000	127,000	2.61	3.30
PB3	105E	1.65	600	77,400	80,300	0.50	2.90
PB4	105E	1.65	600	74,400	75,000	0.32	2.40
PB5	61A	2.5	750	44,300	46,800	0.36	0.36
PB6	20A	2.32	750	40,700	42,200	0.08	0.19
PB7	105C	1.79	900	16,500	19,900	1.18	1.30
PB8	62A	1.72	900	16,400	18,500	0.15	0.32
PB9	105E	1.65	1200	36,100	37,100	0.36	0.39
PB10	105A	1.76	1200	--	31,900	--	--
MA1	105B	0.433	70	54,400	85,700	10.50	10.51
MA2	20A	0.703	70	45,800	77,300	10.50	10.51
MA3	105E	0.935	600	41,700	65,100	8.25	8.40
MA4	$105P_1$	1.08	600	30,400	64,100	8.75	8.80
MA9	105B	0.655	1200	19,500	28,700	0.33	0.70
MA10	105F	0.575	1200	--	28,900	0.06	0.06
MB1	20A	1.88	70	127,500	128,600	2.45	3.05
MB2	105C	0.97	70	117,500	120,500	4.70	5.40
MB7	$105D_2$	0.895	600	78,800	86,800	2.30	4.80
MB8	$105D_2$	1.79	600	75,500	77,800	2.80	3.95
MB5	$105D_1$	1.64	1200	24,000	30,200	1.64	1.74
MB6	105F	0.92	1200	22,800	27,900	1.10	1.93

(a) P: peak exposure
A: after annealing
B: not annealed
M: minimum exposure

Figure 6-1. Microstructure of Irradiated Cladding

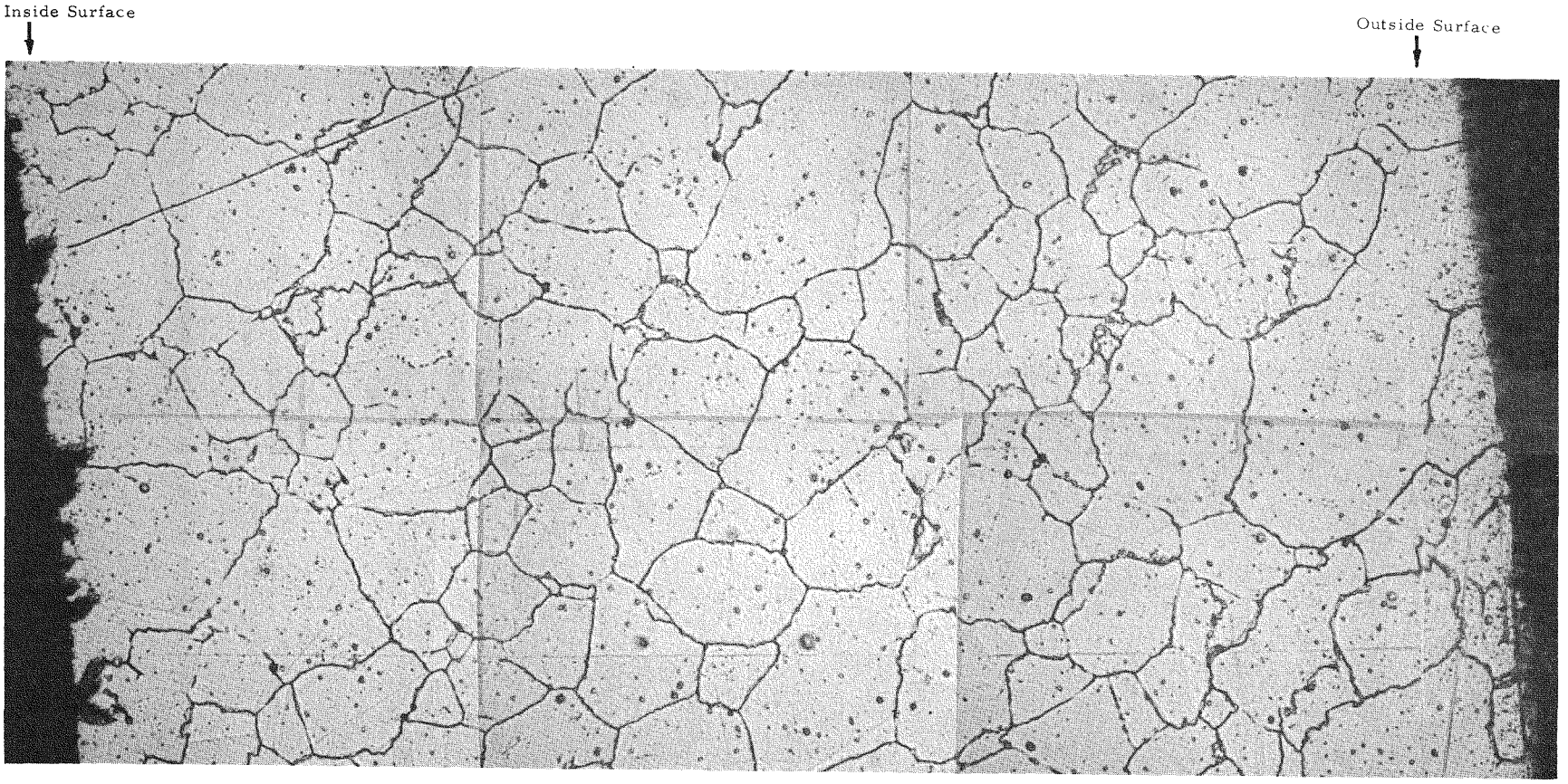

Figure 6-2. Porosity in Irradiated Stainless Steel Cladding (As-Polished, 250×)

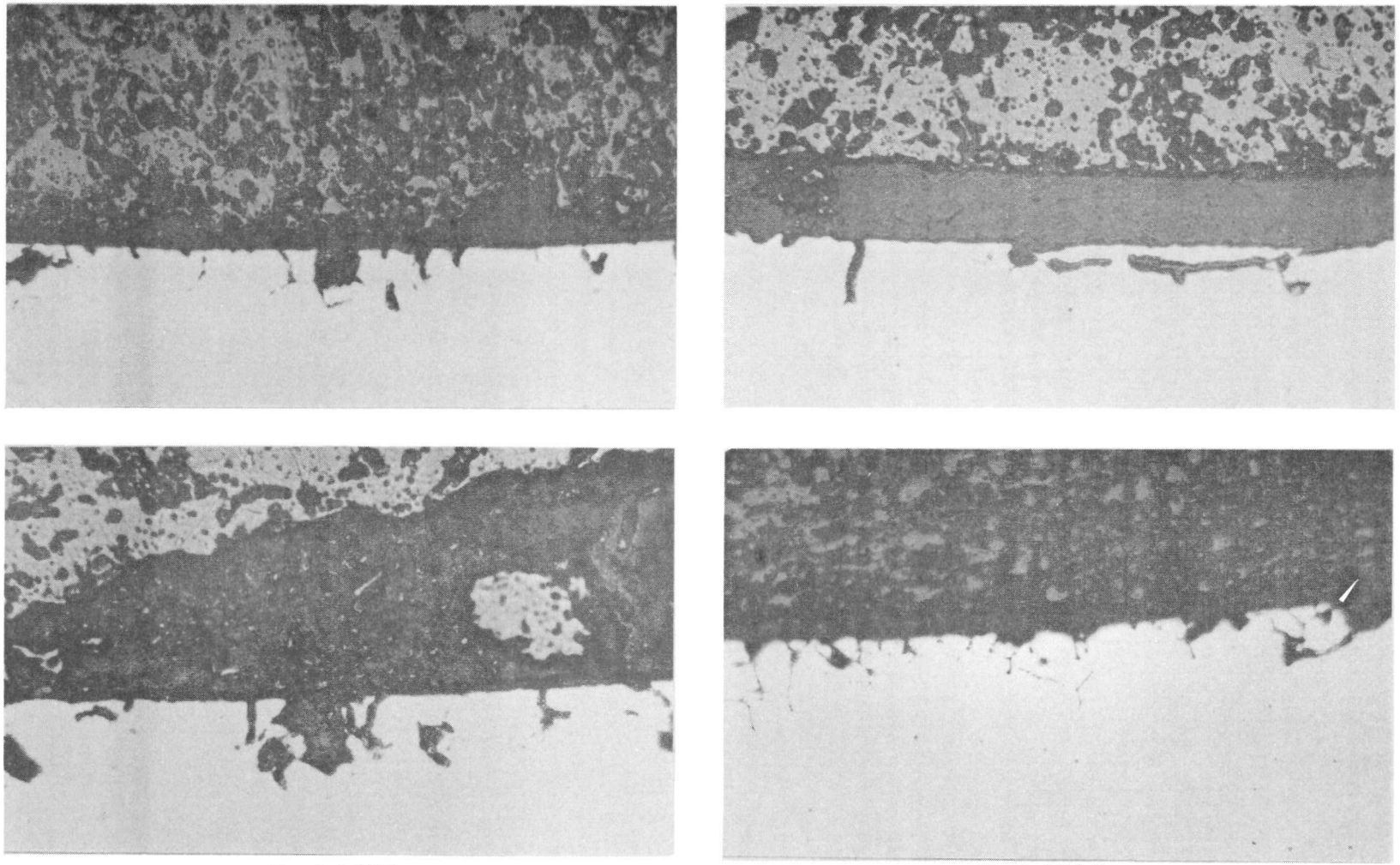

Rod 105B
(Peak Rod Burnup: 30 GWd/T)

Rod 105C
(Peak Rod Burnup: 15 GWd/T)

Figure 6-3. As-Polished and Etched Appearance of Cladding From Rod 105C

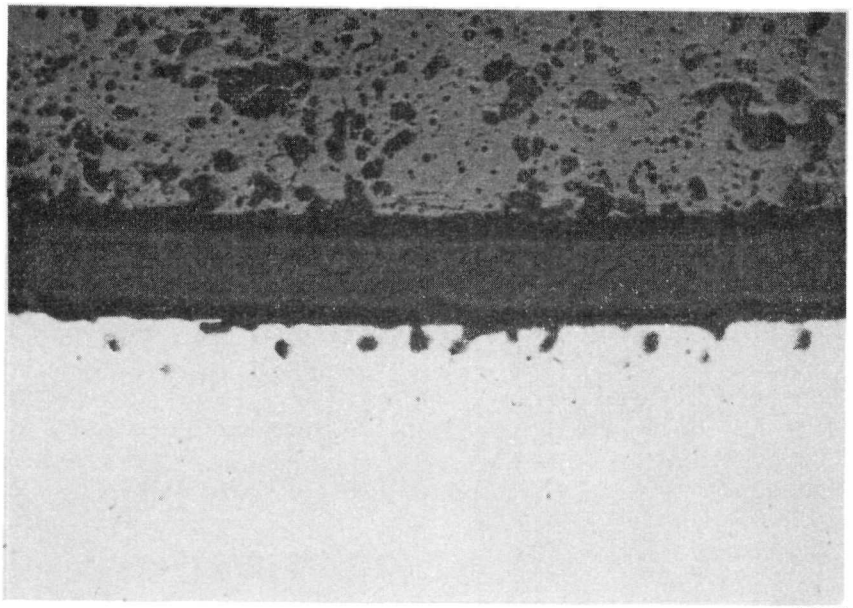

As-Polished 250X

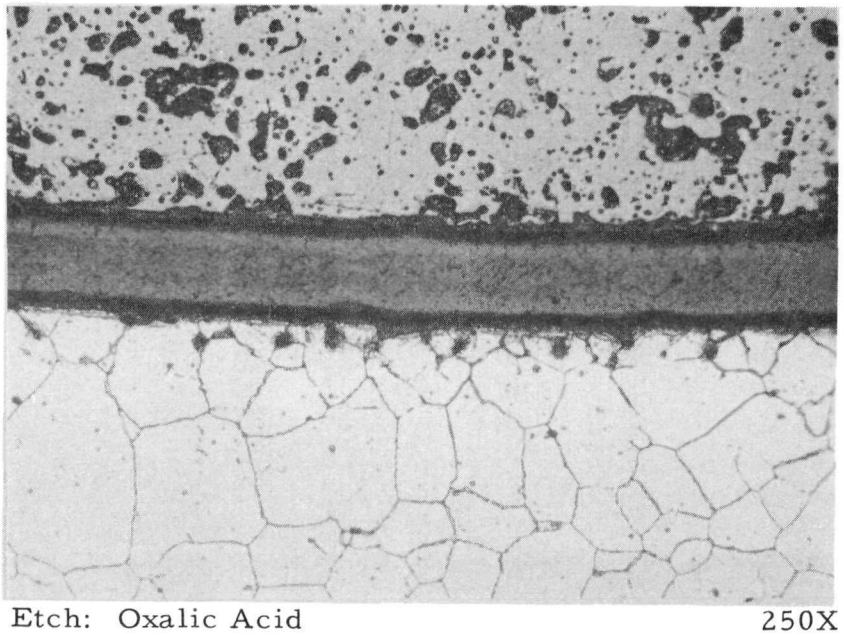

Etch: Oxalic Acid
Electrolytic 250X

Figure 6-4. As-Polished Appearance of Cladding From Rod 105F

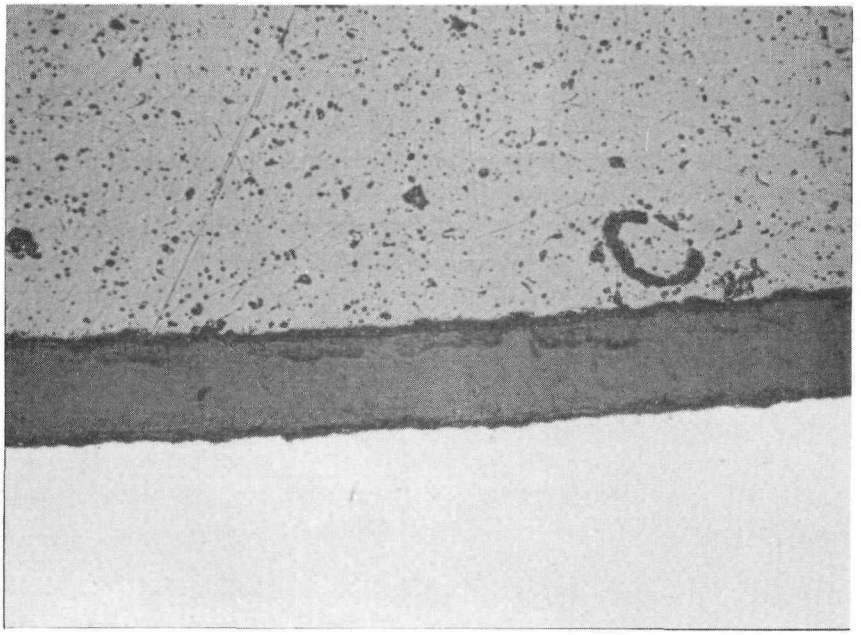

250X

Figure 6-5. Comparison of Inside Surfaces of Cladding in Fuel Rods 106A and 61A

Rod 106A

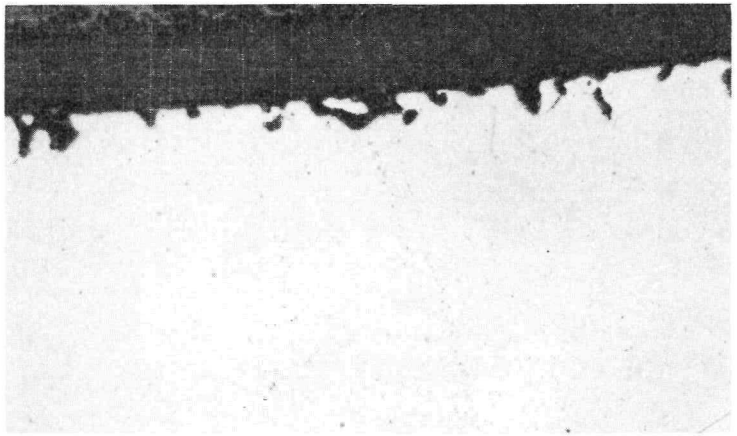

As Polished 250×

Rod 61A

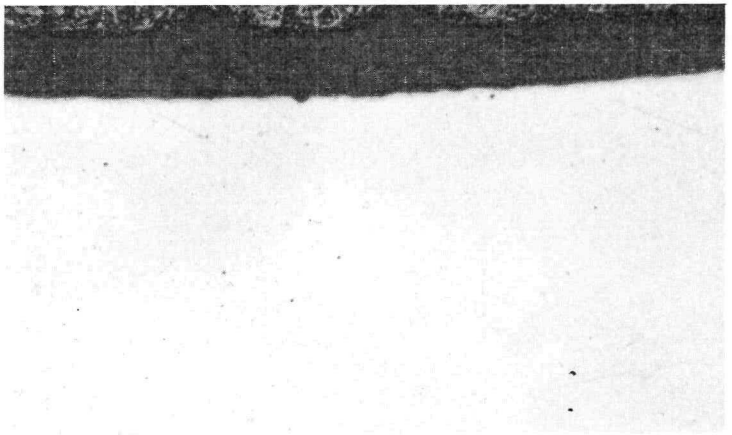

As Polished 250×

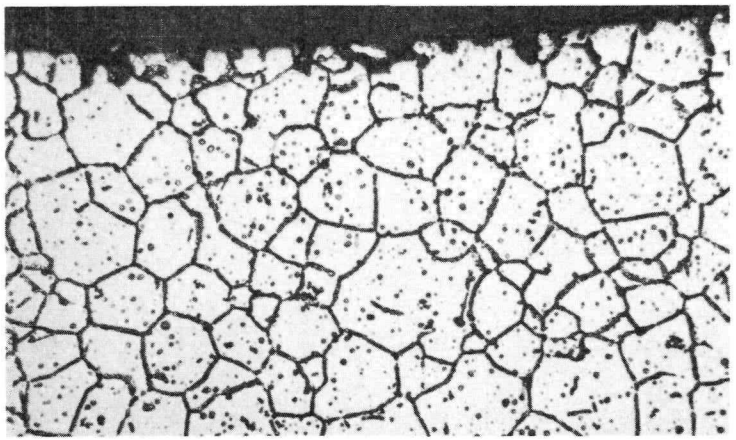

Etched

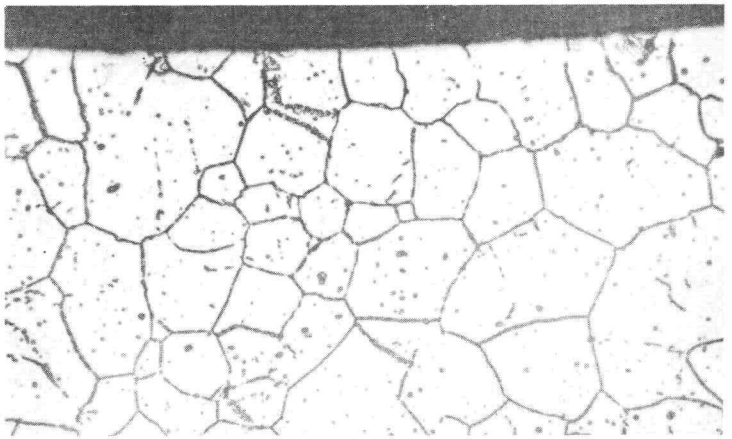

Etched 250×

Figure 6-6. As-Polished and Etched Appearance of Unirradiated Cladding

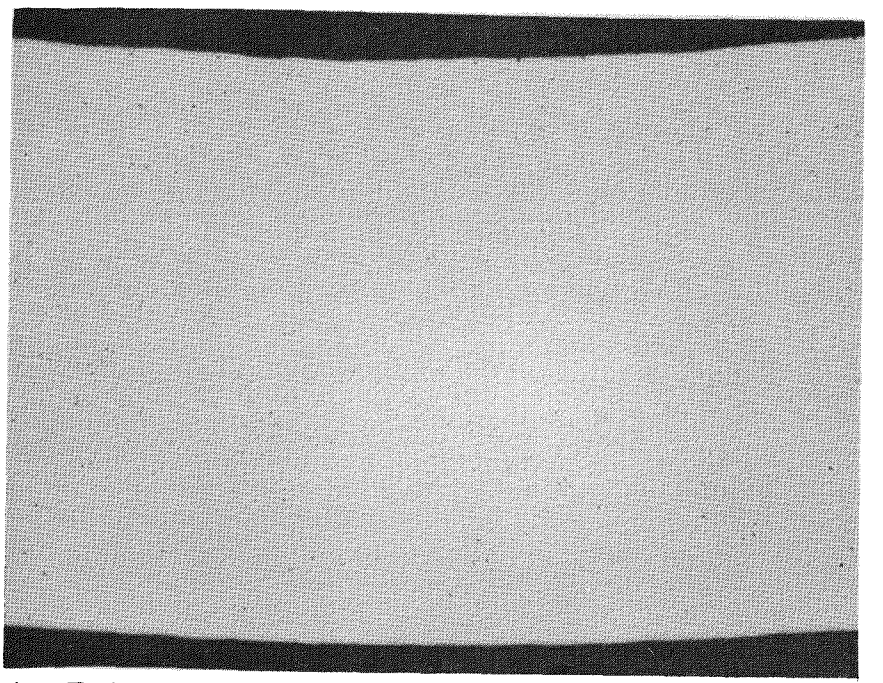

As-Polished 150X

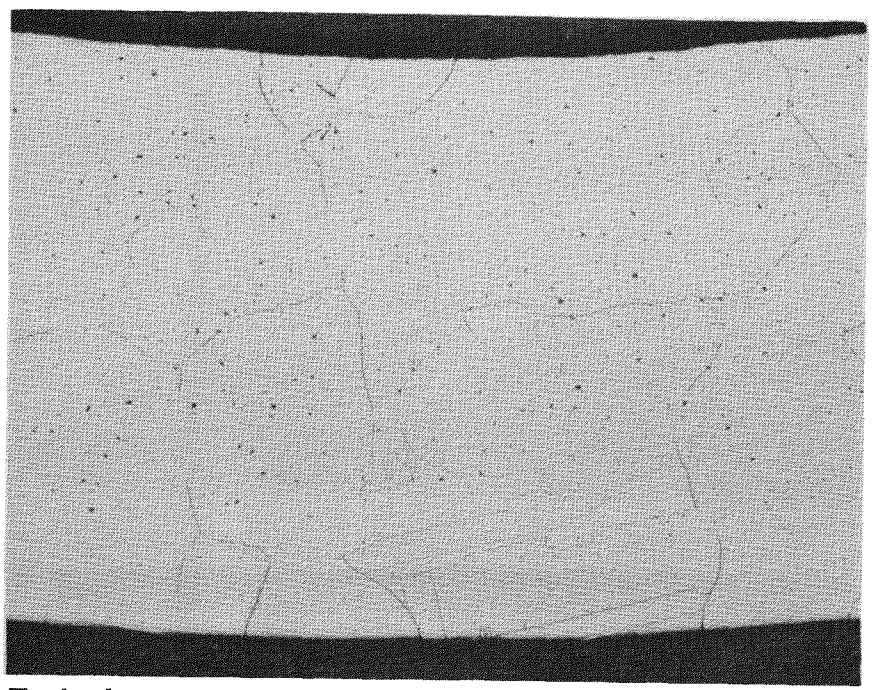

Etched 150X

Figure 6-7. Ferrule From Fuel Rod 106A

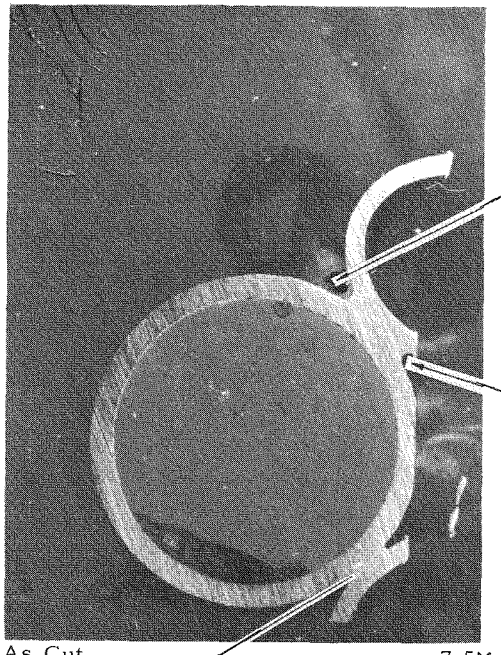

As Cut 7.5×

Photomosiac of this area shown in Figure 6-8

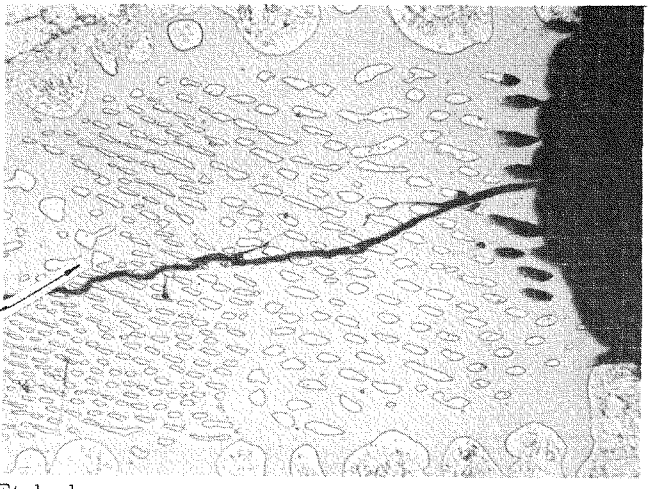

Etched 250×

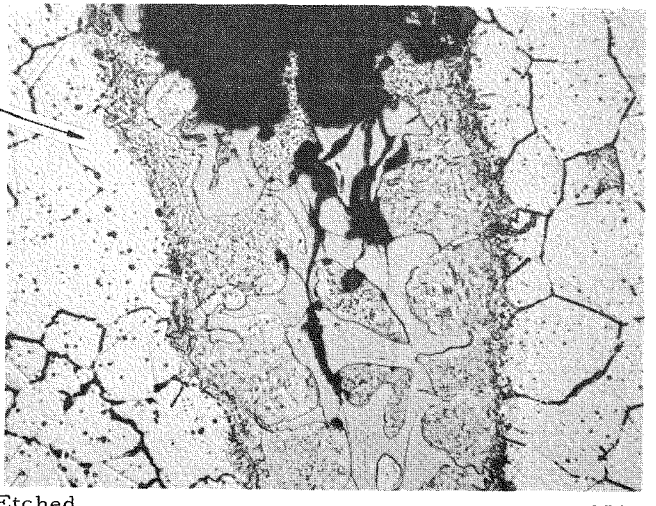

Etched 250×

Figure 6-8. Cladding-to-Ferrule Kannigen Braze Joint

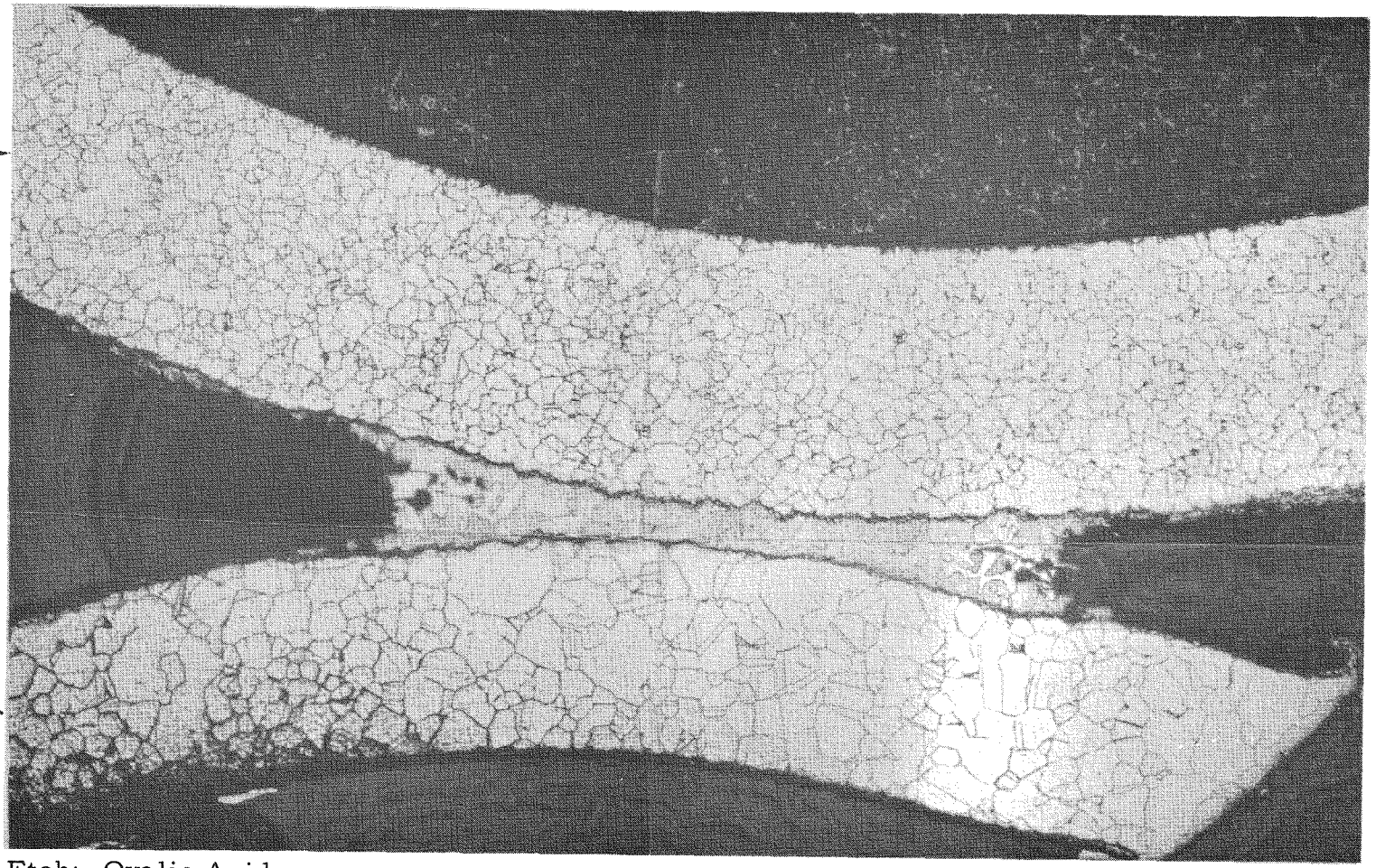

Etch: Oxalic Acid
Electrolytic

75X

Figure 6-9. Unirradiated Braze Joint

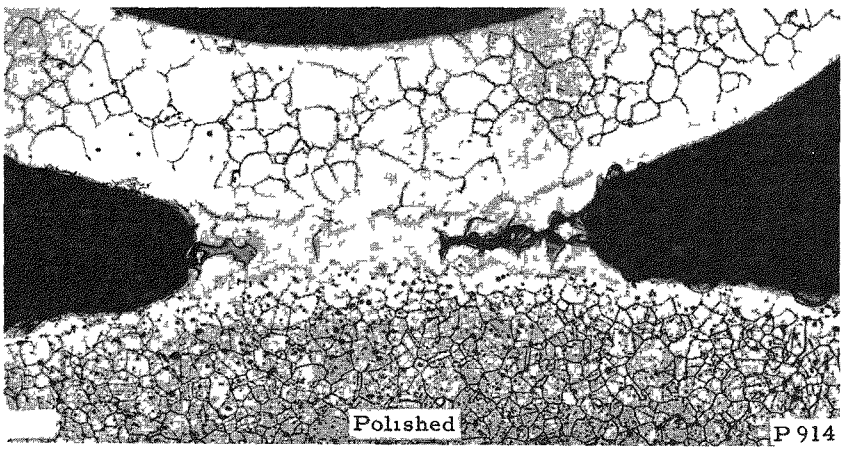

Figure 6-10. Spacer From Fuel Rod 20A, About 35.5 Inches From Bottom of the Rod

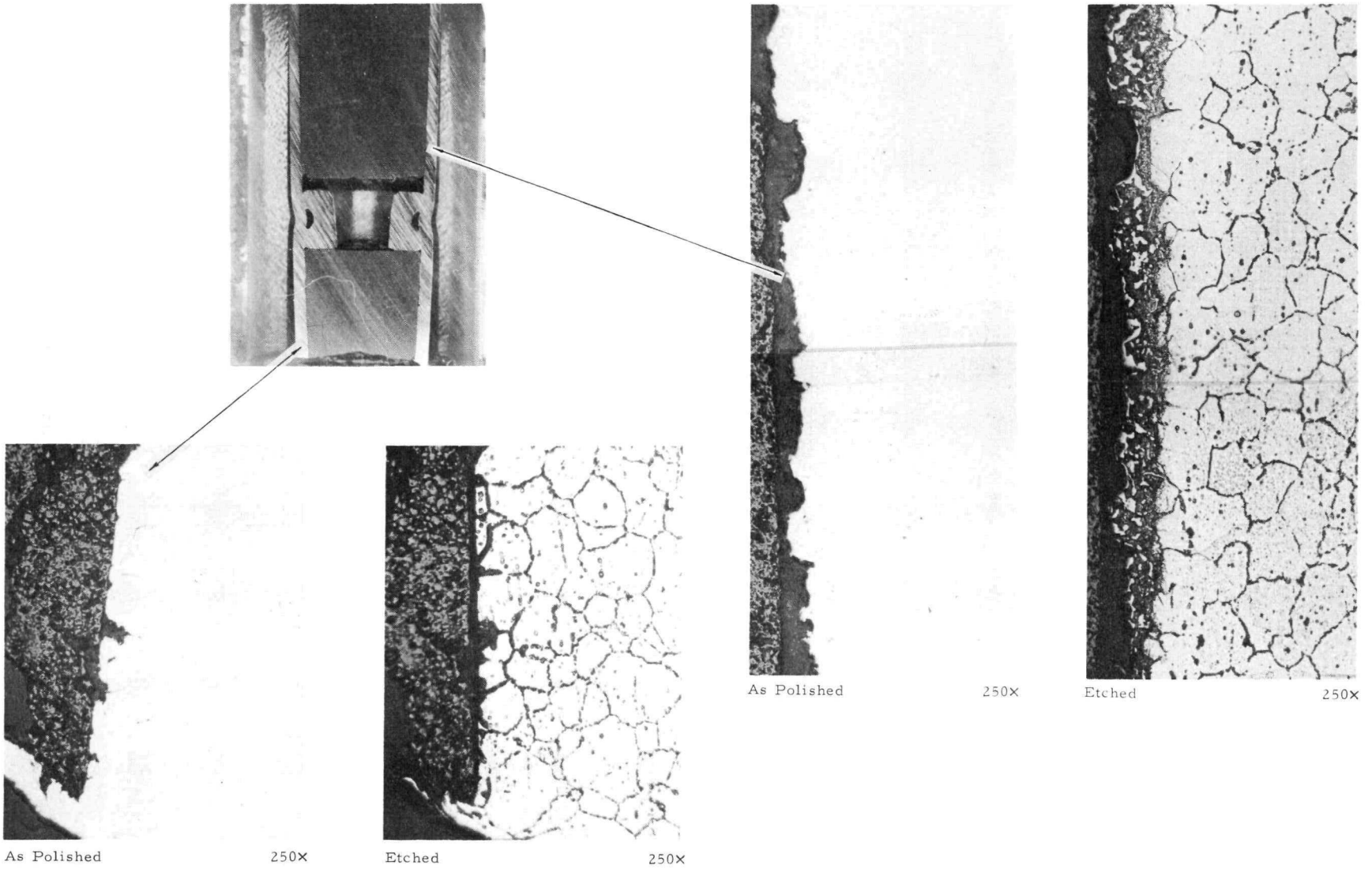

Figure 6-11. Photomosaic of a Portion of the Spacer Shown in Figure 6-10

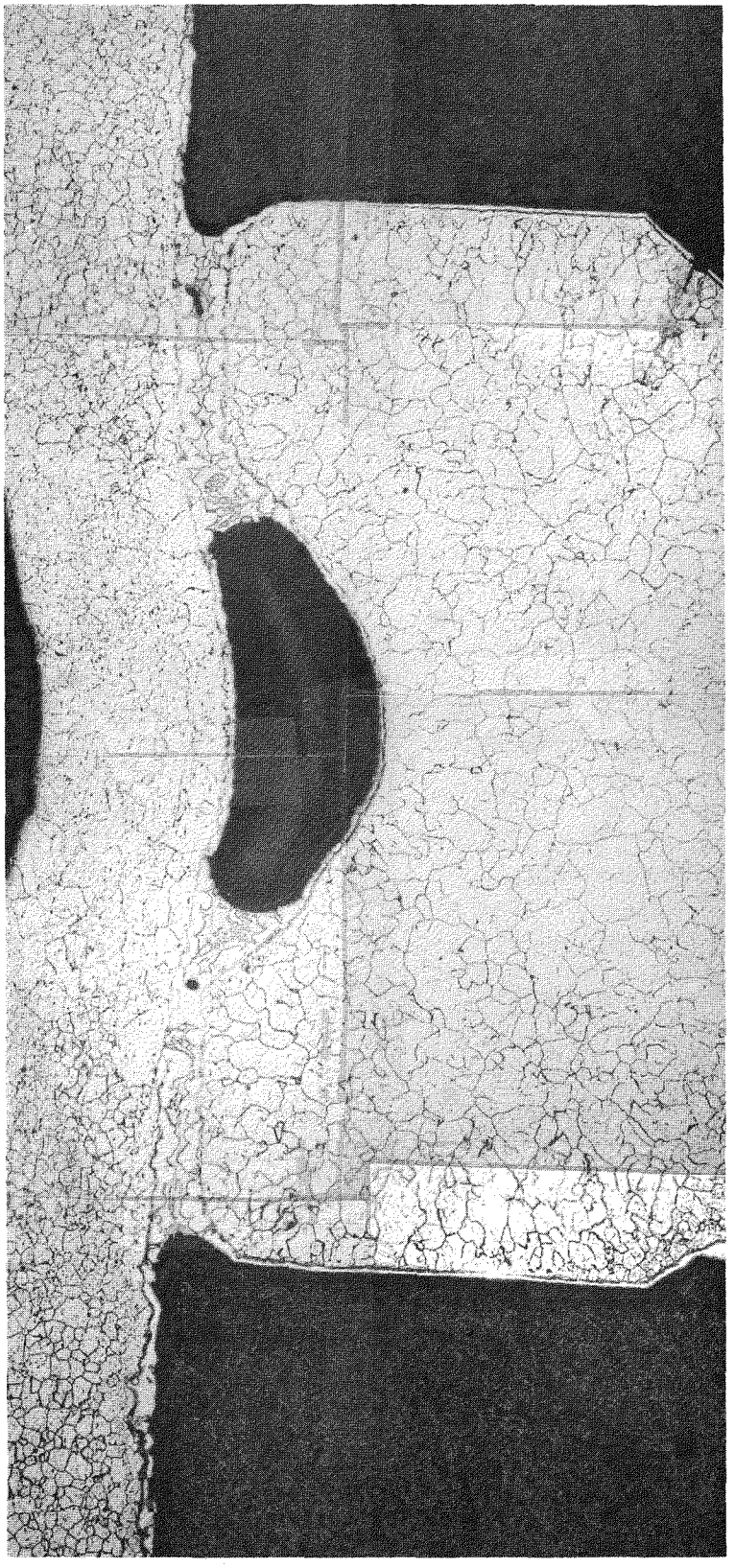

Etched 75X

Figure 6-12. Tensile Specimen for Stainless Steel Cladding

Split Tubular Specimen

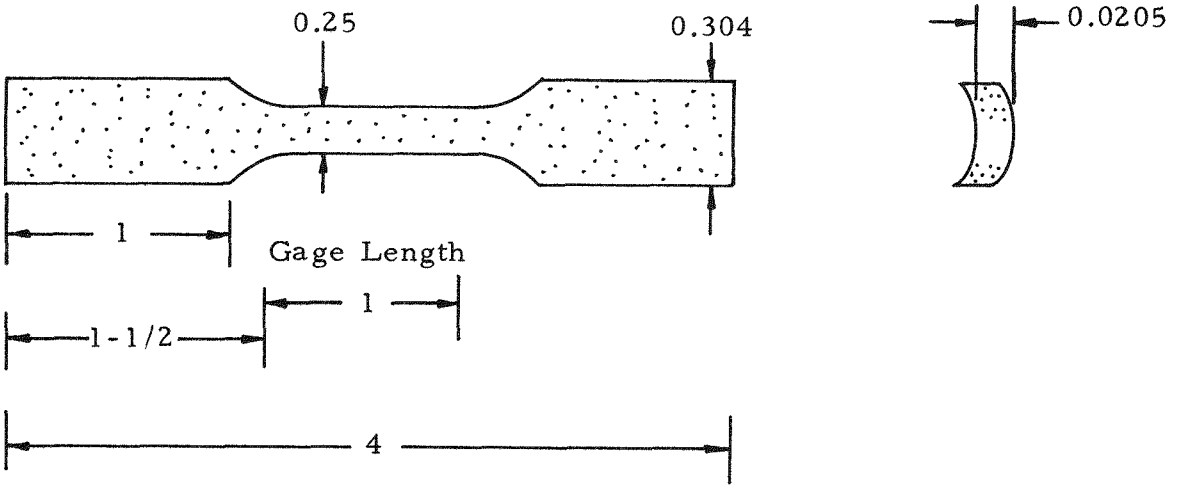

Dimensions in Inches

Figure 6-13. Tensile Grips for Stainless Steel Cladding

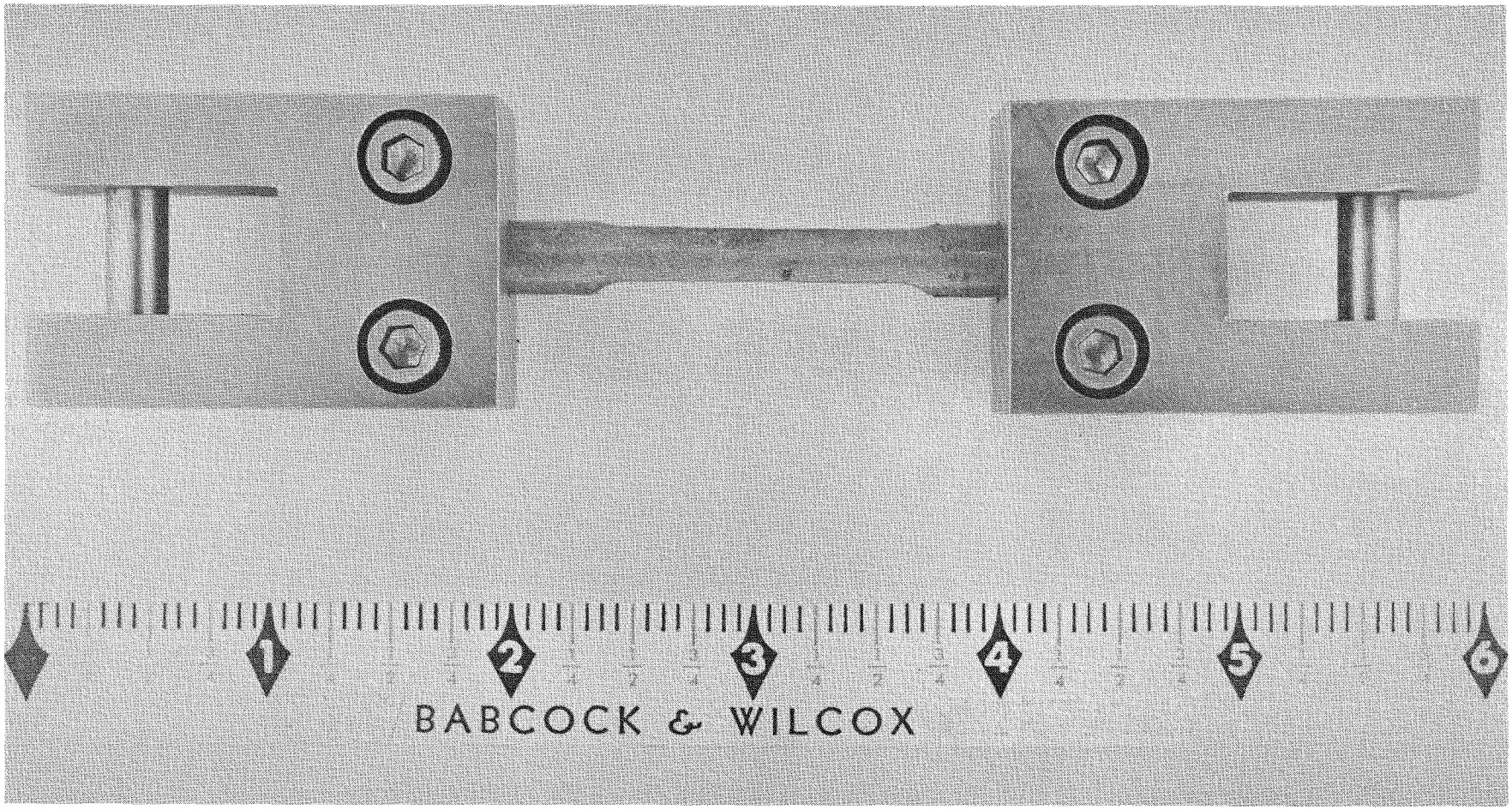

Figure 6-14. Extensometer Used in the Tensile Testing of Stainless Steel Cladding

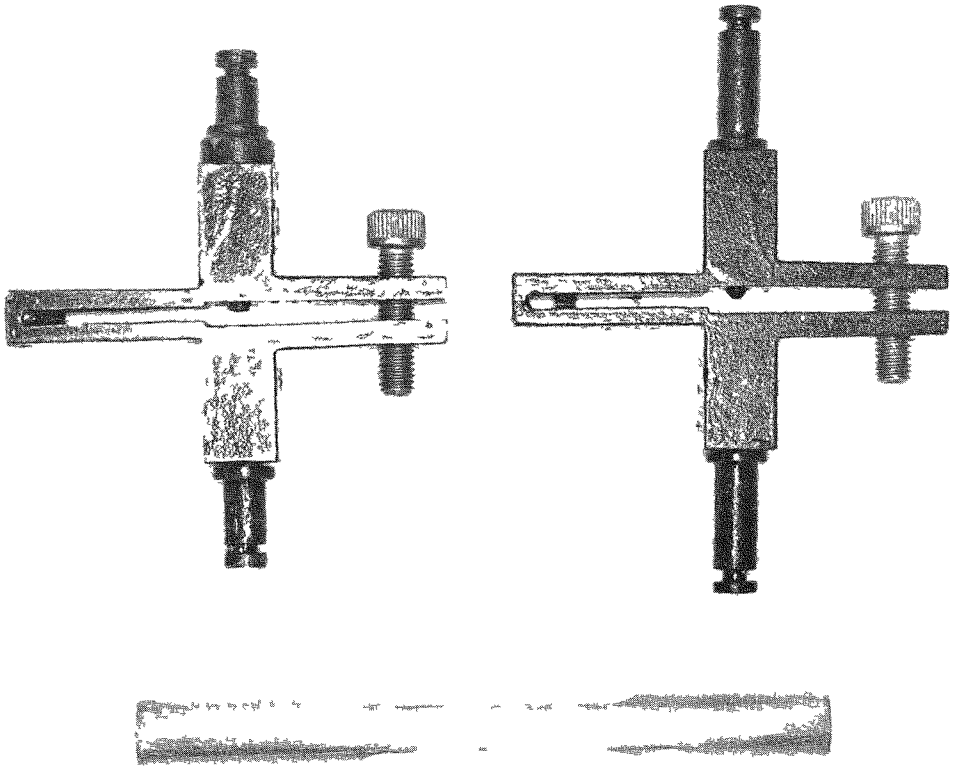

Figure 6-15. Typical Load Deflection Curves for Unirradiated Stainless Steel at Three Test Temperatures

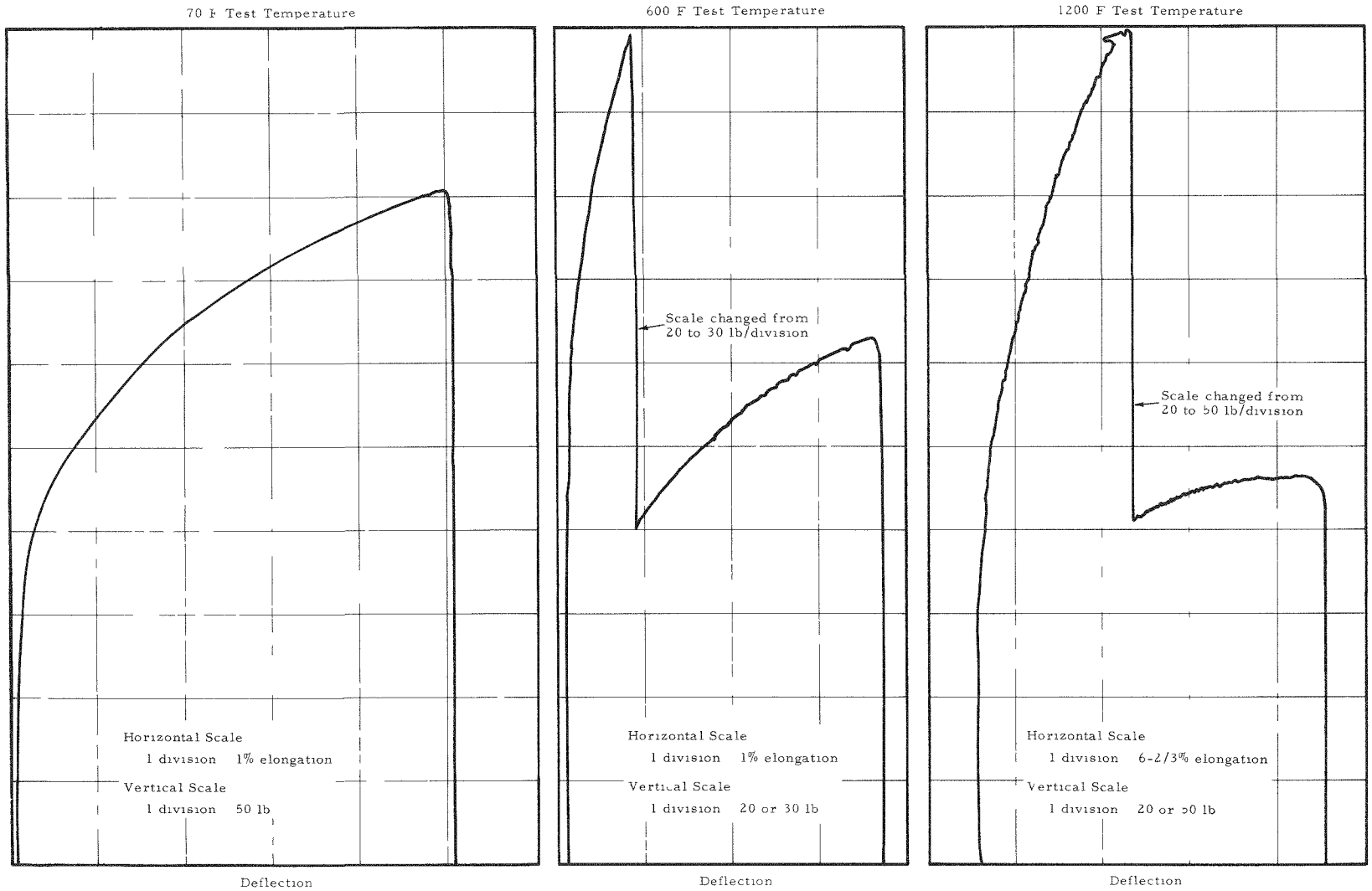

Figure 6-16. Load Deflection Curves for Irradiated Stainless Steel at Three Test Temperatures

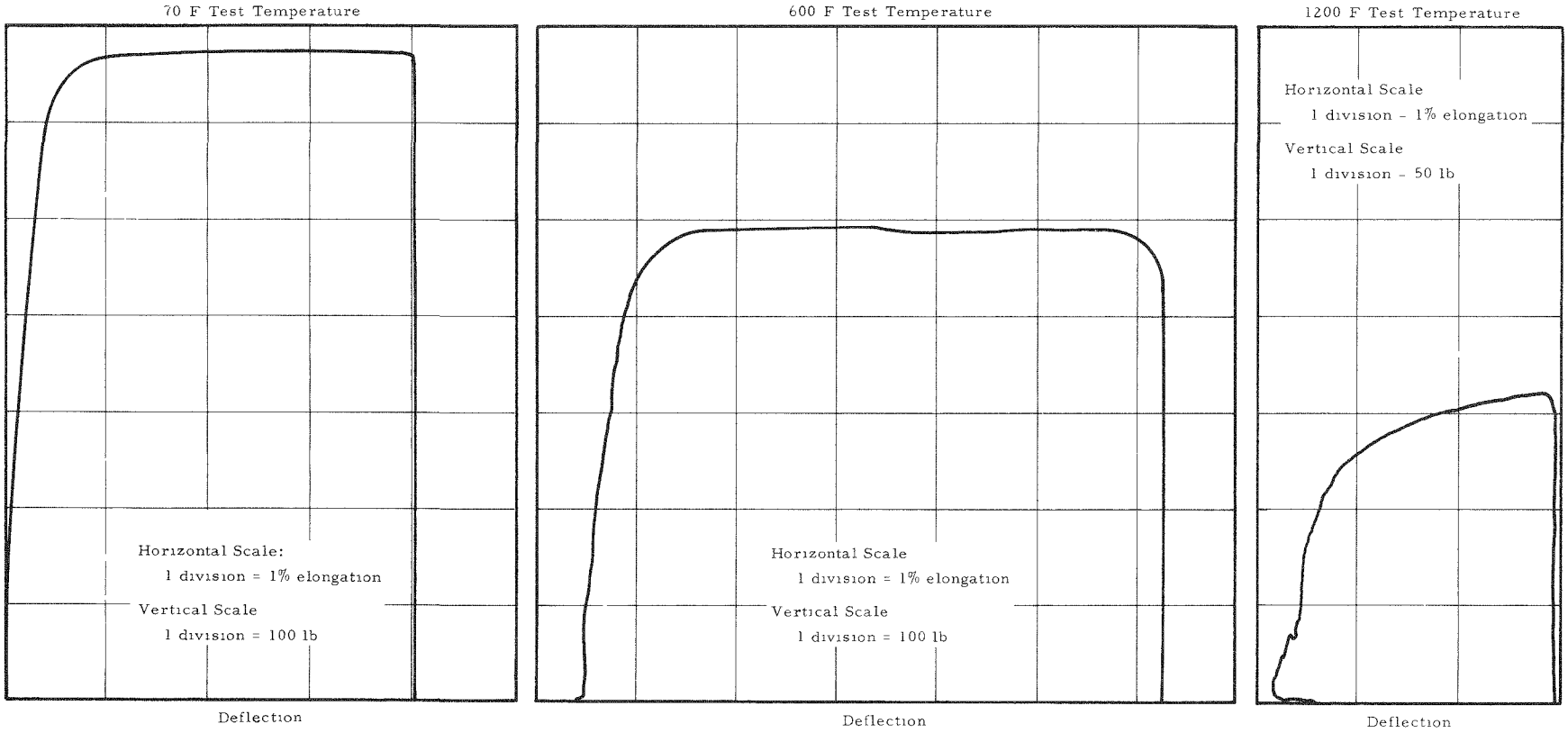

Figure 6-17. Appearance of Tensile Specimens PB-1 and PA-6 After Testing

Specimen PB-1
70 F Test Temperature
Before Annealing

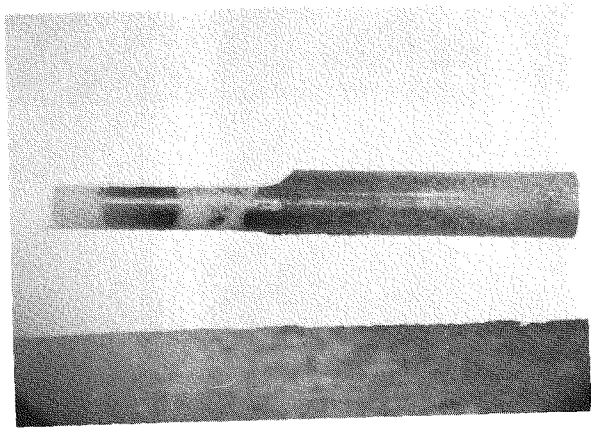

~1×

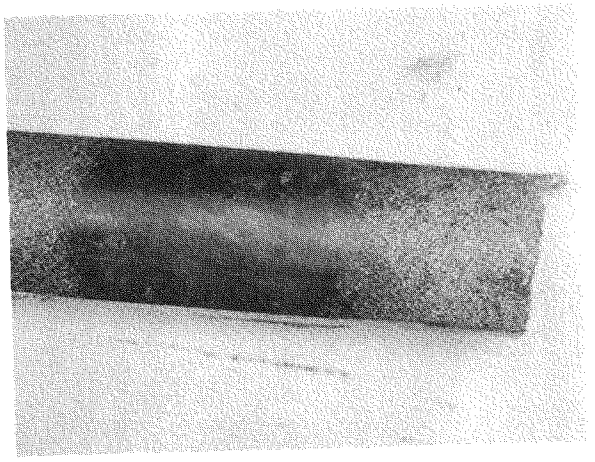

~7×

Specimen PA-6
900 F Test Temperature
After Annealing

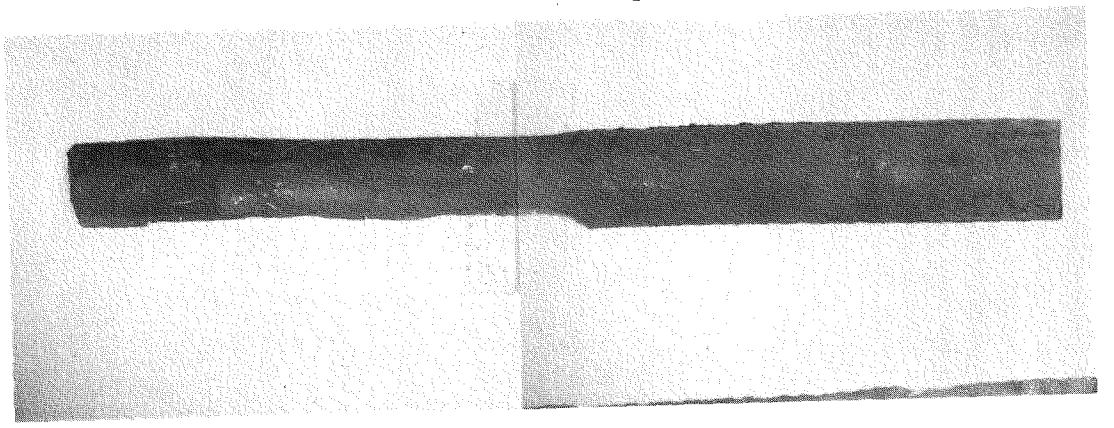

~2.5×

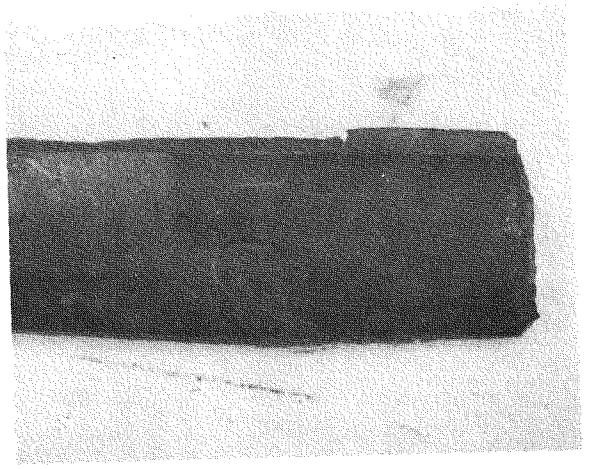

~7×

Figure 6-18. Appearance of Tensile Specimens PB-9 and PA-10 After Testing at 1200 F

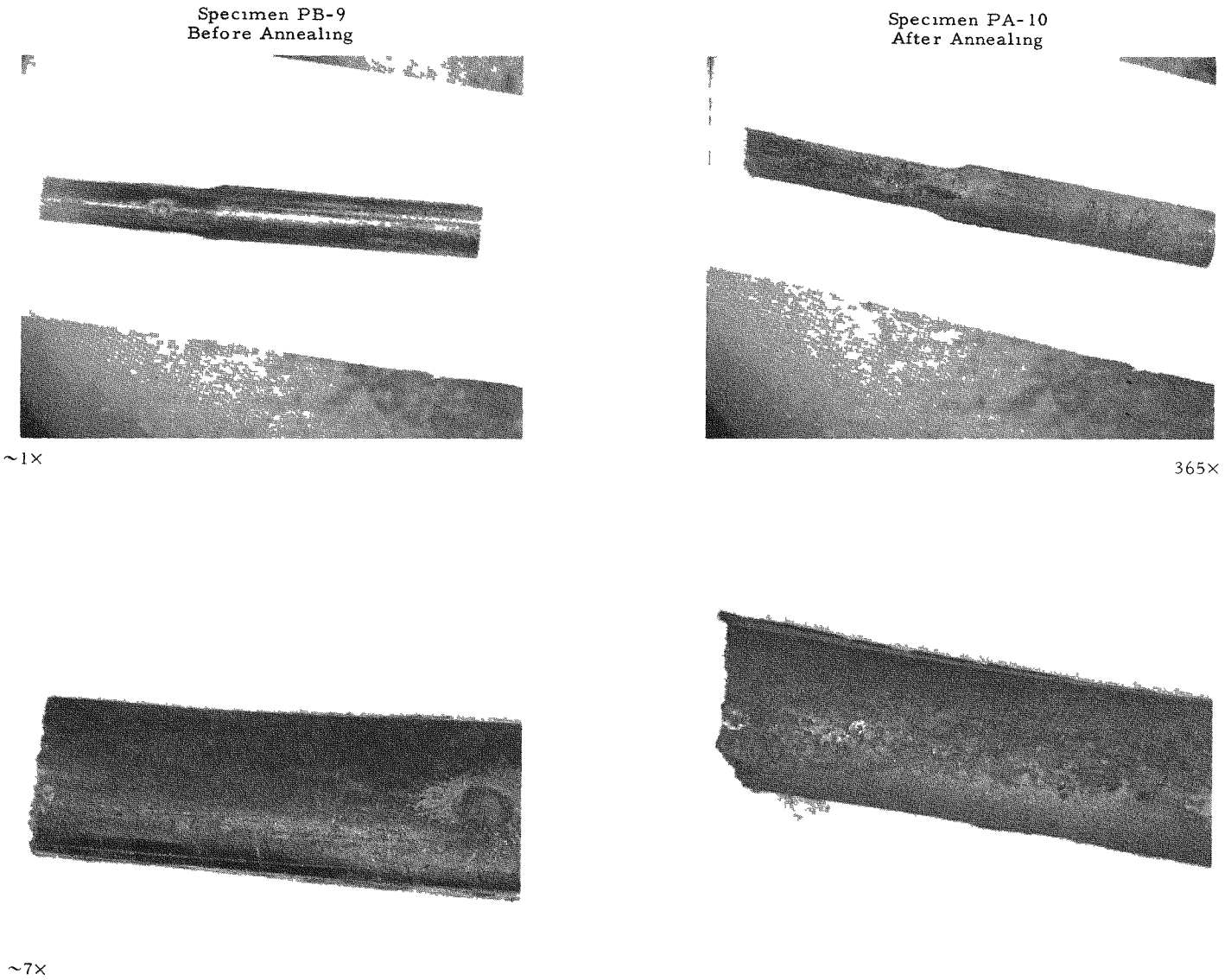

Figure 6-19. Tensile Tests of Unirradiated Stainless Steel Cladding — Yield Strength After Annealing for 1 Hour at 1832 F

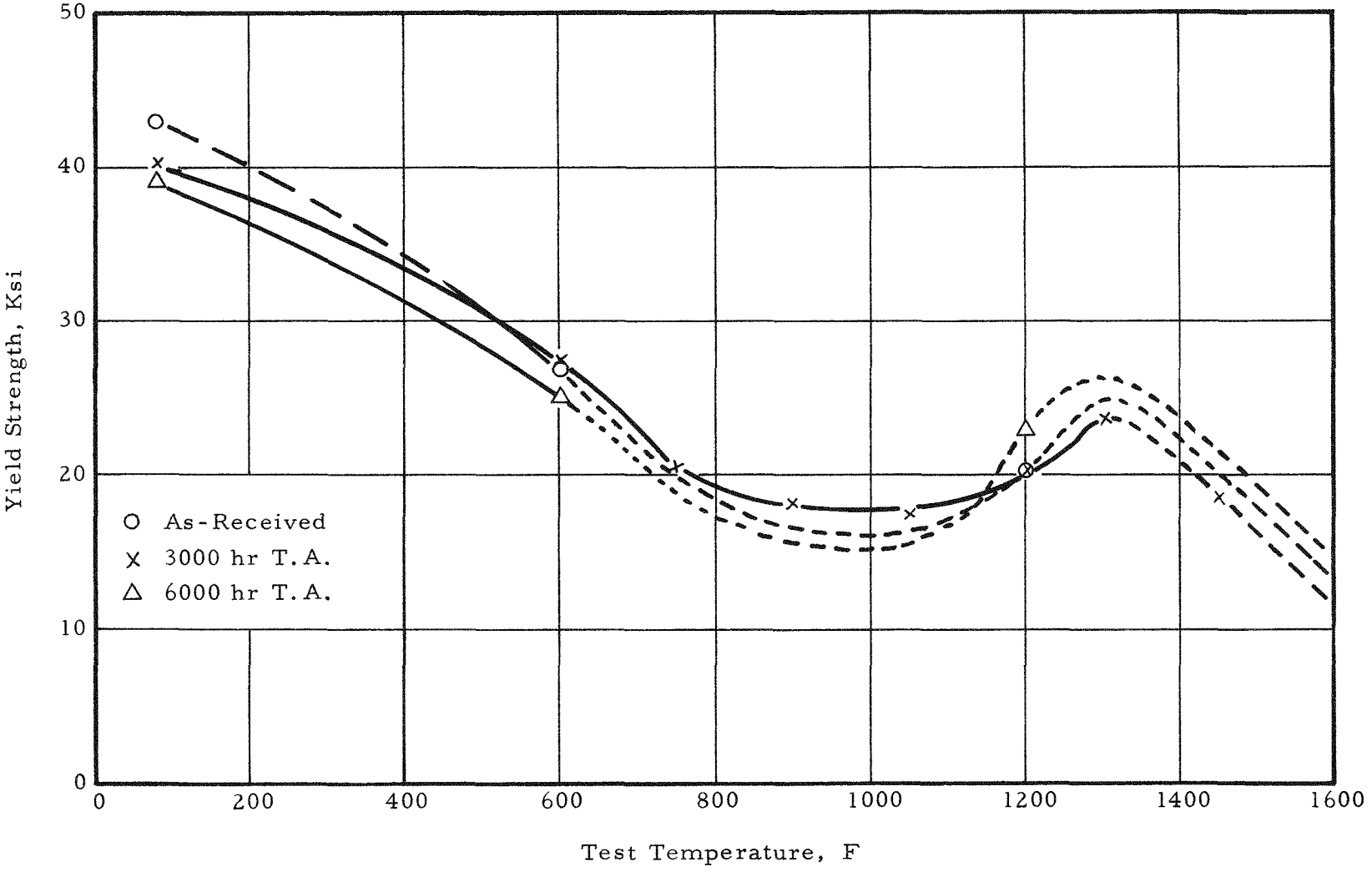

Figure 6-20. Tensile Tests of Unirradiated Stainless Steel Cladding — Tensile Strength After Annealing for 1 Hour at 1832 F

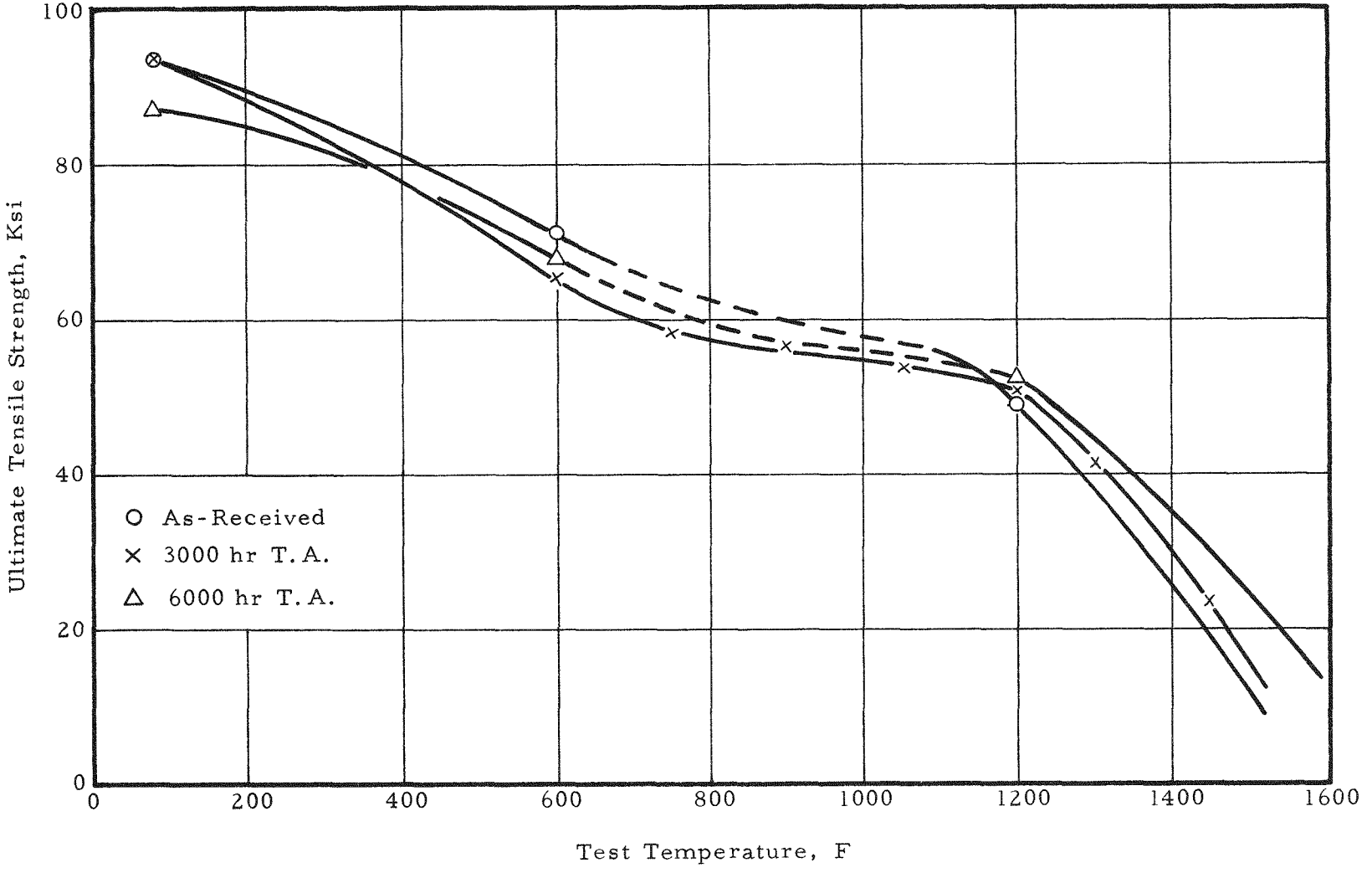

Figure 6-21. Tensile Tests of Unirradiated Stainless Steel Cladding — Uniform Elongation After Annealing for 1 Hour at 1832 F

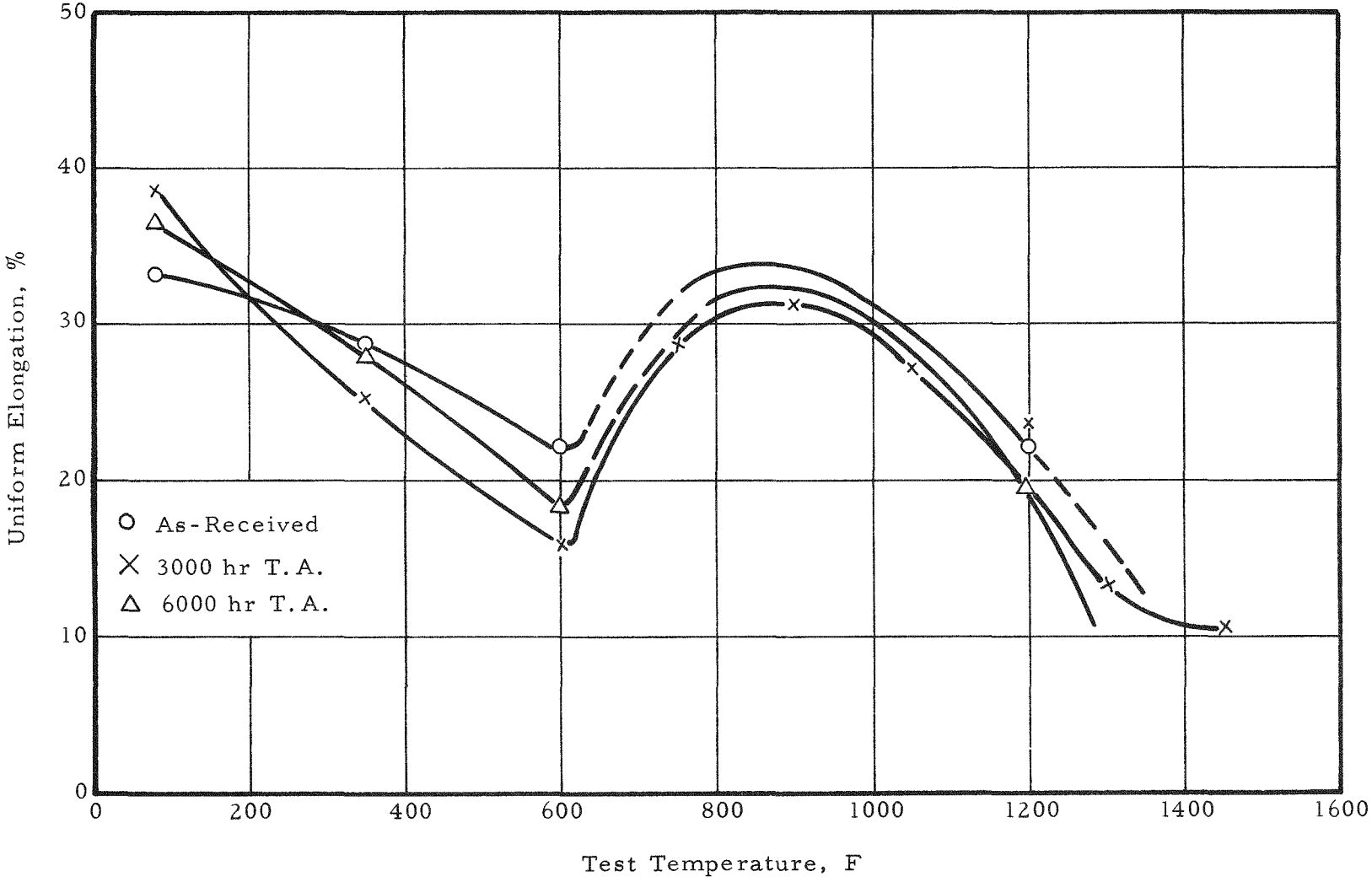

Figure 6-22. Tensile Tests of Unirradiated Stainless Steel Cladding — Total Elongation After Annealing for 1 Hour at 1832 F

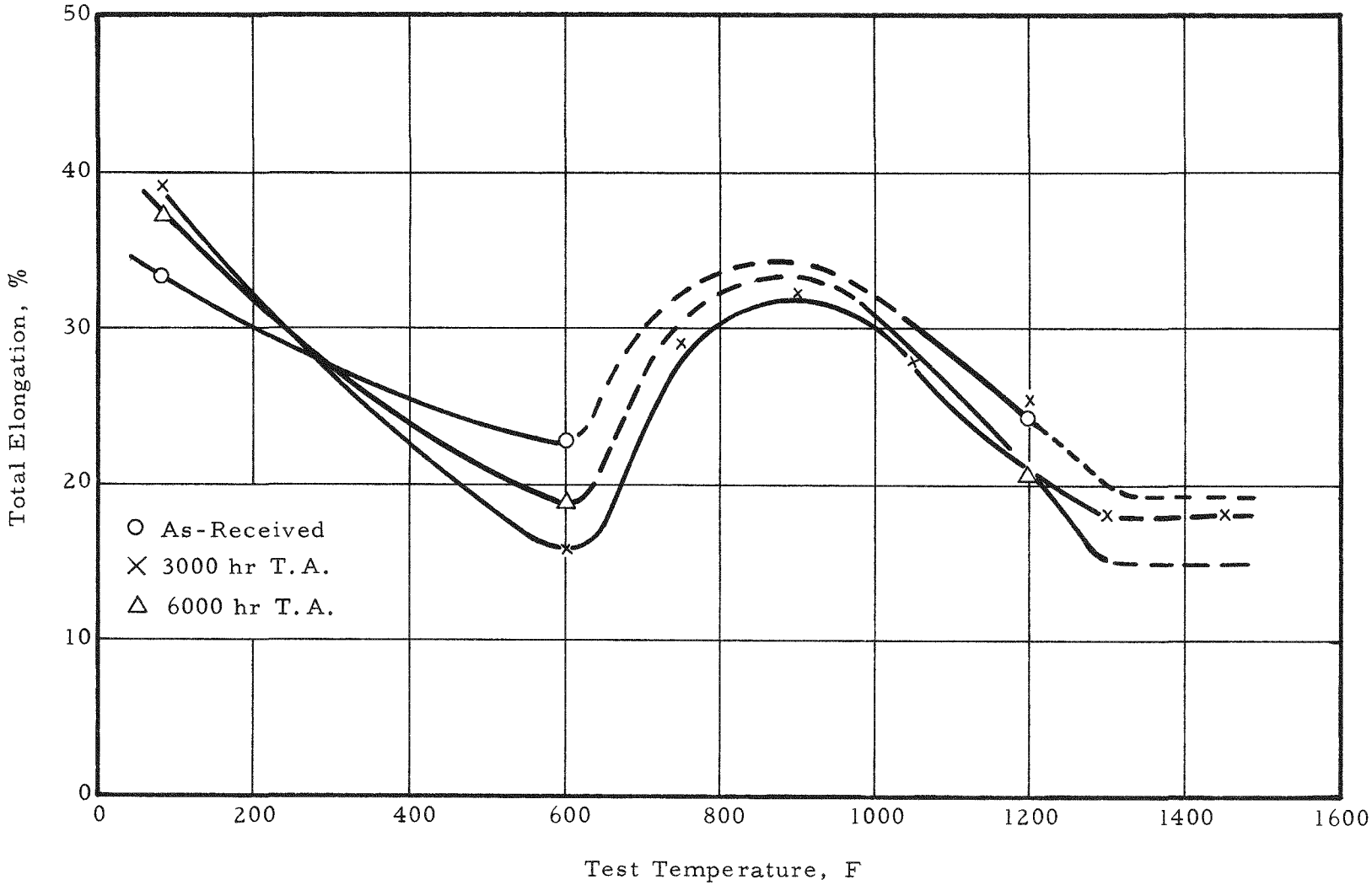

Figure 6-23. Tensile Tests of Unirradiated Stainless Steel Cladding — Yield Strength Before Annealing

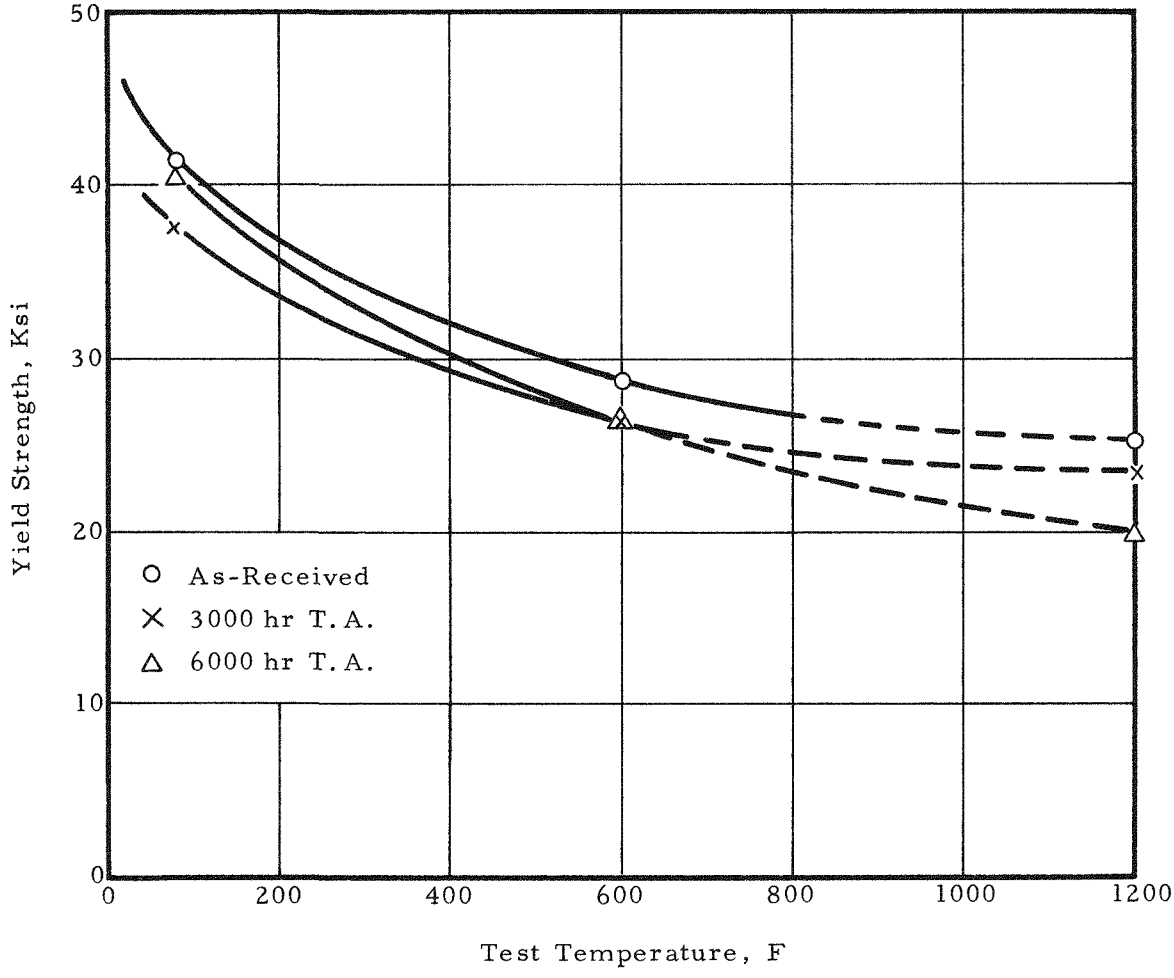

Figure 6-24. Tensile Tests of Unirradiated Stainless Steel Cladding — Tensile Strength Before Annealing

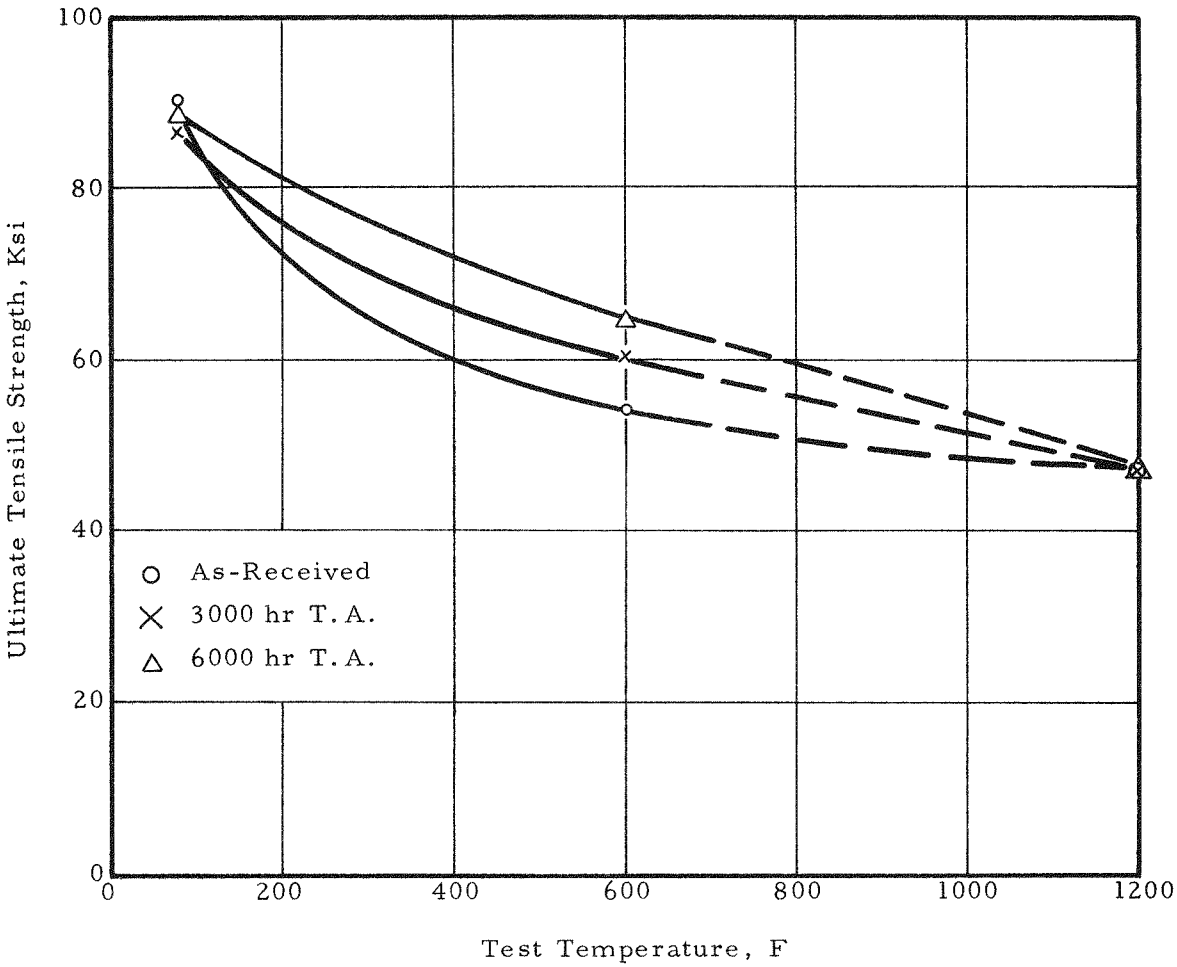

Figure 6-25. Tensile Tests of Unirradiated Stainless Steel Cladding — Uniform Elongation Before Annealing

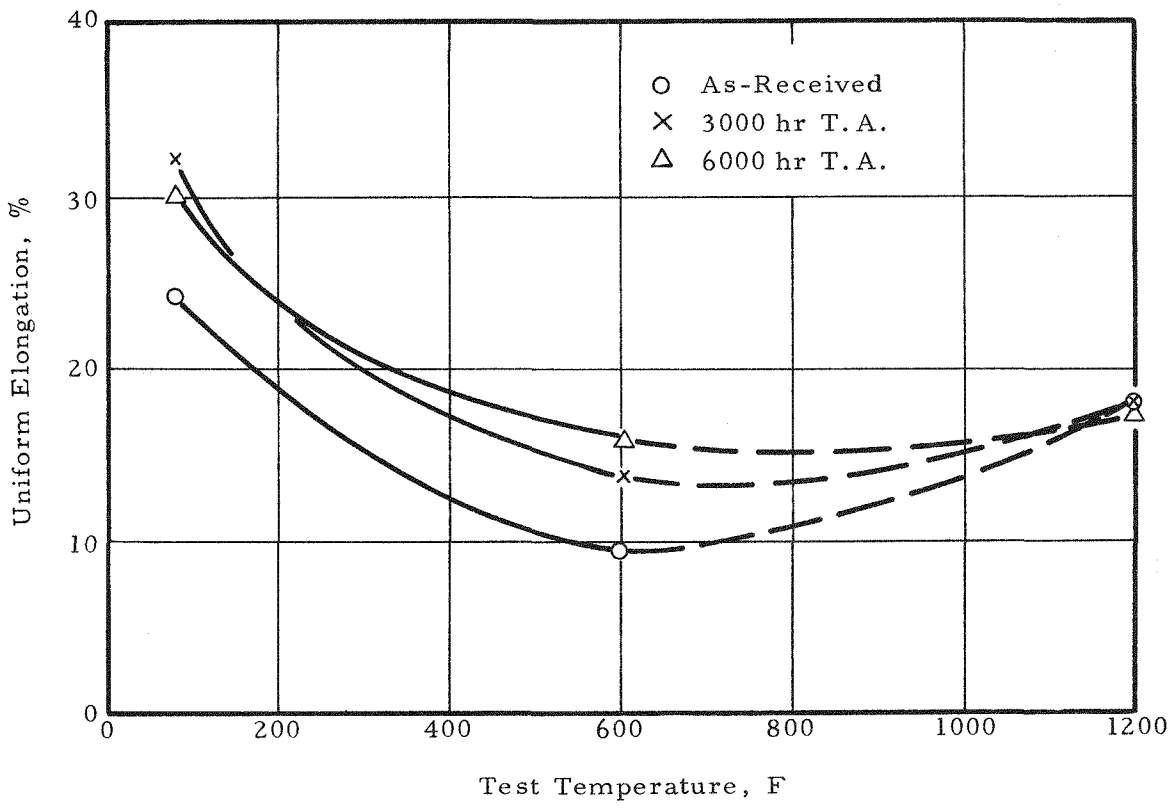

Figure 6-26. Tensile Tests of Unirradiated Stainless Steel Cladding — Total Elongation Before Annealing

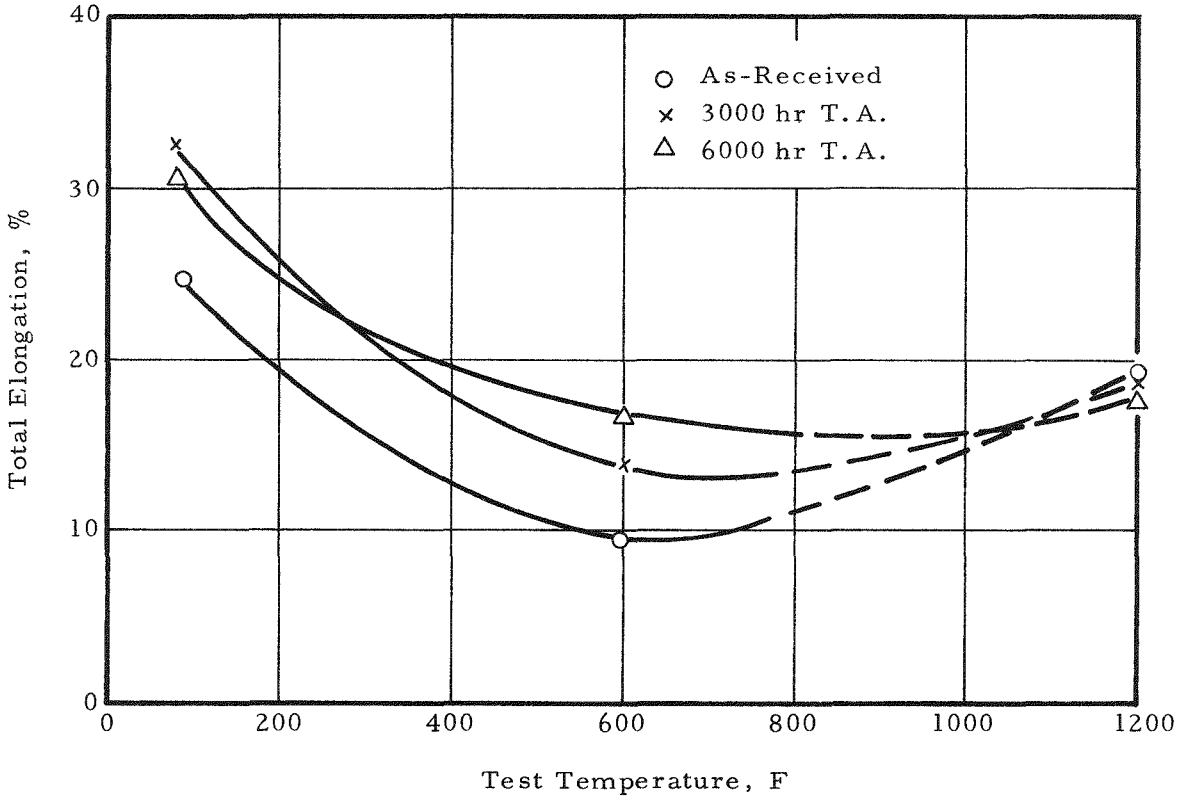

Figure 6-27. Yield Strength of Irradiated Stainless Steel Cladding Before Annealing

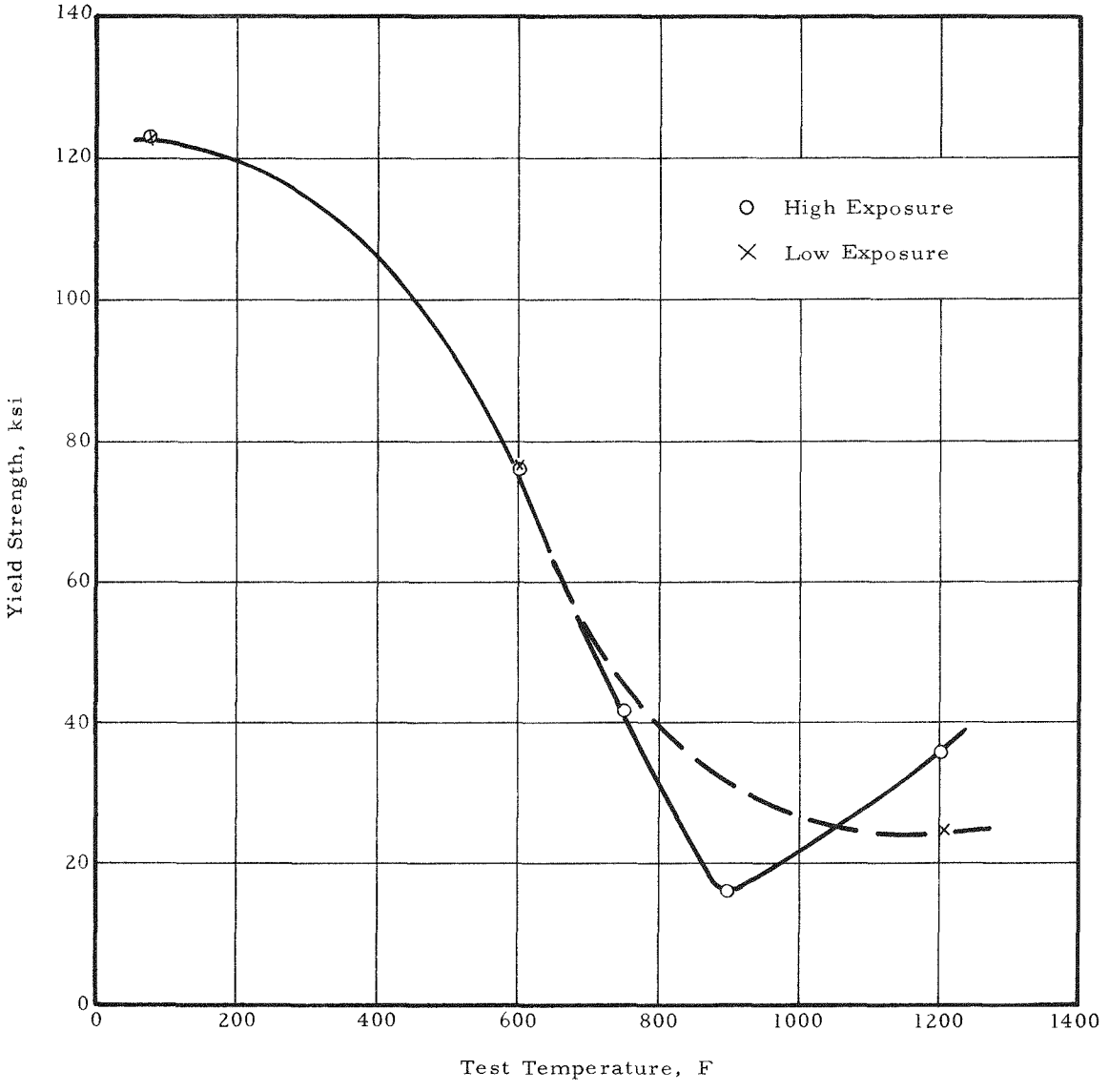

Figure 6-28. Ultimate Strength of Irradiated Stainless Steel Cladding Before Annealing

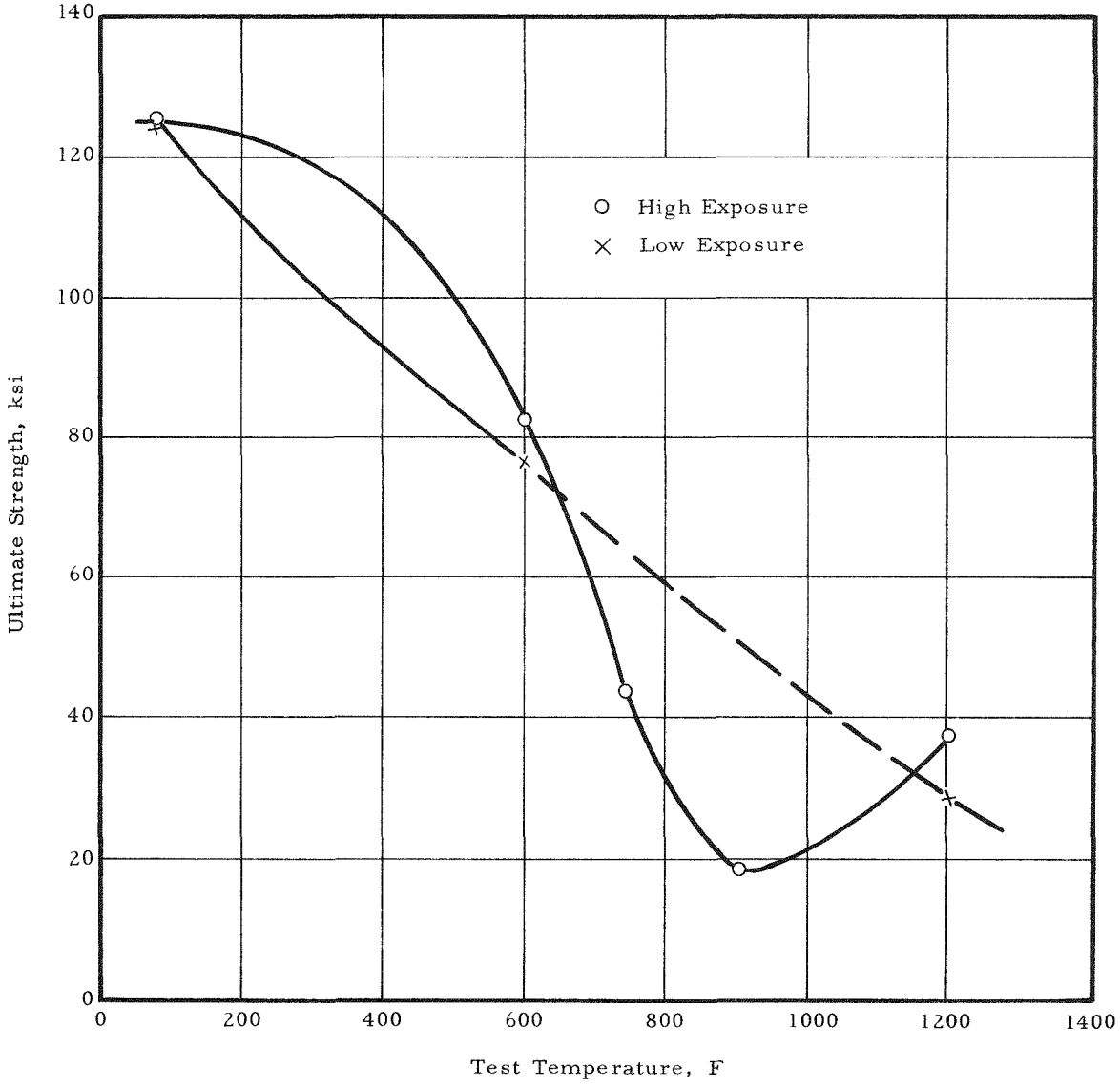

Figure 6-29. Uniform Elongation of Irradiated Stainless Steel Cladding Before Annealing

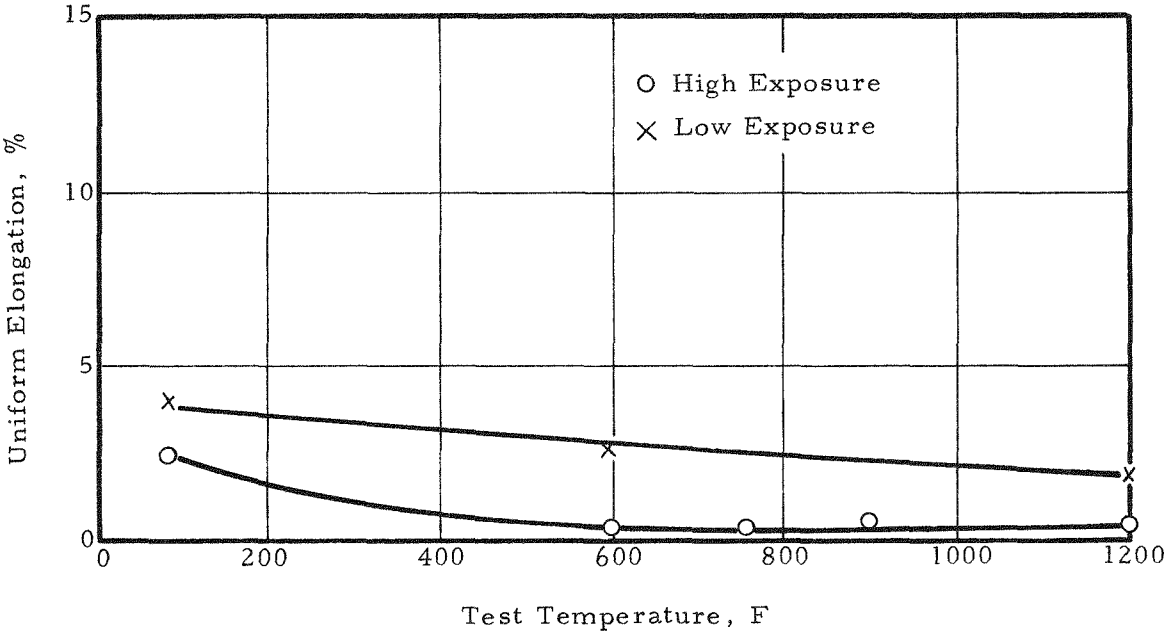

Figure 6-30. Total Elongation of Irradiated Stainless Steel Cladding Before Annealing

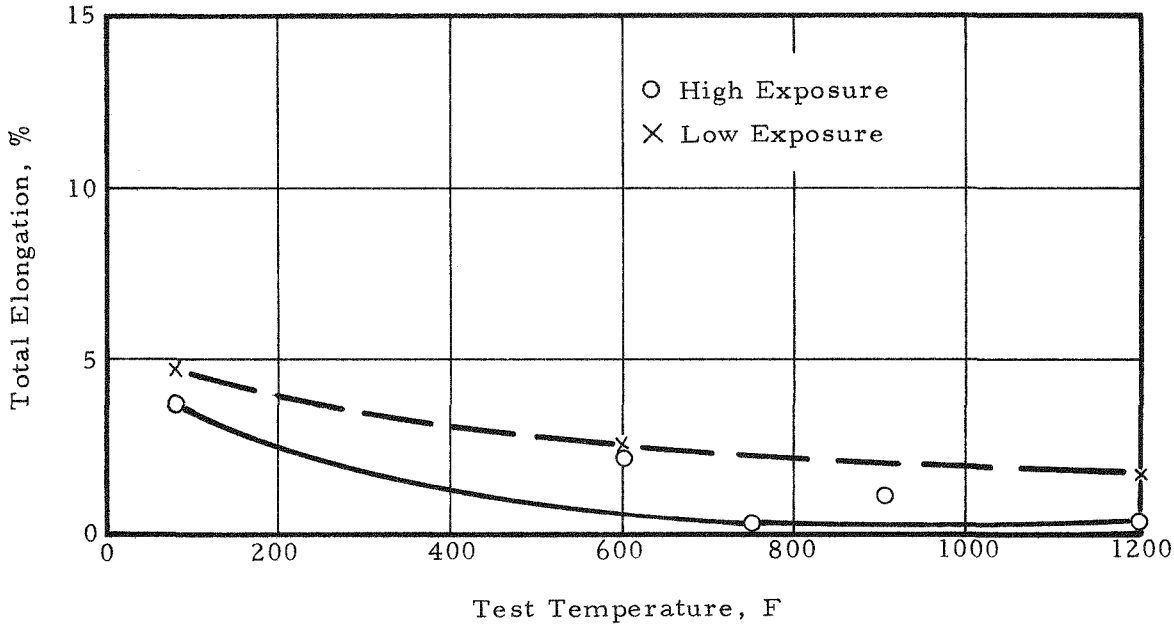

Figure 6-31. Yield Strength of Irradiated Stainless Steel Cladding After Annealing

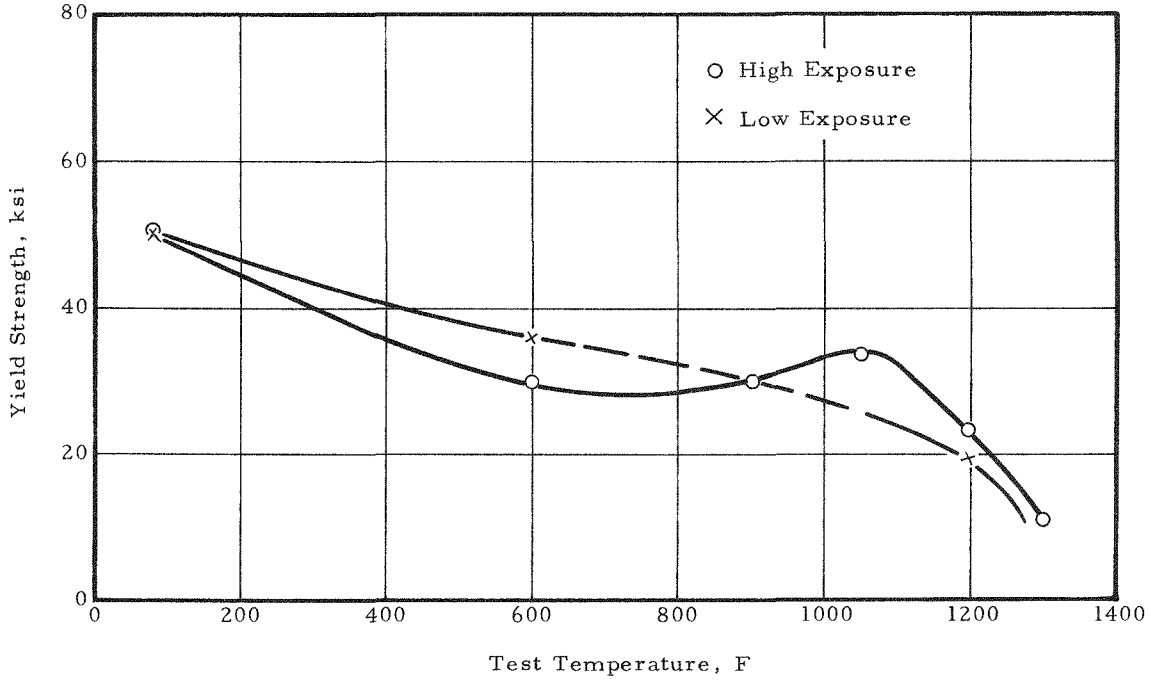

Figure 6-32. Ultimate Strength of Irradiated Stainless Steel Cladding After Annealing

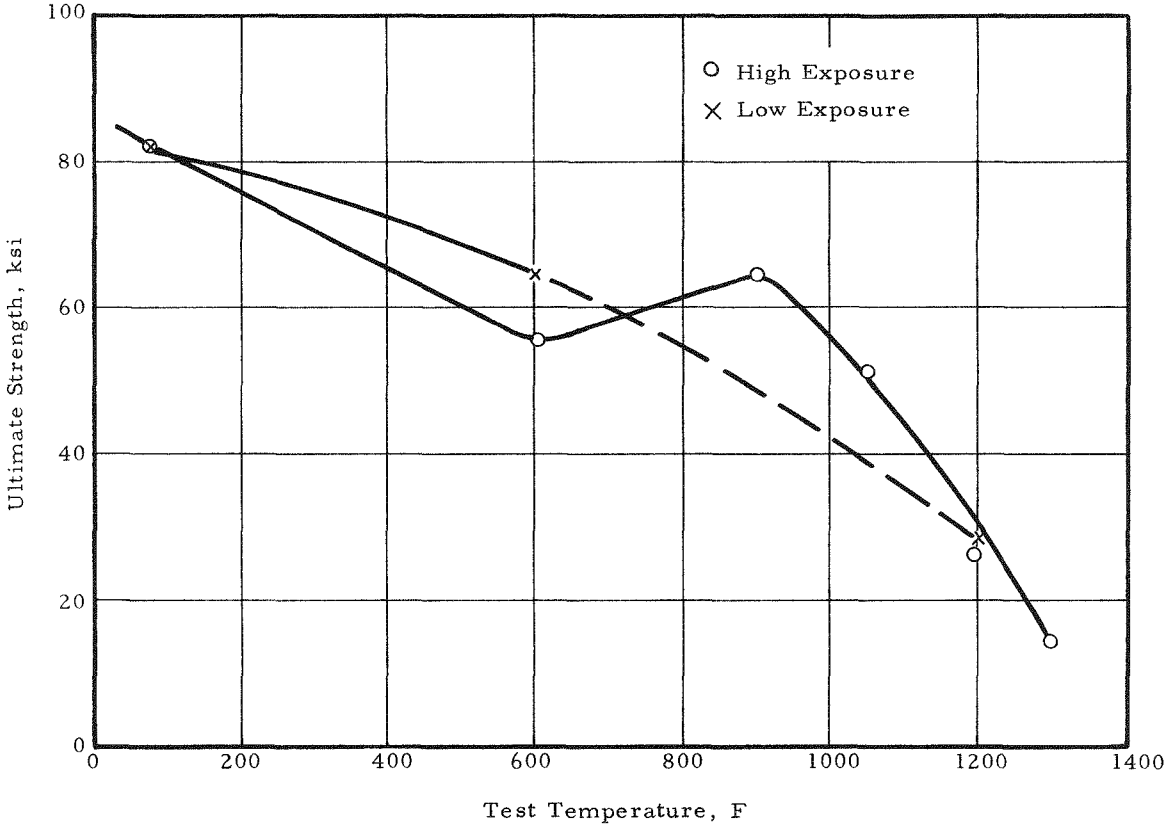

Figure 6-33. Uniform Elongation of Irradiated Stainless Steel Cladding After Annealing

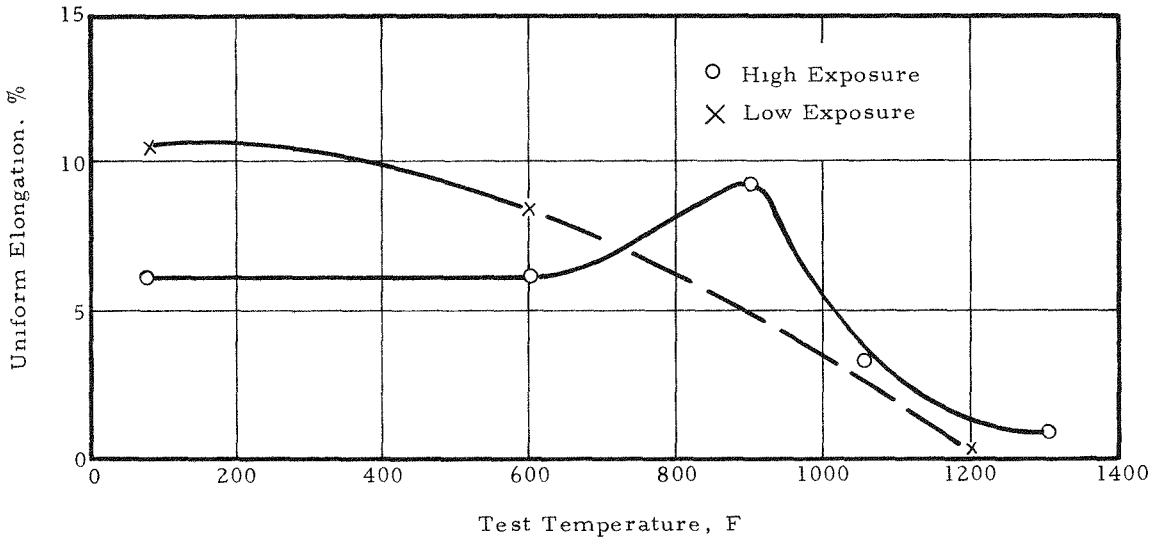

Figure 6-34. Total Elongation of Irradiated Stainless Steel Cladding After Annealing

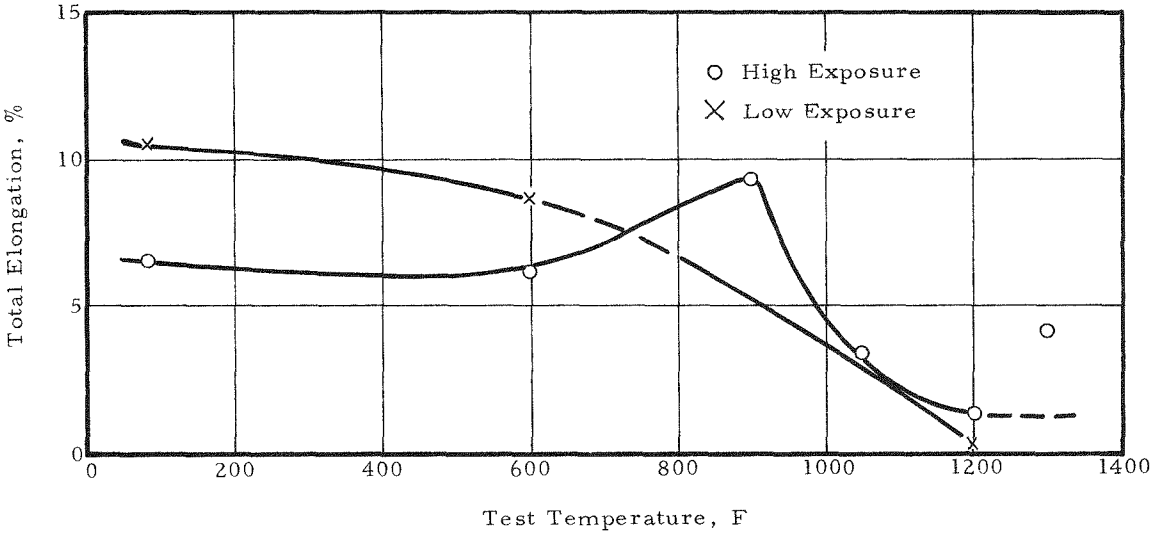

Figure 6-35. Yield Strength of Irradiated Stainless Steel Cladding Before and After Annealing

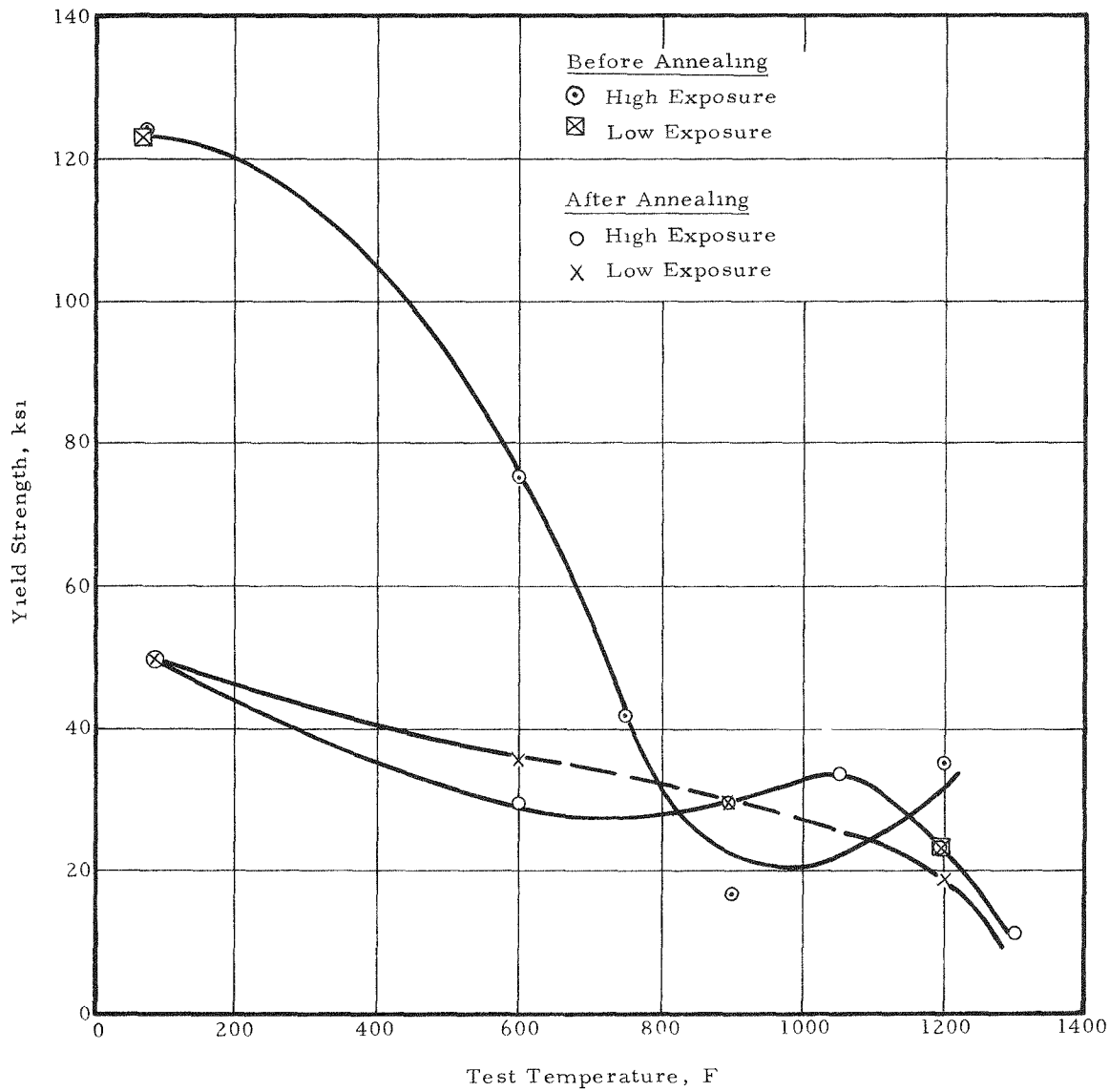

Figure 6-36. Ultimate Strength of Irradiated Stainless Steel Cladding Before and After Annealing

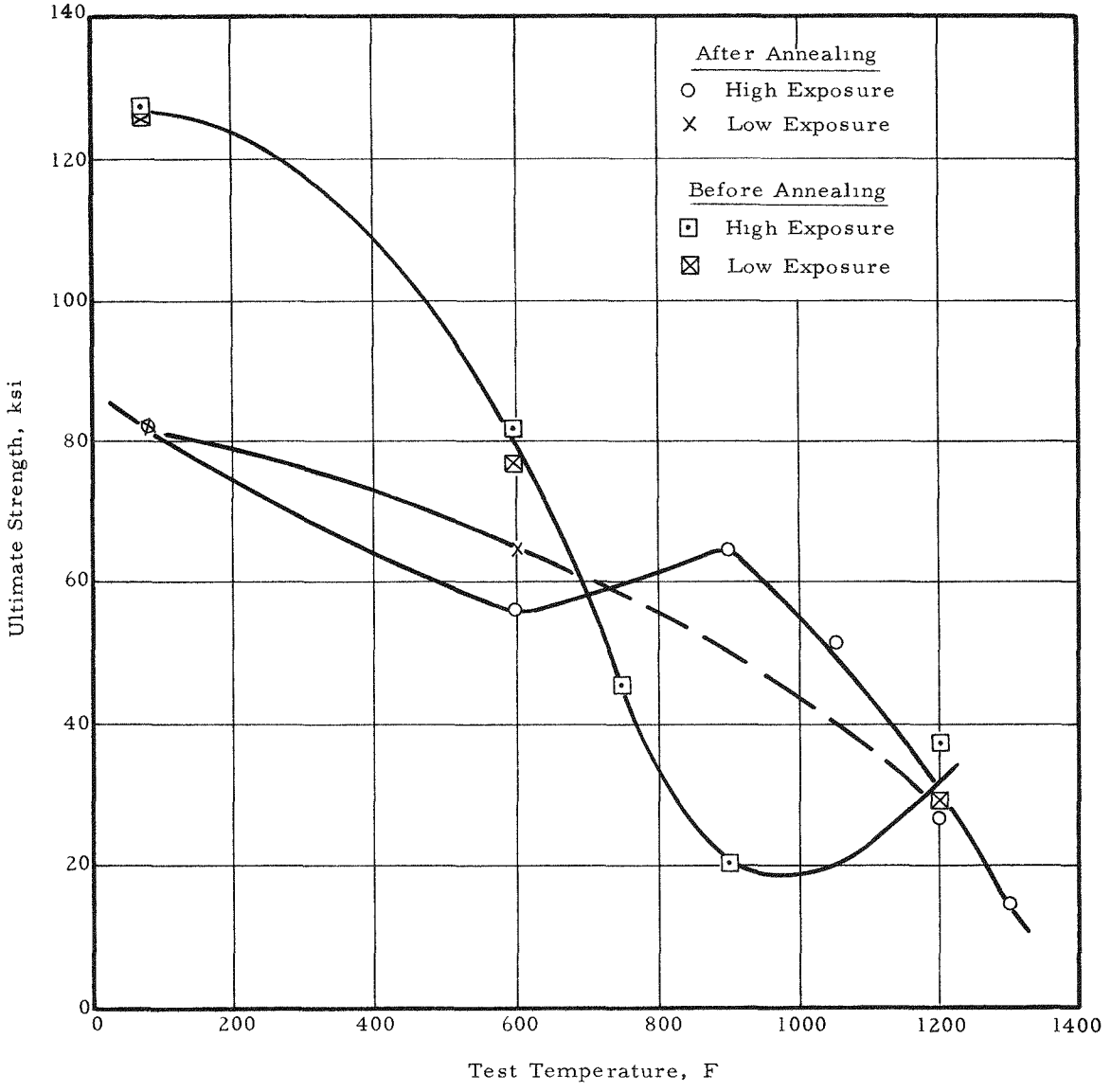

Figure 6-37. Uniform Elongation of Irradiated Stainless Steel Cladding Before and After Annealing

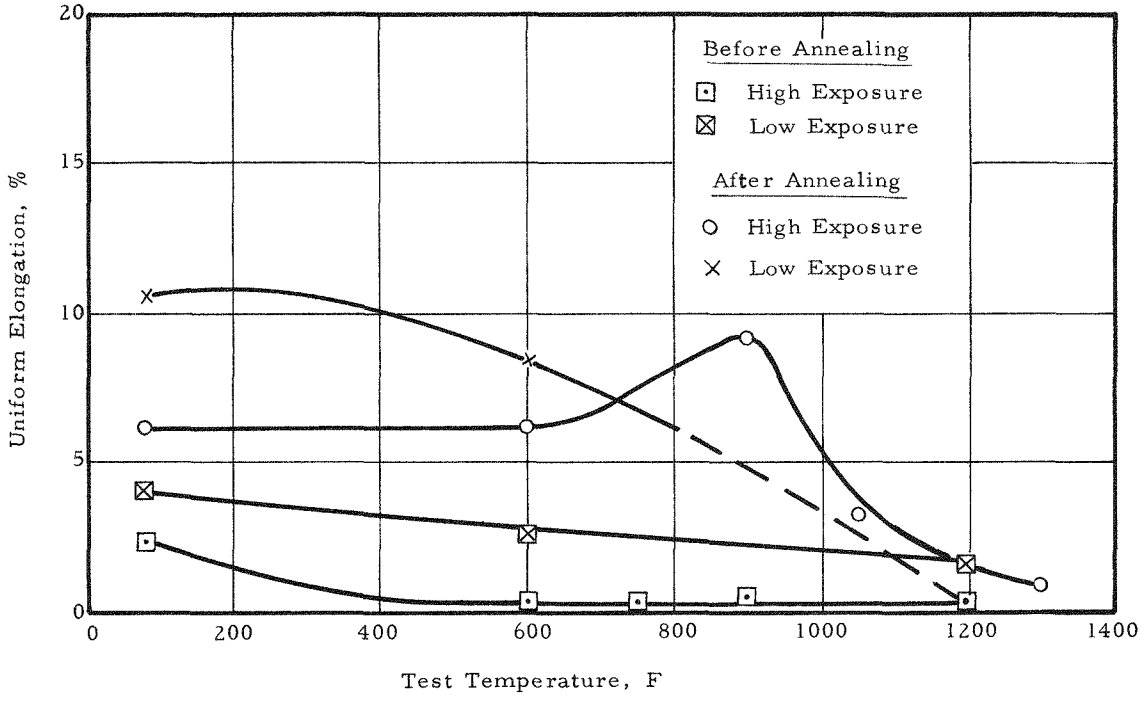

Figure 6-38. Total Elongation of Irradiated Stainless Steel Cladding Before and After Annealing

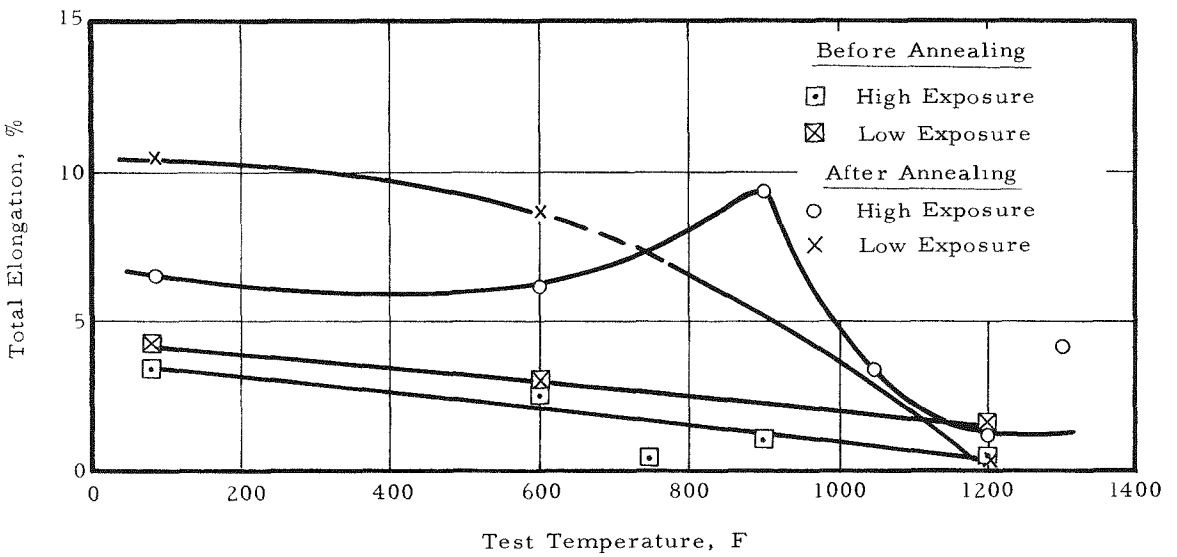

Figure 6-39. Yield Strength of Irradiated and Unirradiated Stainless Steel Cladding After Annealing

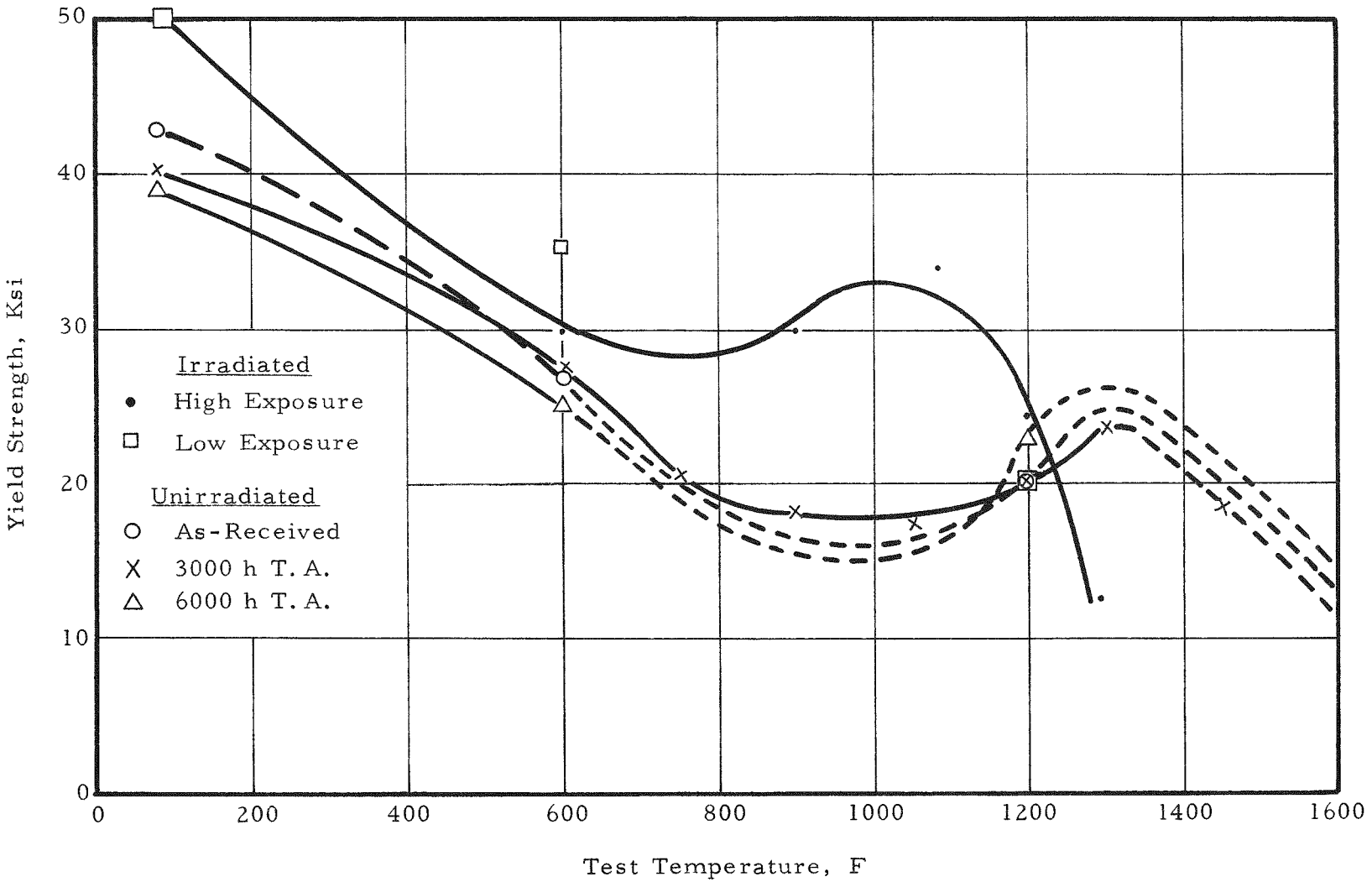

Figure 6-40. Ultimate Tensile Strength of Irradiated and Unirradiated Stainless Steel Cladding After Annealing

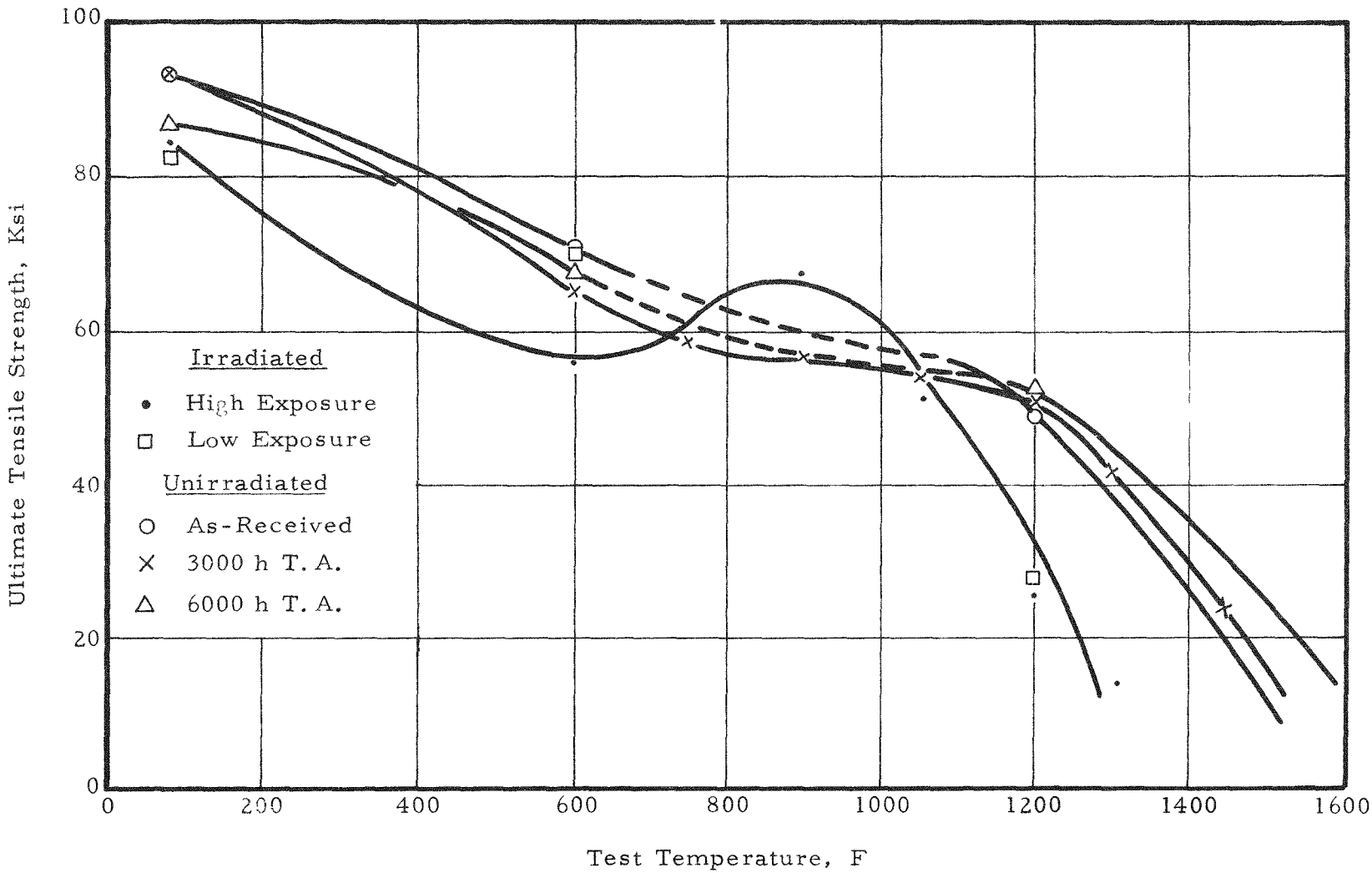

Figure 6-41. Uniform Elongation of Irradiated and Unirradiated Stainless Steel Cladding After Annealing

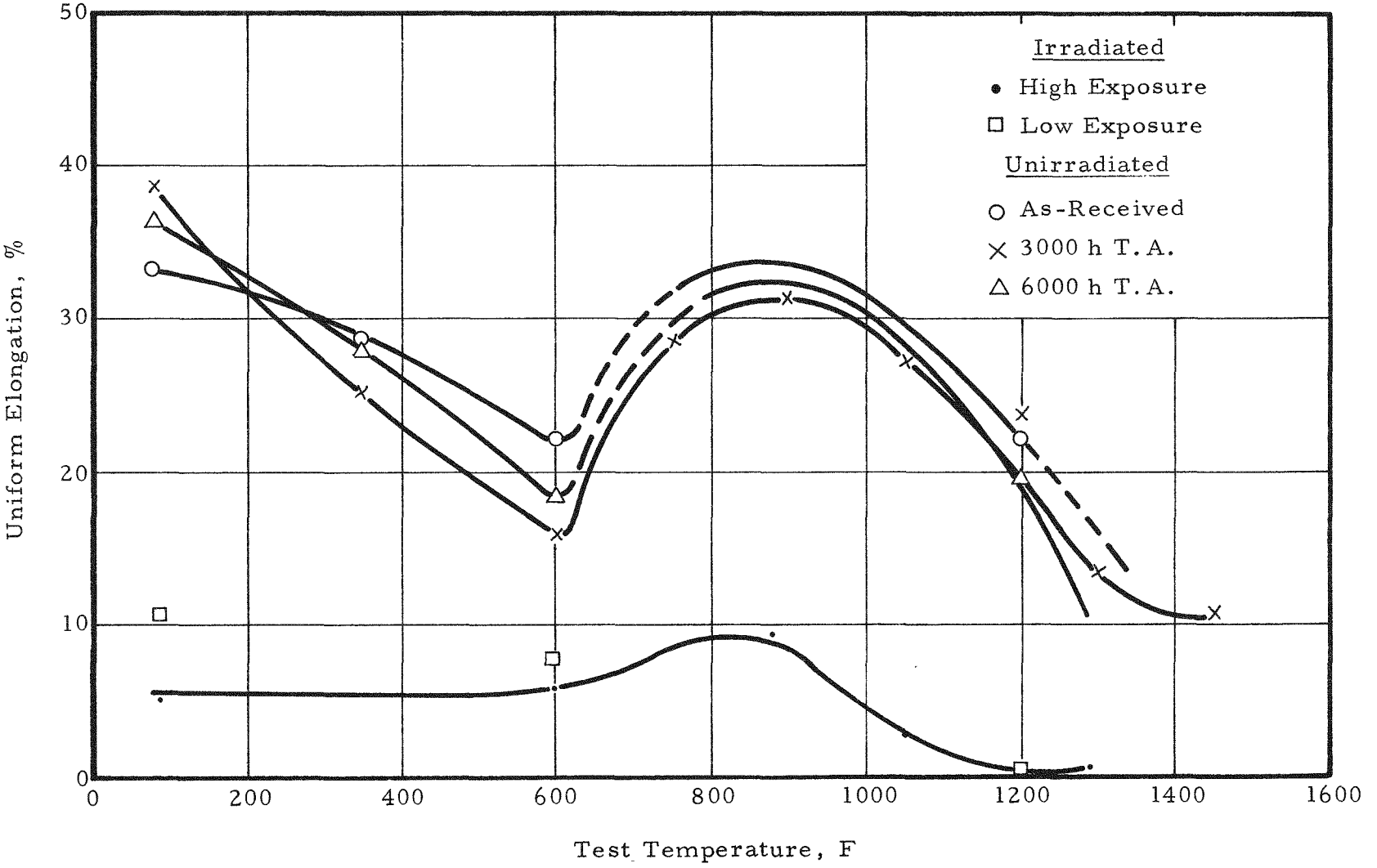

Figure 6-42. Total Elongation of Irradiated and Unirradiated Stainless Steel Cladding After Annealing

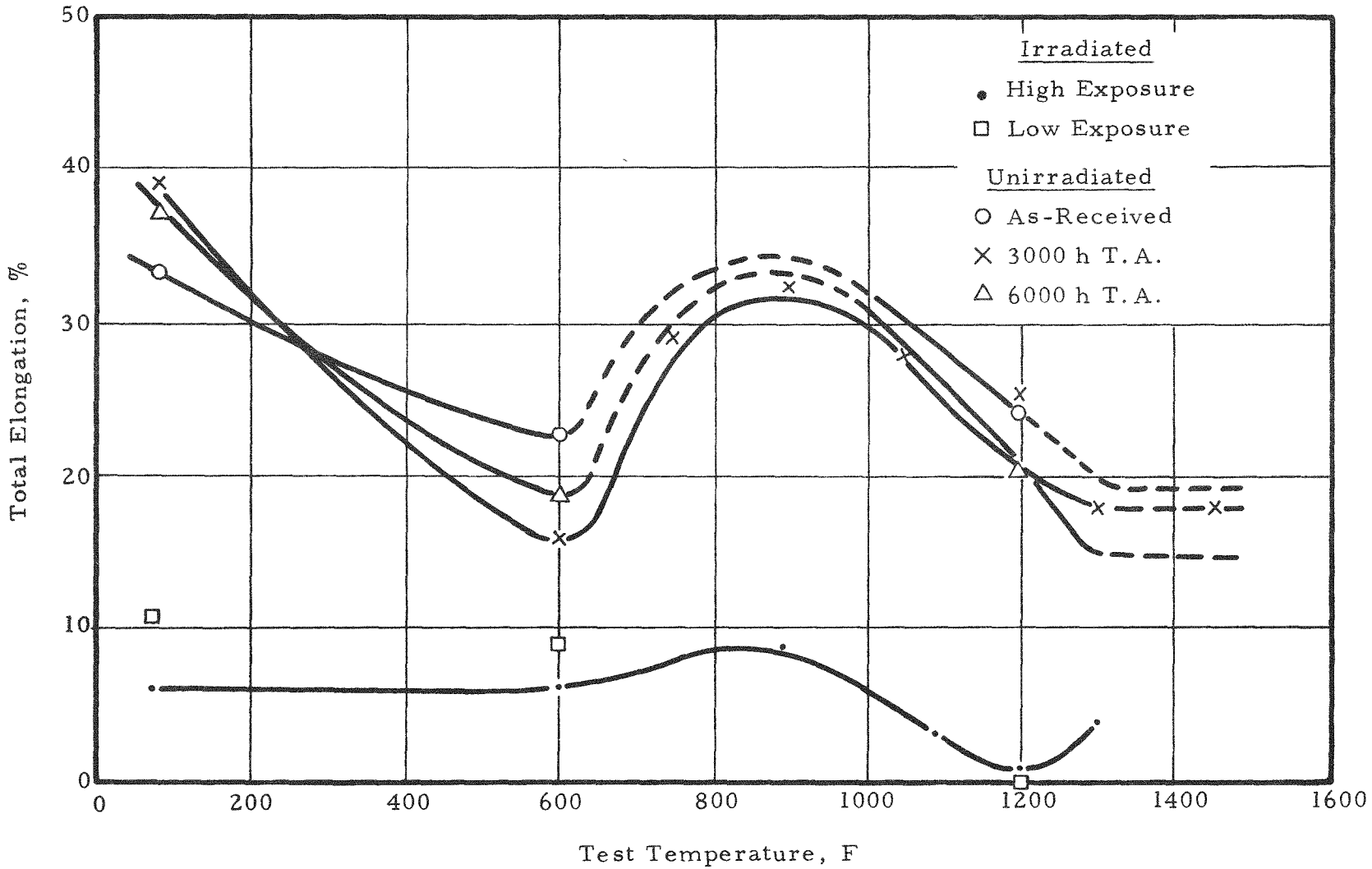

Figure 6-43. The Effect of Test Temperature and Fluence Level on the 0.2% Yield Strength of Annealed AISI Type 304 Stainless Steel (Irradiated at 290 C)

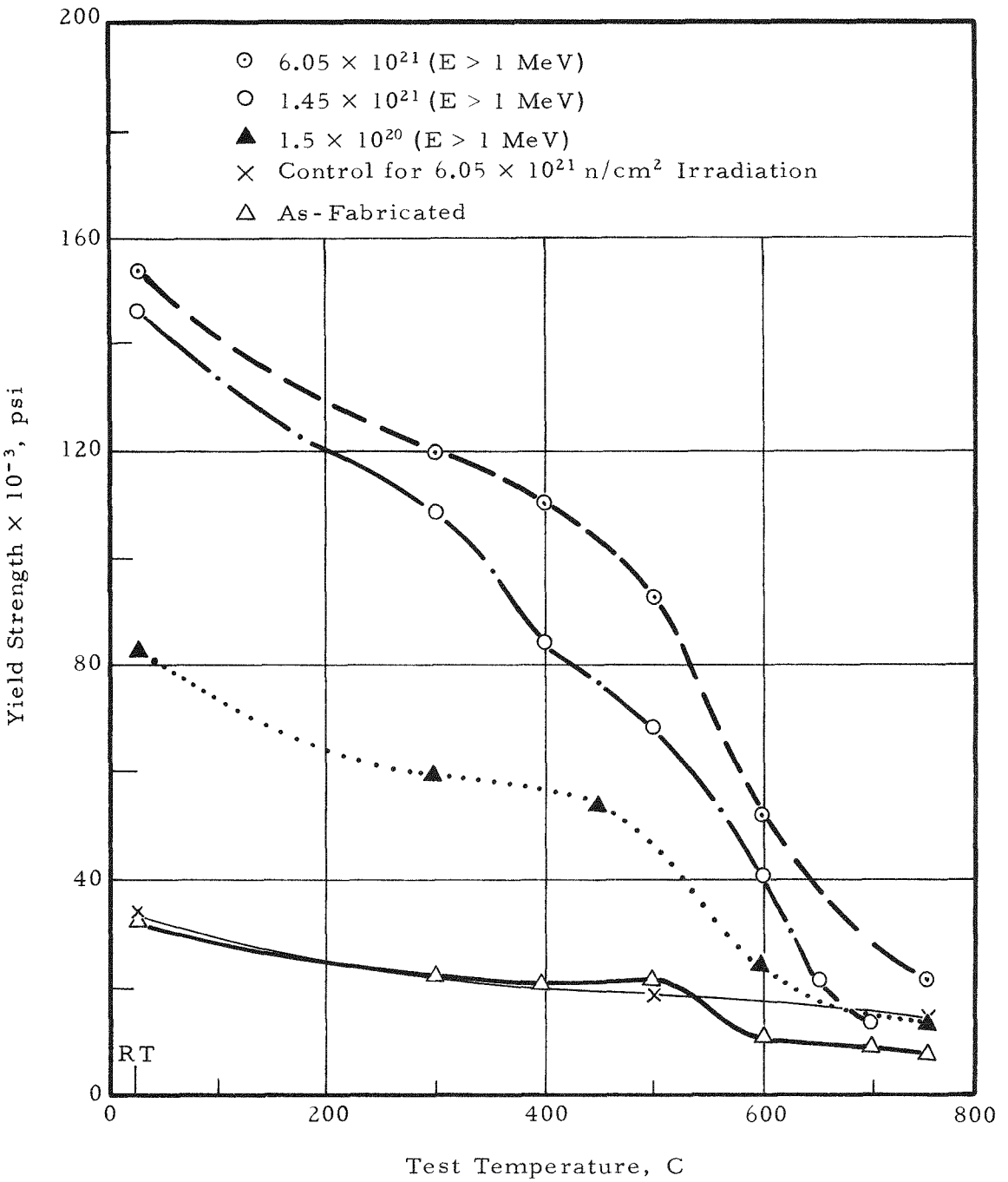

Figure 6-44. The Effect of Test Temperature on the Uniform Elongation of Annealed A1S1 Type 304 Stainless Steel (Irradiated at 290 C)

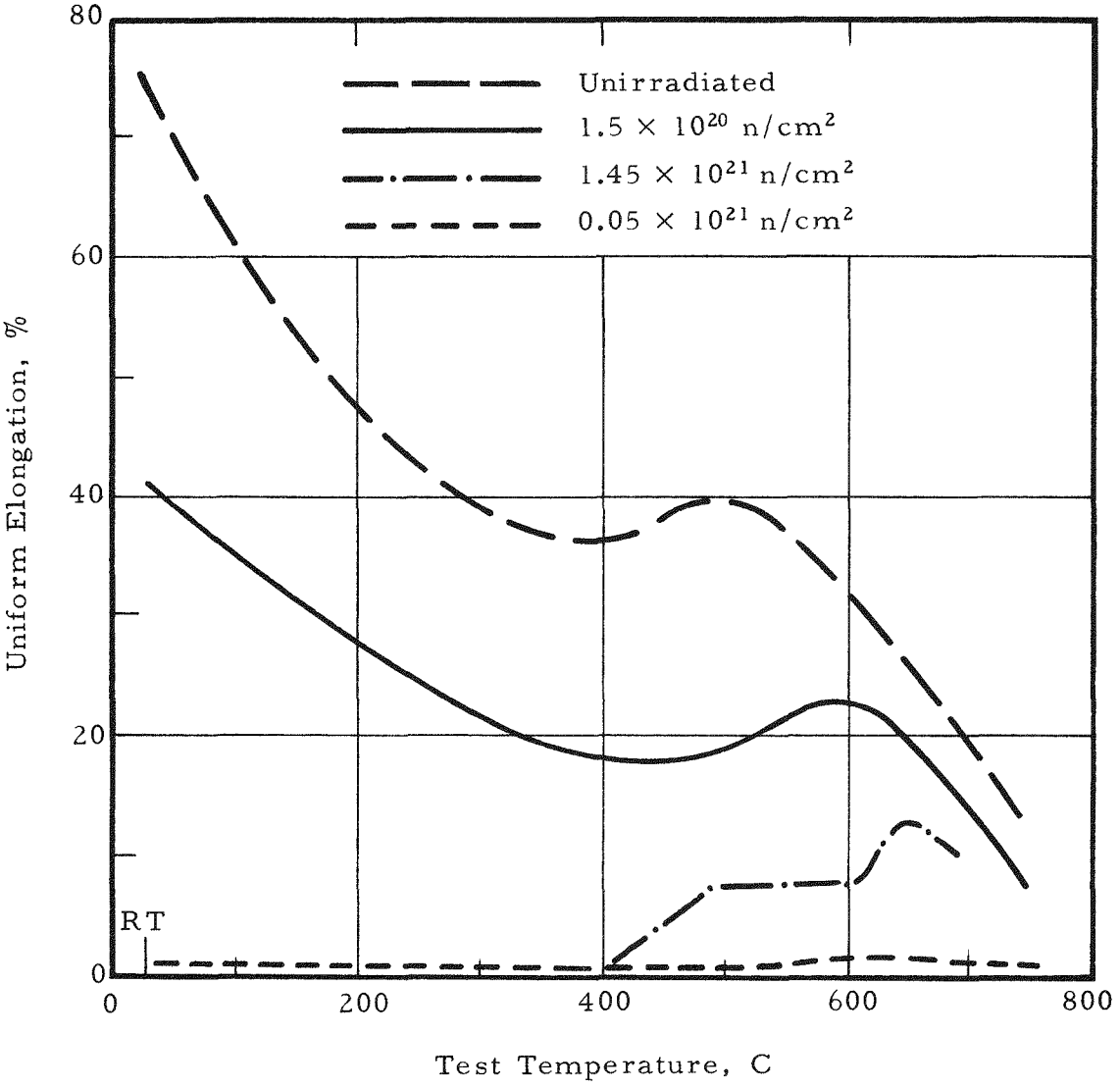

7. ZIRCALOY-2 FUEL CAN EXAMINATION

7.1. Tensile Testing

7.1.1. Purpose

This subtask was carried out to determine the post-irradiation tensile properties of the Zircaloy-2 can after operation for 442 effective full power days in the Indian Point Reactor.

7.1.2. Scope

The scope of this testing program is shown in Table 7-1. Specimens from both the longitudinal and transverse directions were tested at 70, 525, and 750 F. The 525 F test was at the approximate irradiation temperature.

7.1.3. Procedure

The Zircaloy can selected for examination was obtained from element 61. This element was predicted to have the highest fluence—about 3×10^{21} nvt (E > 1 MeV)—of the six elements selected for the program. The tensile blanks were obtained by sectioning the can with an abrasive cutoff wheel and a motorized band saw. The gage lengths were machined using a Tensil Kut machine with a special jig adapted for this type of specimen. Figure 7-1 is a sectioning diagram for the Zircaloy-2 can showing the locations from which the longitudinal and transverse specimens were taken. Dimensions of the tensile specimens used in this program are shown in Figure 7-2. The total fast fluence of the tensile specimens taken from the various positions along the can length was determined from a gamma scan of a fuel pin removed from element 61, and a ratio of the relative activity to the peak activity for each specimen location was obtained.

The tensile properties were determined with an Instron tension test machine. In all instances, a strain rate of 0.020 in./in.-min

was used. An Instron extensometer modified to fit these Zircaloy specimens was used for all three test temperatures. Representative stress-strain diagrams obtained from the room temperature and 525 and 750 F tests are shown in Figures 7-3, 7-4, and 7-5, respectively.

7.1.4. Results

The post-irradiation tensile properties for the room-temperature, 525 F, and 750 F tests are presented in Tables 7-2 through 7-4 and are shown graphically as a function of fast fluence in Figures 7-6 through 7-9. For all test temperatures, the ultimate tensile and 0.2% yield strengths continue to increase with total fluence for fast fluences up to 2.6×10^{21} (E > MeV). The fluence values given in this report were calculated and not determined by dosimetry. The strength values in the longitudinal direction were greater than in the transverse direction; however, the rate of change as a function of fast fluence appears to be the same in both directions. This was true for all three of the post-test temperatures. Preirradiation tensile data are not available for this material; therefore, the change in tensile and yield strengths as a function of fast fluence and specimen orientation could not be evaluated. However, the absolute values have been reported by Irvin for Zircaloy-2 pressure tubing irradiated at 540 F.[8] After an exposure of 2.2×10^{21}, Irvin reported tensile and yield strength values of 107,000 psi. This compares well with the 100,000 to 110,000 psi range obtained from the material in this investigation.

The increases in tensile and yield strengths are accompanied by a decrease in ductility, as shown in Figure 7-9. For all three post-test temperatures, the total elongation is greater in the transverse direction than in the longitudinal direction. However, for both directions, the absolute values of ductility were lower for the 525 F test than for the room temperature and 750 F tests. This result coincides with the apparent greater rate of increase in strength as a function of fast fluence for the 525 F test, compared with the room temperature and 750 F tests. There is no difference in the uniform elongation values, regardless of the fast fluence or specimen orientation. All of the uniform elongation values were 1% or less. For these reasons the uniform elongation values are not presented graphically. The lower ductility at 525 F is not

inconsistent with results reported in WCAP-3269-14 where a minimum in ductility occurs at 500 to 800 F.[9]

Table 7-1. Tensile Testing of Zircaloy-2 Can

	Test temperature, F					
	70		525		750	
Fluence	L	T	L	T	L	T
Minimum	2	3	3	3	2	2
1/2 peak	3	5	3	3	2	2
3/4 peak	3	3	3	2	2	3
Peak	3	3	3	2	2	2

L = longitudinal
T = transverse

Table 7-2. Effect of Irradiation at 525 F on the 70 F Tensile Properties of Zircaloy-2

Fluence $\times 10^{-21}$(a)	Type of specimen(b)	Strength, ksi		Elongation, %	
		Yield	Ultimate	Uniform	Total
0.14	L	101.2	105.8	1.3	6.4
0.14	L	101.2	105.8	1.3	5.7
0.14	T	98.1	100.9	0.1	5.8
0.14	T	95.4	97.8	0.5	10.6
0.14	T	99.0	102.8	0.4	10.4
1.5	L	97.4	104.0	1.1	1.9
1.5	L	101.5	105.7	0.6	0.8
1.5	L	101.2	108.6	1.0	5.4
1.5	T	100.1	105.9	1.3	2.6
1.5	T	95.3	109.5	1.2	3.6
1.5	T	95.6	102.8	0.9	5.6
1.5	T	102.2	109.3	0.7	7.7
1.5	T	91.3	96.6	0.8	7.7
2.2	L	101.8	109.0	0.7	4.2
2.2	L	102.5	114.8	0.6	4.4
2.2	L	109.4	113.8	0.9	5.4
2.2	T	99.0	104.8	0.8	6.5
2.2	T	94.9	104.4	0.6	7.3
2.2	T	99.8	101.5	0.4	4.3
2.6	L	103.0	113.2	0.7	4.8
2.6	L	109.2	113.1	0.7	5.9
2.6	L	109.0	111.2	0.5	4.1
2.6	T	105.8	108.2	0.5	9.0
2.6	T	105.8	108.9	0.4	9.5
2.6	T	97.8	104.1	0.5	8.8

(a) $E > 1$ MeV

(b) L = longitudinal
T = transverse

Table 7-3. Effect of Irradiation at 525 F on the 525 F Tensile Properties of Zircaloy-2

Fluence $\times 10^{-21}$(a)	Type of specimen(b)	Strength, ksi		Elongation, %	
		Yield	Ultimate	Uniform	Total
0.14	L	54.9	59.8	0.3	3.5
0.14	L	52.4	54.6	0.6	1.3
0.14	L	57.6	58.0	0.2	4.8
0.14	T	48.4	48.8	0.1	3.1
0.14	T	37.9	46.7	1.2	4.9
0.14	T	--	56.1	--	7.4
1.5	L	64.2	64.7	0.0	2.8
1.5	L	66.4	67.5	0.0	3.3
1.5	L	64.0	64.3	0.1	1.3
1.5	T	57.3	57.6	0.1	2.1
1.5	T	56.5	56.5	0.0	9.2
1.5	T	53.8	54.4	0.3	10.2
2.2	L	68.3	69.0	0.1	1.9
2.2	L	53.3	53.5	0.1	4.3
2.2	L	63.4	63.8	0.0	1.2
2.2	T	51.5	52.6	0.2	6.3
2.2	T	49.0	53.0	0.8	7.3
2.6	L	66.1	67.8	0.4	1.8
2.6	L	58.3	62.9	0.5	0.9
2.6	L	60.9	63.8	0.4	0.7
2.6	T	55.6	56.3	0.2	8.4
2.6	T	54.3	56.3	0.3	7.9

(a) F > 1 MeV

(b) L = longitudinal
T = transverse

Table 7-4. Effect of Irradiation at 525 F on the 750 F Tensile Properties of Zircaloy-2

Fluence $\times 10^{-21}$(a)	Type of specimen(b)	Strength, ksi		Elongation, %	
		Yield	Ultimate	Uniform	Total
0.14	L	50.3	50.8	0.1	8.0
0.14	L	48.8	48.8	--	7.5
0.14	T	46.6	46.8	0.0	11.6
0.14	T	46.4	46.4	---	10.9
1.5	L	49.2	49.2	--	5.1
1.5	L	51.6	51.6	--	7.0
1.5	T	38.8	42.5	0.2	8.3
1.5	T	42.6	42.7	0.1	9.1
2.2	L	52.0	54.5	0.1	6.0
2.2	L	51.6	54.5	0.6	6.6
2.2	T	46.6	46.6	--	10.7
2.2	T	54.4	54.7	0.0	3.7
2.2	T	45.5	45.5	--	9.3
2.6	L	57.0	57.3	0.0	5.8
2.6	L	58.9	58.9	--	5.2
2.6	T	48.4	48.6	0.1	10.3
2.6	T	48.1	48.7	0.2	9.9

(a) $E > 1$ MeV

(b) L = longitudinal
T = transverse

7.2. Metallography

7.2.1. Purpose

Sections of the Zircaloy-2 can were examined metallographically to determine the thickness of the oxide film and the increase in hydrogen produced by the corrosion reaction between the Zircaloy and water.

7.2.2. Scope

Specimens from four different locations along the axial length of the can were examined. Specimens were obtained from sections 1, 2, 3, and 7, as described in Figure 7-1.

7.2.3. Procedure

The metallographic specimens were vacuum-impregnated with epoxy and mounted in a cold setting compound. Fine Al_2O_3 powder was mixed with the epoxy to preserve the thin oxide film during grinding and polishing. The surface of the channel was examined in the as-polished condition, and an attempt was made to measure the thickness of the oxide film. After the thickness of the film had been measured, the specimens were etched for 5 to 15 seconds (in a solution of 25 parts lactic, 15 parts nitric, and 1 part hydrofluoric acid) to outline the hydrogen platelets. The amount of hydrogen in the Zircaloy-2 was estimated by comparing the density of the hydrogen platelets with that of specimens of known hydrogen content.

7.2.4. Results

Figures 7-10 and 7-11 are photomicrographs of the specimens in the as-polished and etched conditions. The oxide film on all specimens was too thin to measure; thus it was impossible to determine the corrosion rate for the can. According to Lustman and Kerze, [10] the oxide film on Zircaloy-2 exposed to 550 F water for 800 days would be about 1.5 microns thick. An oxide film 1.0 microns thick would be produced by exposure to 500 F water for 800 days. [11] Thus, the available data indicate that the oxide film would be less than 1.5 microns thick unless irradiation enhanced the corrosion behavior. The inability to

measure the very thin film on the can suggest that the corrosion of the Zircaloy-2 channel was not enhanced by irradiation.

Assuming that a 1.5 micron oxide film was produced on each surface, then a total of 6.0 mg/dm^2 of hydrogen would be produced. If the Zircaloy-2 channel absorbed 100% of the hydrogen produced, then the hydrogen content of the can would be increased by about 40 ppm, and its total hydrogen content would be less than 65 ppm. The hydrogen content of the can was estimated to be less than 40 ppm.

Because the oxide film could not be measured and because the hydrogen content of the can in the unirradiated condition was not known, it was impossible to determine what percentage of the hydrogen was absorbed. Because the hydrogen content after irradiation was estimated to be less than 40 ppm, it is apparent that irradiation did not enhance the hydrogen uptake.

Figure 7-1. Sectioning Diagram for Zircaloy-2 Can

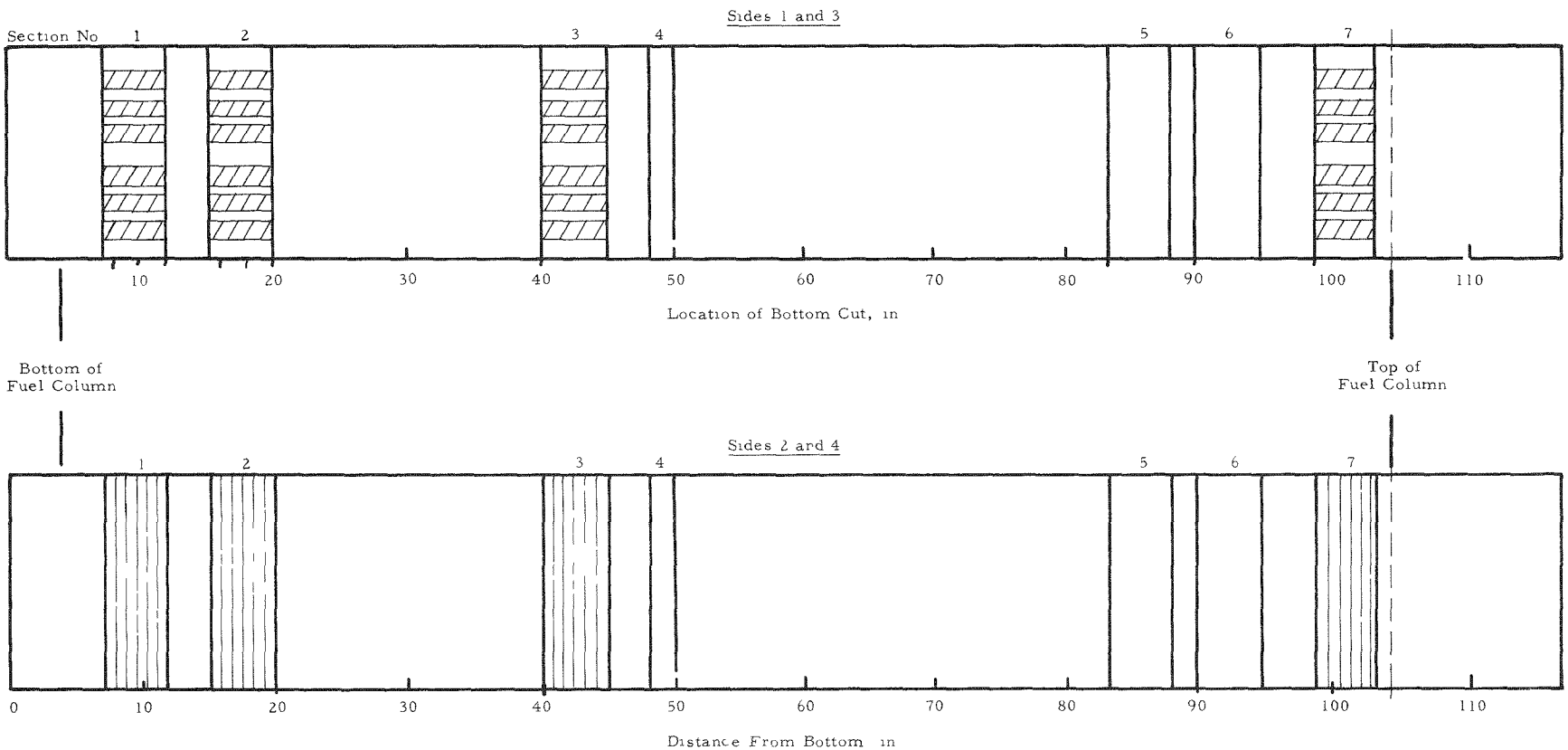

Figure 7-2. Dimensions of Tensile Specimens for Zircaloy-2 Can

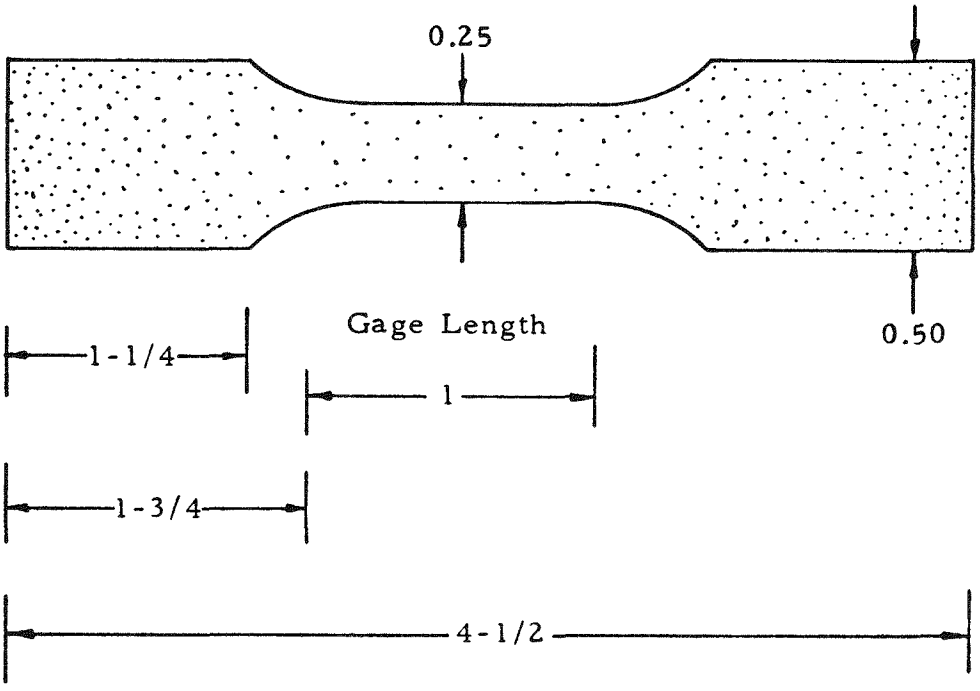

Dimensions in Inches

Figure 7-3. Load Deflection Curve for a Specimen Tested at 70 F

Figure 7-4. Load Deflection Curve for a Specimen Tested at 525 F

Figure 7-5. Load Deflection Curve for a Specimen Tested at 750 F

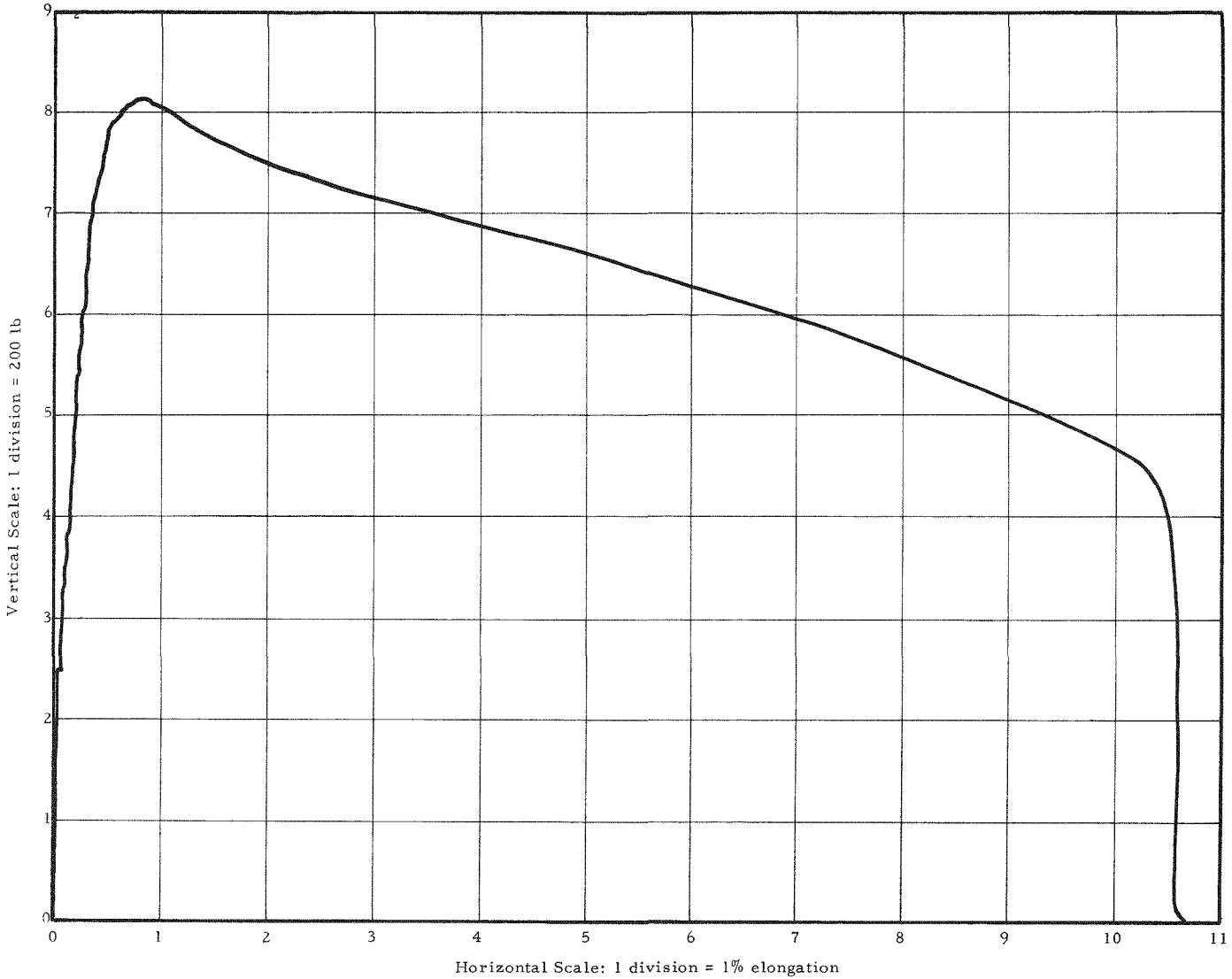

Figure 7-6. Effect of Irradiation at 525 F on the Strength of Zircaloy-2 at 70 F

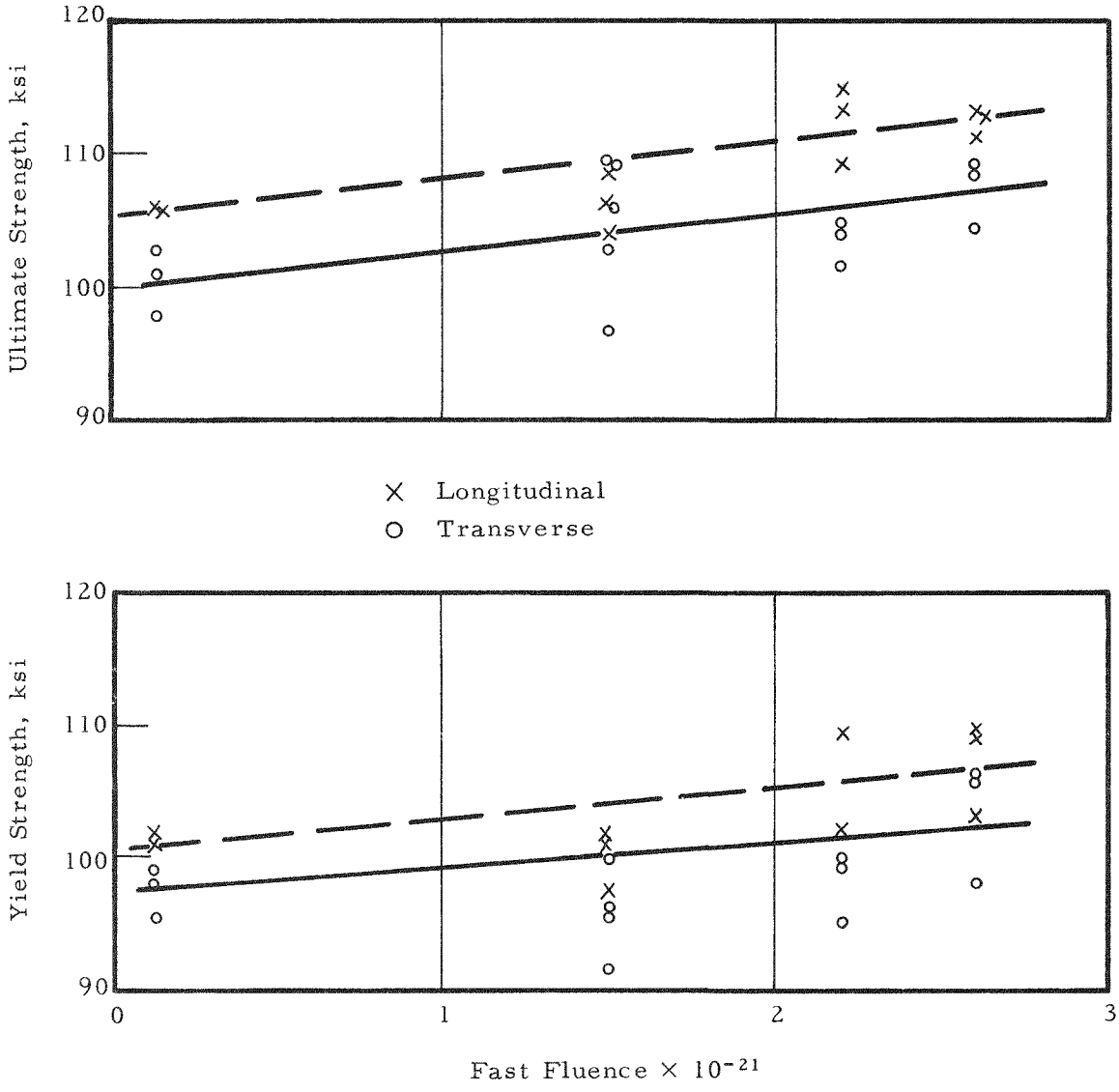

Figure 7-7. Effect of Irradiation at 525 F on the Strength of Zircaloy-2 at 525 F

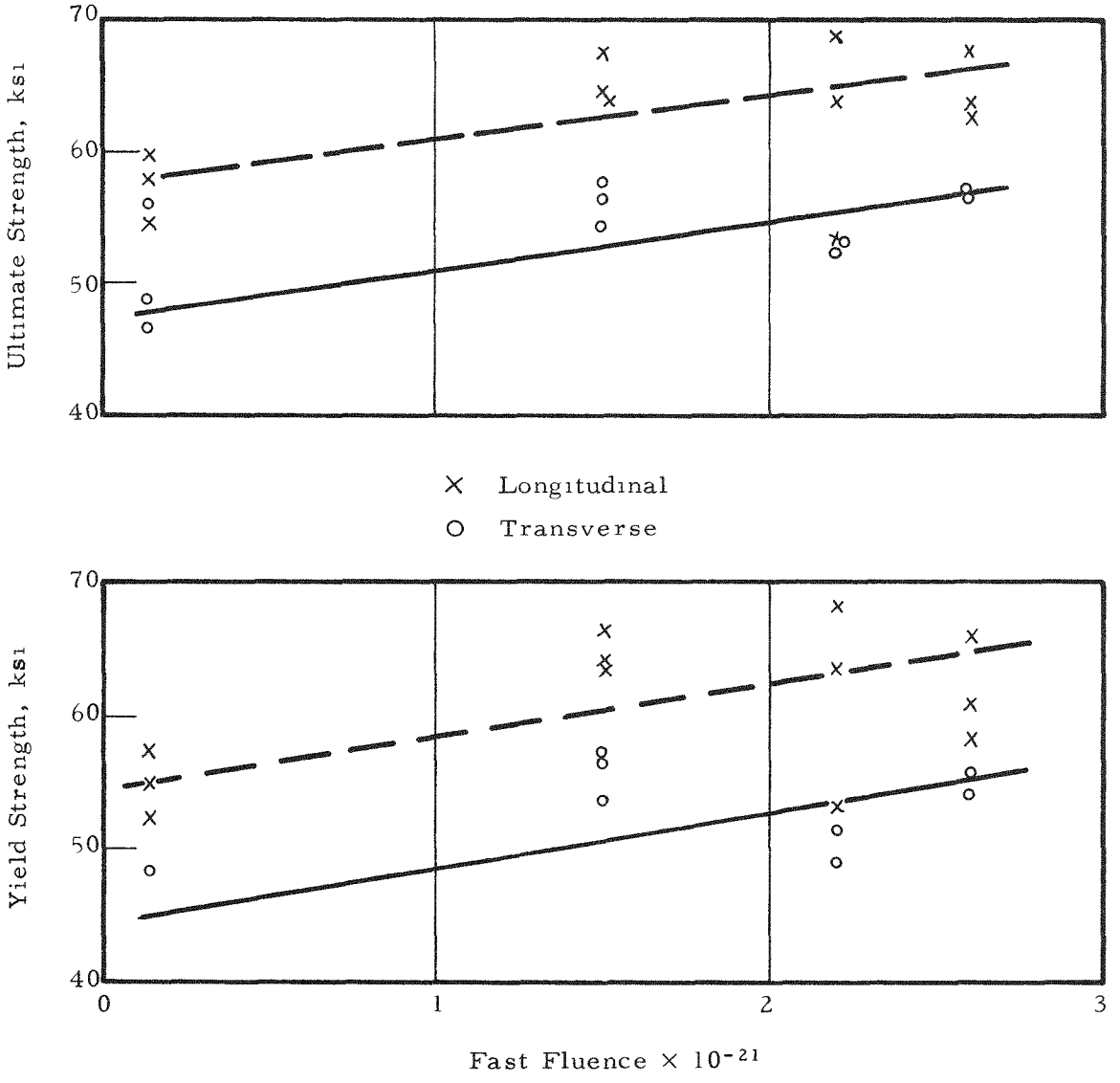

Figure 7-8. Effect of Irradiation at 525 F on the Strength of Zircaloy-2 at 750 F

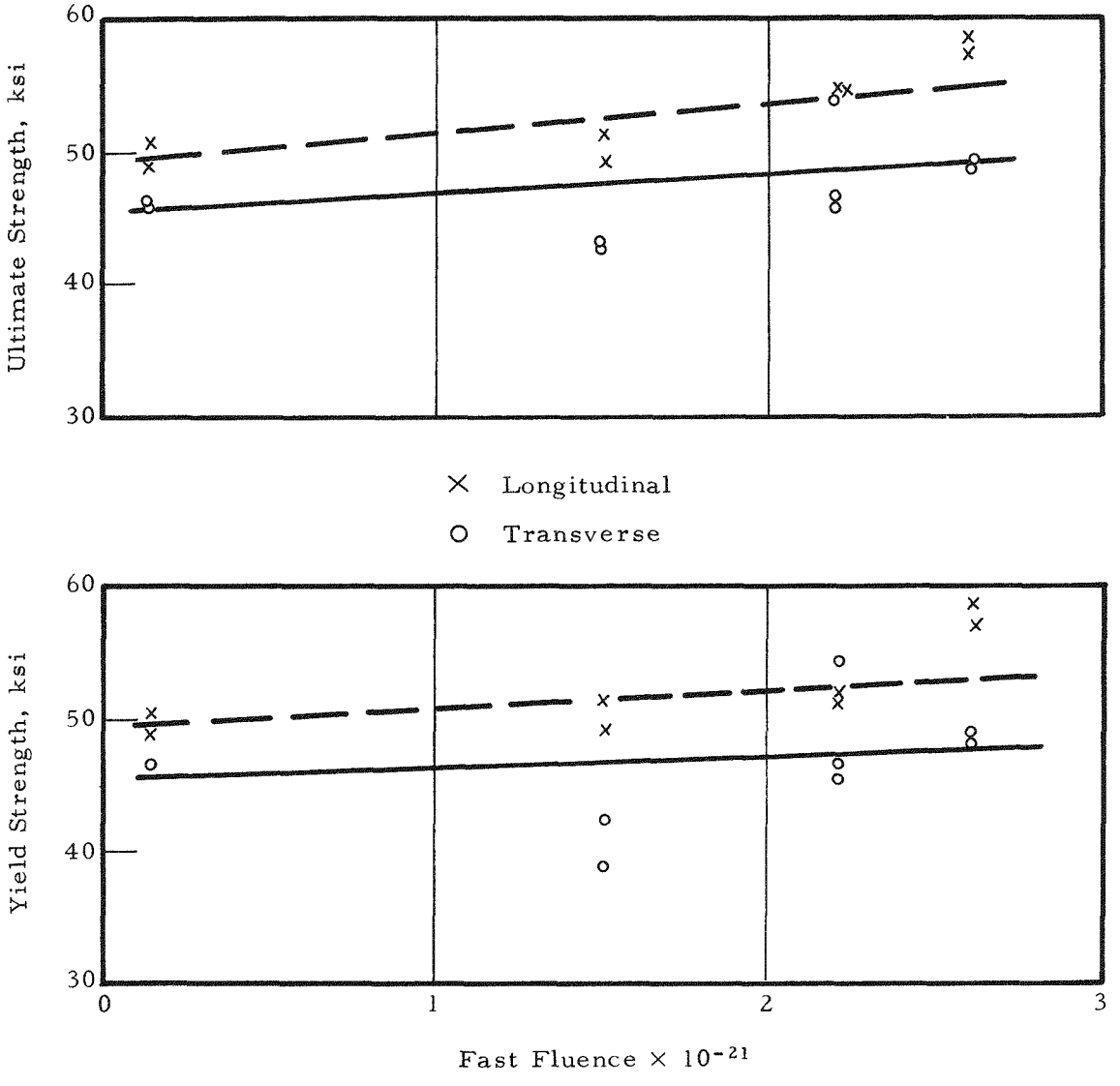

Figure 7-9. Effect of Irradiation at 525 F on the Total Elongation of Zircaloy-2

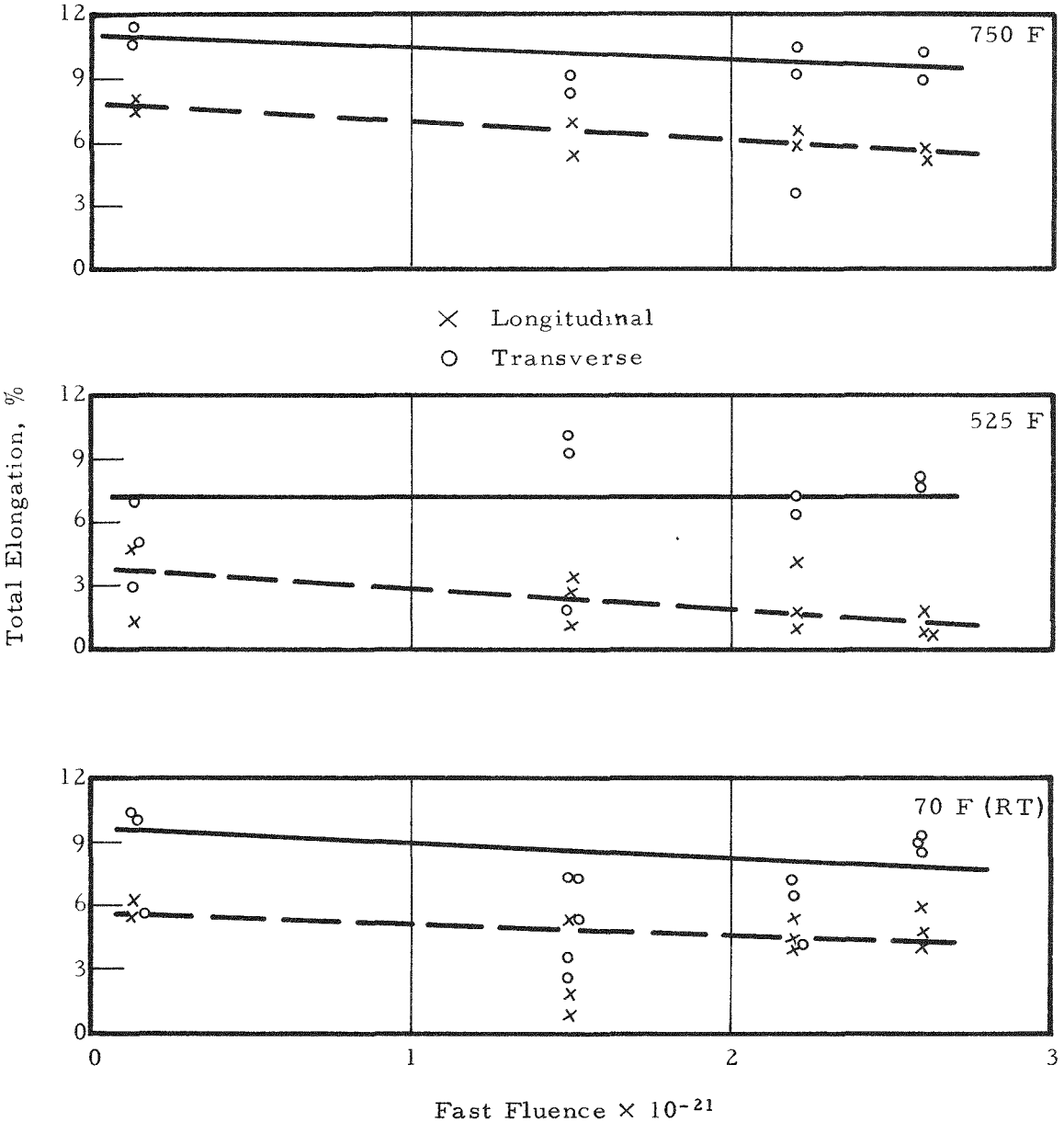

Figure 7-10. Appearance of Zircaloy-2 Channel at Section 1
(See Figure 7-1 for Location)

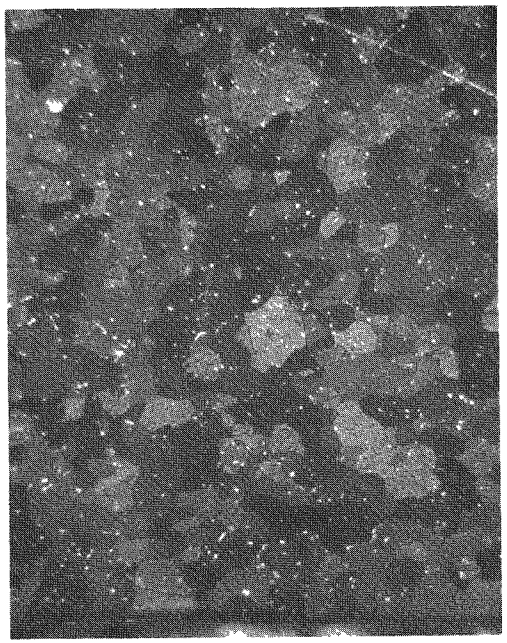

250×
Inside Surface

250×
Center of Channel

250×
Outside Surface

All Specimens Etched With Lactic Acid

Figure 7-11. Appearance of Zircaloy-2 Channel at Section 7
(See Figure 7-1 for Location)

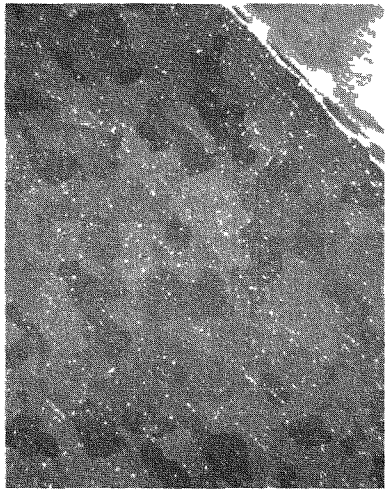

Light Etched 250×

Inside Surface — Polarized

Light As Polished 250×

Inside Surface — Bright

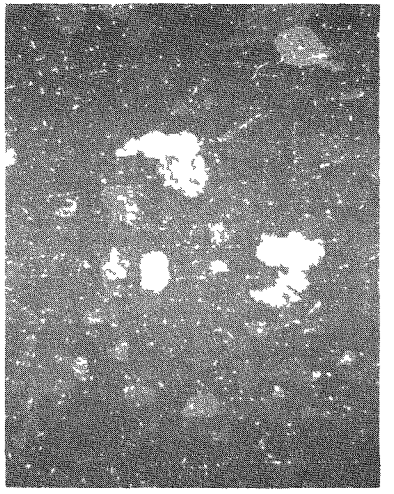

Light Etched 250×

Center of Channel — Polarized

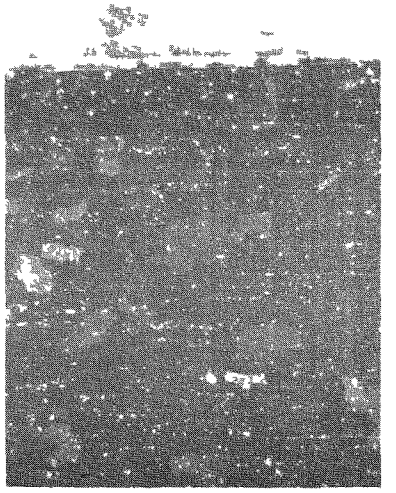

Light Etched 250×

Outside Surface — Polarized

REFERENCES

[1] Williamson, H. E., et al., AEC Fuel Cycle Program — Examination of Zircaloy-Clad UO_2 Fuel Rods Operated in the VBWR to 10,000 MWD/TU, GEAP-4597, March 1966.

[2] Bezella, W. A., Analyses of the Fission Gases Released Within Spent Yankee Fuel Rods, WCAP-6087, February 1968.

[3] Lyons, M. F., et al., "New Evidence to Delineate the UO_2 Molten Boundary," Trans. Am. Nucl. Soc., Vol 8, No. 2, November 1965.

[4] Collins, C. G., Moteff, J., and Chandler, B. A., Evaluation of the Potential of Selected Alloys for Use as a Fuel Cladding Material in an LMFBR, GEMP-573, November 1967.

[5] Bement, A. L., et al., Effects of Irradiation on the Structure and Properties of Stainless Steel, BNWL-SA-1876, August 1968.

[6] Conner, J. G. and Porembka, S. W. (editors), A Compendium of Properties and Characteristics for Selected LMFBR Cladding Materials, BMI-1900, May 1968.

[7] Weir, J. R. and Martin, W. R., Data Presented at the 7th General Meeting on the Irradiation Effects on Reactor Structural Materials, Columbus, Ohio, November 1966.

[8] Irvin, J. E., "Effects of Irradiation and Environment on the Mechanical Properties and Hydrogen Pickup of Zircaloy," Electro Chemical Technology, Vol 4, No. 5-6, May-June 1966.

[9] Scott, D. B., Physical and Mechanical Properties of Zircaloy-2 and -4, WCAP-3269-14, May 1965.

[10] Lustman, B. and Kerze, F., Jr., The Metallurgy of Zirconium, McGraw-Hill Book Co., Inc. (1955).

[11] Pressurized Water Reactor (PWR) Project Technical Progress Report, October 1963-January 1964, Westinghouse, WAPD-MRP-107.

DISTRIBUTION

1. U.S. Atomic Energy Commission
New York Operations Office
376 Hudson Street
New York, New York 10014

Attn: L. Graup

2. U.S. Atomic Energy Commission (18)
Washington, D.C. 20545

Attn: J.M. Simmons (2)
L. Rubenstein
A. Van Echo
J.A. Lieberman
S.A. Szawlewicz
M.A. Rosen
R.E. Pahler
D.E. Erb (2)
R.W. Barber
W.H. McVey
I.F. Zartman
J.W. Vaughn (NR) (2)
L.J. Colby
C.E. Weber
Document Library

3. U.S. Atomic Energy Commission (227)
Division of Technical Information Extension
P.O. Box 62
Oak Ridge, Tennessee 37830

4. Ames Laboratory (2)
U.S. Atomic Energy Commission
Iowa State University
Ames, Iowa 50010

Attn: O.N. Carlson
W.L. Larsen

5. Argonne National Laboratory (4)
9700 South Cass Avenue
Argonne, Illinois 60439

Attn: R.C. Vogel
M.V. Nevitt
J.H. Kittel
F. Foote

6. Brookhaven National Laboratory
Upton, Long Island, New York 11973

Attn: D. Gurinsky

---

7. Los Alamos Scientific Laboratory (3)
P.O. Box 1663
Los Alamos, New Mexico 87544

Attn: D.B. Hall (2)
R.D. Baker

---

8. Oak Ridge National Laboratory (5)
P.O. Box X
Oak Ridge, Tennessee 37830

Attn: J.E. Cunningham (2)
P. Patriarca
J. Weir
D.E. Ferguson

---

9. Pacific Northwest Laboratory (6)
P.O. Box 999
Richland, Washington 99352

Attn: J.J. Cadwell
F.W. Albaugh
T.T. Claudson
A.L. Bement
R. Dillion
R.G. Wheeler

---

10. Atomics International (2)
P.O. Box 309
Canoga Park, California 91304

Attn: H. Pearlman
W. Murray

---

11. Battelle Memorial Institute (3)
505 King Avenue
Columbus, Ohio 43201

Attn: DMIC
S. Paprocki
W. Berry

---

12. Combustion Engineering, Inc. (2)
Windsor, Connecticut 06095

Attn: W.P. Chernock
S.S. Christopher

13. Gulf General Atomic, Inc. (2)
P.O. Box 1111
San Diego, California 92112

Attn: S. Jaye
G. Buzzelli

14. General Electric Company (4)
Atomic Power Equipment Department
P.O. Box 1131
San Jose, California 95108

Attn: K. Cohen (2)
T. Pashos
H. Klepfer

15. Knolls Atomic Power Laboratory (3)
P.O. Box 1072
Schenectady, New York 12301

Attn: Library (2)
A.E. Bibb

16. General Electric Company (3)
Nuclear Materials & Propulsion Operation
P.O. Box 132
Cincinnati, Ohio 45215

Attn: V.P. Calkins
C. Brassfield
J. McGurty

17. E.I. du Pont de Nemours and Company (2)
Savannah River Laboratory
Aiken, South Carolina 29801

Attn: S. Rideout (2)

18. Westinghouse Electric Corporation (3)
Atomic Power Division
P.O. Box 355
Pittsburgh, Pennsylvania 15230

Attn: T. Stern (2)
R. Allio

19. Westinghouse Electric Corporation (5)
Bettis Atomic Power Laboratory
P.O. Box 79
West Mifflin, Pennsylvania 15122

Attn: E.J. Kreigh
R.H. Fillnow
B. Lustman
W.J. Babyak
J.J. Taylor

20. Idaho Nuclear Corporation (2)
P.O. Box 1845
Idaho Falls, Idaho 83401

Attn: J.M. Beeston
W.C. Francis

21. Babcock & Wilcox (93)

Arthur, VD
Ball, RM
Baroch, CJ (2)
Barringer, HS
Bishop, WN (45)
Breazeale, WM
Central Files (6)
Clark, RH
Collings, DM
Deuster, RW
Dewell, EH
Engelder, TC
Ewing, JW
Gibson, WR
Grant, SP
Harbinson, EN
Holt, CD
Hostetler, DR
Johnson, CR
Kosiancic, EJ/Carlson, RV
Lewis, RH
Library (2)
Littrell, LW (2)
Lynch, ED
Marsh, SF (2)
McDaniel, GT
Moncrief, EC
Moore, WT
Munim, AV
North, DC
Poor, HH/Alliance
Prince, LK
Probert, PB/Barberton
Rosenberger, GG
Schmitt, DH
Travis, CC/TRG
Vorres, KS/Rubright, MM/Alliance
Weissert, LR
Wolfe, GE
Womack, RE